Università di Pisa

Scuola di Dottorato "Leonardo da Vinci"

PhD Programme in
Mechanical Engineering

PhD Dissertation

Smart materials and vehicle efficiency. Design and experimentation of new devices.

Francesco Bucchi

2014

Università di Pisa

Scuola di Dottorato "Leonardo da Vinci"

PhD Programme in
Mechanical Engineering

PhD Dissertation

Smart materials and vehicle efficiency. Design and experimentation of new devices.

Author:

Francesco Bucchi .....

Tutors:

Prof. Ing. Francesco Frendo .....

Prof. Ing. Paola Forte .....

SSD ING–IND/14

2014

Abstract

In this dissertation the activities carried out during the PhD are comprehensively described. The research mainly focused on the development of novel smart devices aimed at disengaging auxiliaries in internal combustion engine vehicles. In particular, the activities dealt with modeling, design, manufacturing and testing different fail-safe magnetorheological clutch prototypes, in the framework of a project funded by Regione Toscana, which involved two departments of the University of Pisa and Pierburg Pump Technology - Stabilimento di Livorno.

After an extended literature review, several concepts of the clutch were proposed, which led to the design of the first magnetorheological prototype. An intensive experimental campaign was conducted, which involved several prototypes. A particular attention was focused on the measurement and analysis of the torque transmitted by the clutch in different operating conditions and new indices were proposed to objectively analyze the performances of magnetorheological clutches in general. On the basis of the results of the first experimental phase, the limits of the first design were analyzed and a novel prototype was developed, which succeeded in fulfilling all the design specifications.

Further analyses were carried out in order to develop a clutch model starting from the experimental results. The effect of clutch heating was considered and a complete model of the clutch based on neural networks was proposed. The model was capable of taking into account the effect of the main parameters influencing the torque characteristic and may be used in a vehicle simulator or in a hardware-in-the-loop bench.

Finally, an additional component to be connected to the clutch, which made use of shape memory alloys, was developed and tested during the visiting period at the University of Toledo (OH), USA.

Sommario

All'interno di questa tesi sono descritte le attività di ricerca condotte durante l'intero dottorato, che hanno riguardato lo sviluppo di nuovi componenti meccanici facenti uso di materiali intelligenti. In particolare sono stati progettati e realizzati vari dispositivi concepiti al fine di disconnettere gli organi ausiliari nei motori a combustione interna. L'attività di ricerca ha riguardato la modellazione, la progettazione, l'ingegnerizzazione e la sperimentazione di frizioni a fluido magnetoreologico, eccitate da magneti permanenti, all'interno di un progetto finanziato dalla Regione Toscana, che ha coinvolto l'Università di Pisa e Pierburg Pump Technology - Stabilimento di Livorno.

Inizialmente è stata condotta un'ampia analisi bibliografica e sono stati proposti vari progetti preliminari della frizione, che hanno portato verso la definizione del primo prototipo realizzato. Successivamente è stata portata avanti un'intensa campagna di prove sperimentali che ha riguardato diversi prototipi di frizione. Una particolare attenzione è stata dedicata alla misura della coppia trasmessa in differenti condizioni di utilizzo. Attraverso un'analisi critica dei risultati sperimentali sono stati evidenziati i limiti dei modelli utilizzati durante la progettazione e sono stati proposti alcuni miglioramenti, che hanno portato alla realizzazione di un nuovo prototipo in grado di soddisfare le specifiche previste all'interno del progetto finanziato.

All'analisi dei risultati sperimentali ha fatto seguito un ulteriore approfondimento riguardante l'effetto del riscaldamento sulla coppia trasmessa dalla frizione ed è stato proposto un modello, basato sull'uso delle reti neurali, in grado di simulare la caratteristica del dispositivo in differenti condizioni d'uso, che può essere usato all'interno di un simulatore di veicolo.

Nell'ultima fase del dottorato, svoltasi in visita presso la University of Toledo (OH), USA, è stato progettato un manicotto scanalato da interfacciare con la frizione, facente uso di molle a memoria di forma.

Contents

Introduction

Vehicle efficiency is one of the most challenging research topics in the last decades. The research on alternative propulsion is very well known even to the large the public opinion. Many efforts are also devoted to the improvement of the overall efficiency of internal combustion engine vehicles.

In this dissertation the development of several magnetorheological clutch prototypes is presented. The research was set in the framework of the funded project *Bando Unico R&S* supplied by Regione Toscana. The activity, coordinated by Pierburg Pump Technology, involved four Italian university departments and was named **Development of a vacuum pump for internal combustion engines disengageable by a magnetorheological clutch**.

In a Diesel engine, the vacuum pump to be disconnected draws air from the power-brake system. The originality of the project lied in the use of smart materials without any active external control and on the strict fail-safe requirements.

Several novel magnetorheological clutches making use of permanent magnet were developed and tested. The activity, besides the fulfillment of the project goal, was also aimed at the characterization of the behavior of magnetorheological fluids in different operating conditions and to the development of comprehensive models.

In this dissertation the activity is extensively described, starting from the environmental and key research motivations (Chapter 1) and from an in-depth literature analysis on magnetorheological fluids and devices (Chapter 2).

The design and experimentation of the conceived prototypes is proposed, along with the analysis of experimental results, in Chapters 3-6. In Chapters 7 and 8 a thermal and neural network based clutch models are developed starting from the experimental results.

Finally, in Chapter 9, an enhancement of the clutch device is proposed, which consists in a sliding spline sleeve, actuated by shape memory alloys springs, which can mechanically engage the clutch as a function of the environmental temperature.

The activities were also illustrated in several research papers [1, 2, 3, 4, 5, 6, 7, 8], from which several parts of the dissertation are drawn.

Acknowledgements I would like to thank some people who supported me during the PhD period. First of all I would like to thank my PhD tutors, prof. Francesco Frendo and prof. Paola Forte, who followed my activities daily with remarkable willingness, addressing my research but leaving a wide space to autonomous choices. Many thanks to Andrea Ferri and Alessandro Franceschini who worked with me on the research project during their MsC theses. We discussed a lot in a very constructive and smart way and they gave a fundamental contribution to the whole project. On Pierburg side, I would like to thank Elisa Bartalesi who followed the activities with pursuance, allowing the whole group to conduct the research rightly; many thanks to Raffale Squarcini and Giacomo Armenio who drove the research with wisdom, always stimulating and pushing the group in the right way. Many thanks to Dr. Mohammad Elahinia who supported me at the University of Toledo and gave me the chance of spending my abroad period gladly. Finally, I would like to thank the Formula SAE team of the University of Pisa, where I spent a lot of time and learned a lot, and its former Faculty Advisor prof. Massimo Guiggiani, who supported me since the BSc degree.

Chapter 1

Background and aims of the research

1.1 Trends in the automotive industry

In the last decades the reduction of fuel consumption and pollutant emissions became challenging research topics for the automotive industry and OEM (original equipment manufacturers). In the TRIAD markets (Japan, Western Europe and North America) government regulations on pollution have been enforced since 20 years ago and are becoming year by year stricter. In particular, the first European emission standard, the Euro 1, was issued in 1993 and nowadays the sixth edition of the standard, the Euro 6, is about to be promulgated. In the USA, the regulations were firstly applied in 1994 (Tier I emission standard), which prescribed maximum levels of consumption and emissions on the basis of the vehicle weight. Nowadays, driven by the strict regulations enforced by the California Air Resources Board (CARB), a second phase is in act and the car manufacturers will be charged if they will not meet the consumption standard indicated by the Corporate Average Fuel Economy, which orders a fuel consumption limit for cars below 35 mpg (14.9 $\mathrm{km\,L^{-1}}$).

In the meantime, new markets are growing up in the rising regions of the world (Fig. 1.1), the so-called BRIC countries (Brazil, Russia, India and China), where the regulations on consumption and emissions are not so strict and the low-cost market does not allow to develop expensive new technologies. Especially in India and in China (Fig. 1.2) the vehicle demands are increasing massively, and they will further increase,

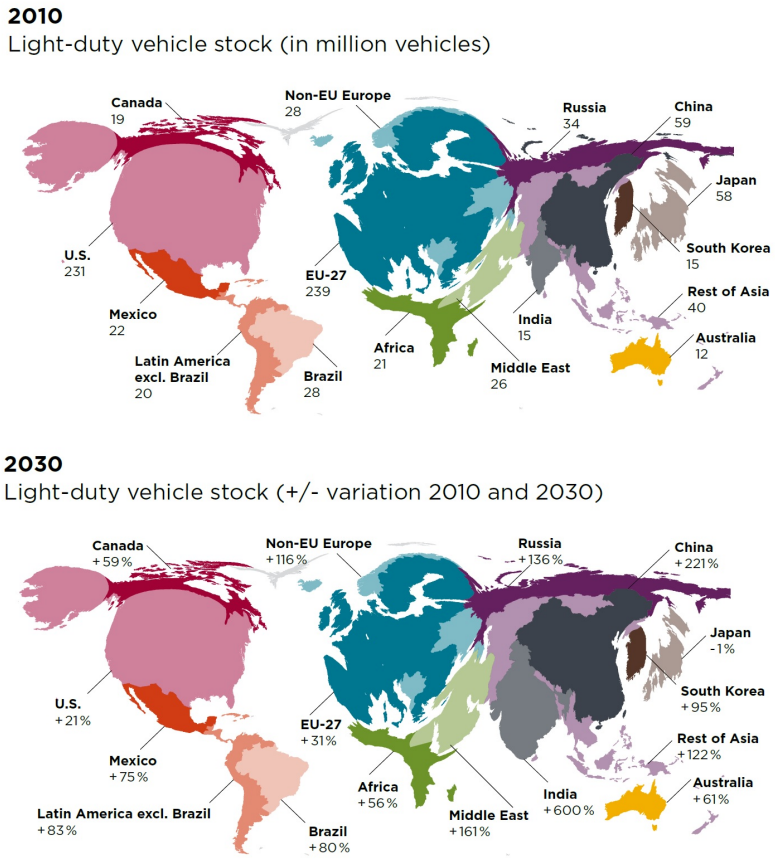

Figure 1.1: Light duty vehicles stock in the world - Comparison between 2010 and expected 2030 amounts - Source: [9]

inducing both the pollution and the oil-demand (Fig. 1.3) to rise.

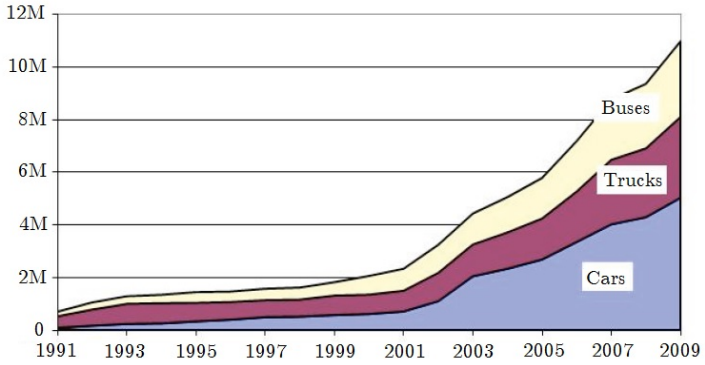

Figure 1.2: Annual vehicle sales in China - Source: [10]

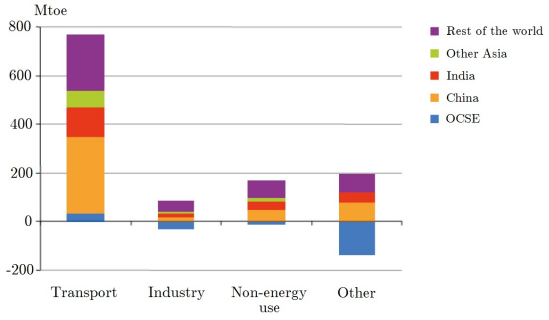

Figure 1.3: Expected oil demand 2006-2030 - Source: [10]

These trends force the countries and the international organizations to control and regulate the vehicle markets in terms of consumption and pollutant emissions (§ 1.1.1). In the same way, the OEM and the vehicle manufacturers are developing new technologies which can fulfill the governments regulations, the customers demand and the cost effectiveness (§ 1.1.2).

1.1.1 Emission and consumption standards

In order to test the vehicles performances in terms of emissions and consumption, several standard cycles have been proposed prescribing a speed profile to be followed by the vehicle, which reproduces the characteristics of a reference path in the urban or in the extra-urban environment.

The most important cycles used nowadays to test vehicles are the NEDC (New European Driving Cycle) cycle for the European market, the CAFE (Corporate Average Fuel Economy) cycle for the US market, and the JC08 cycle for the Japanese market, which are shown in Fig. 1.4. In the growing countries, no standard cycles have been yet accepted. Both the European and the Japanese driving cycles merge in the same

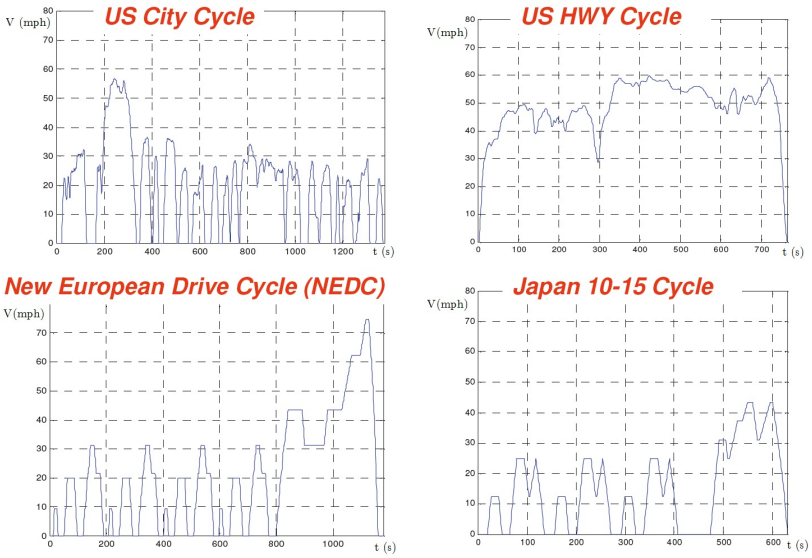

Figure 1.4: American, European and Japanese driving cycles - Source: [10] - [1 mph = 1.61 $\mathrm{km\,h^{-1}}$]

test an urban scenario and an extra-urban one, whereas the US reference cycle considers separately the two scenarios. In addition, in the European countries, the regulations are prescribed looking at the pollutant emissions (grams of CO_2 per kilometer), whereas the American limits are in terms of consumption (miles per gallon [1 mpg = 0.425 $\mathrm{km\,L^{-1}}$]).

The comparison between the current and future emission standards enforced in the main world regions is shown in Fig. 1.5 and Fig. 1.6, in terms of emissions and consumption respectively, both normalized following the NEDC driving cycle. Looking at both the emissions and

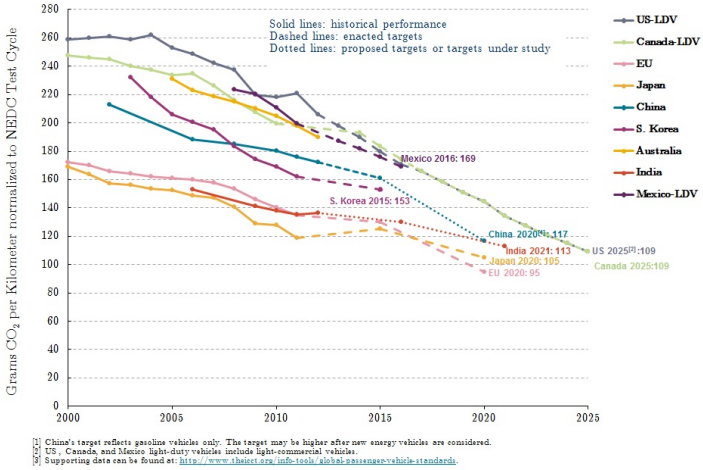

Figure 1.5: CO_2 emission comparison between standard cycles - Source: [11]

the consumption, which, for the internal combustion engines (ICEs), are strictly related, the most virtuous regions are Europe, Japan and India, the worst are the North-American ones, whereas the biggest Asiatic vehicles markets are in an intermediate position. If we consider the perspective for the next 10 years, the gap between America and Europe should reduce, thanks to the effort of the North-American governments (Fig. 1.7), and the efficiency should increase in all the regions.

1.1.2 Technologies and investments of the automotive industry

The OEM and the vehicle manufacturers are striving to fulfill the enforced regulations, both optimizing the current technologies (ICE) and proposing new ones as hybrid or electric vehicles (HV and EV respectively).

An interesting analysis of the automotive market was recently presented by one of the most important professional services company, the Klynveld Peat Marwick Goerdeler (KPMG), in the form of a survey report

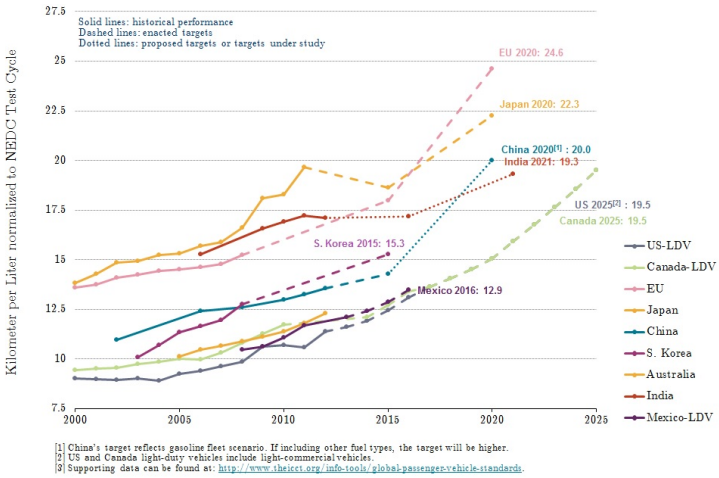

Figure 1.6: Consumption comparison between standard cycles - Source: [11]

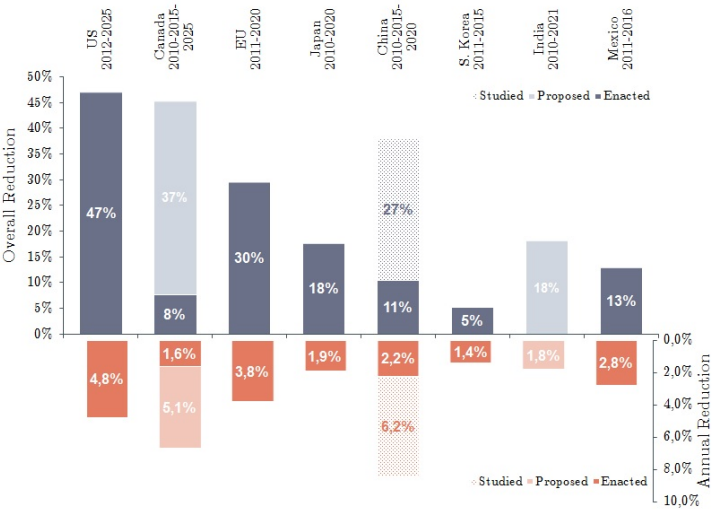

Figure 1.7: Envisaged CO_2 emission reduction - Source: [11]

[12]. The survey was submitted to 200 senior executives from the world's leading automotive companies, including automakers, dealers, financial

service providers, rental companies and mobility service providers.

The first point which comes out from the report is how the investments on powertrain technologies are almost equally split between ICE downsizing and plug-in hybrid development, but the main part of the R&D resources are still allocated to the development of ICEs.

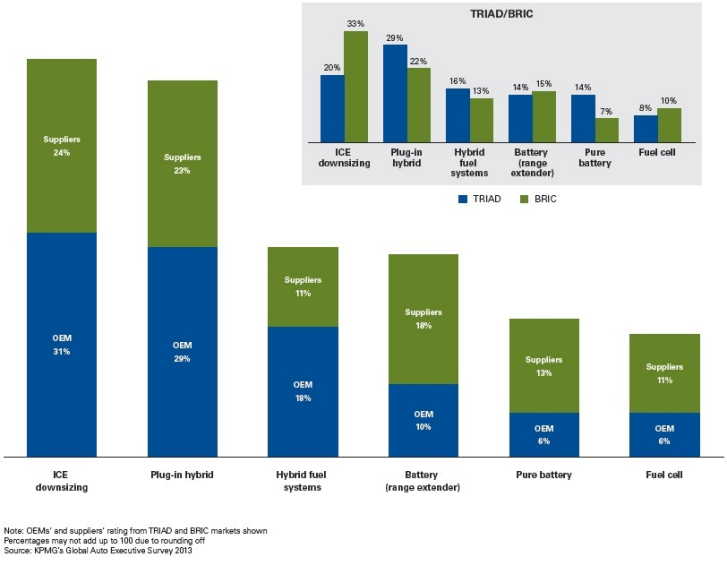

Figure 1.8: Main investments in powertrain technologies (2014–18) - Source: [12]

Indeed, the forecast for the next years is to have ICE still present in the market, holding the main segment up to 2030, as shown by two different analyses in Fig. 1.10 and Fig. 1.11.

For this reason the research on conventional engines is still in progress and deals mainly with:

- the optimization of the power to weight ratio, for both the engine and the whole vehicle;
- the reduction of friction losses;
- the reduction of losses due to the auxiliary devices systems

Usually, the vehicle manufacturers cope directly with the first problem, trying to meet the request of the governments in terms of consumption

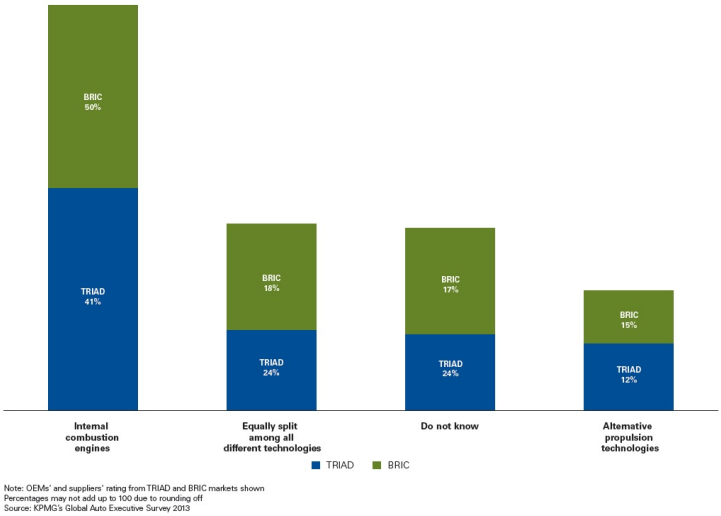

Figure 1.9: Current allocation of R&D powertrain resources - Source: [12]

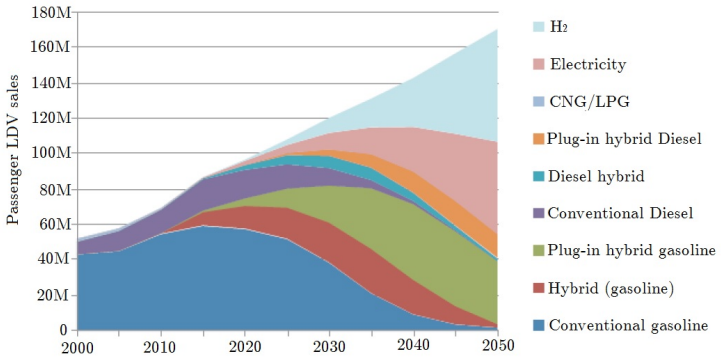

Figure 1.10: Light duty vehicle sales forecast - Source: [10]

and pollution, reducing the engine size (Fig. 1.12), together with the requests of the customers, which desire bigger and safer cars, as proved by Fig. 1.13.

It is worth noting that in 2009 there was an interruption of the weight increasing trend, which can be attributed both to the economical crisis

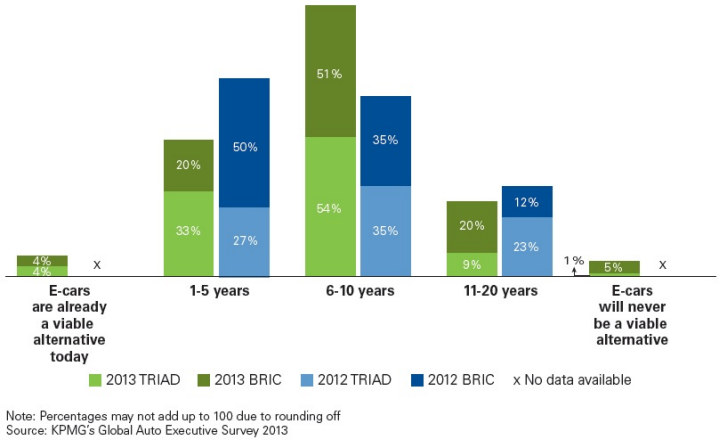

Figure 1.11: Time period in which ICE offers the greatest potential for clean, efficient engines - Source: [12]

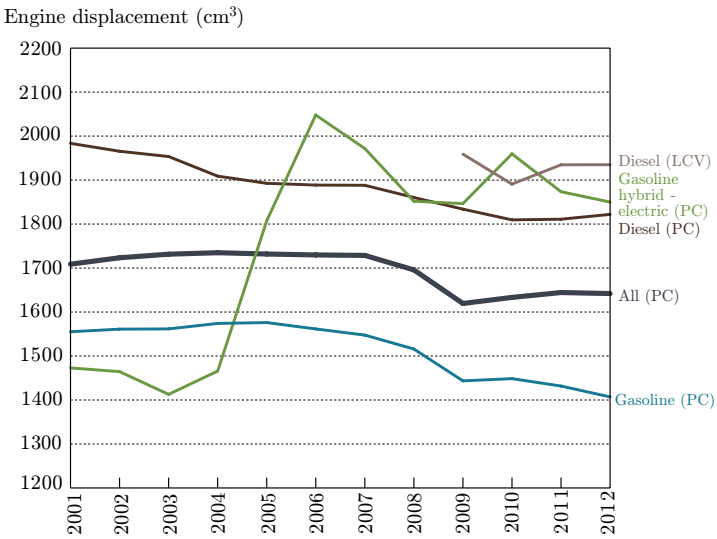

Figure 1.12: Engine displacements for new vehicles - Source: [12]

and to the emission of Euro 5 emission standard.

The reduction of friction and auxiliary losses are usually in charge of the OEM, which have to develop more efficient devices (e.g. oil pumps,

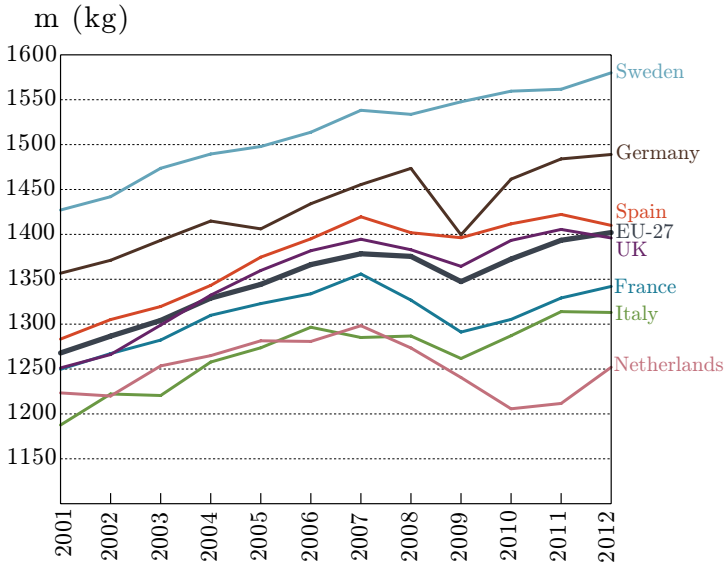

Figure 1.13: Passenger cars: vehicle mass in running order- Source: [12]

water pumps, vacuum pumps, air-conditioning systems etc.). It was in this context that the PhD research project came into being. In particular it was aimed at reducing the power absorption the ICE vacuum pump, supplied for several passenger vehicles by Pierburg Pump Technology - Stabilimento di Livorno (PPT in the following) through:

- increasing the pump efficiency using new materials and new pump geometries;
- developing a new device, based on the use of magnetorheological fluids, which can disconnect the vacuum pump when it is not necessary (see Chapter 3), avoiding the related losses.

The project was funded by *Regione Toscana* in the framework of the Bando Unico R&S 2008 and involved three Italian universities (University of Pisa, University of Bologna, Polytechnic Institute of di Torino) and Pierburg Pump Technology. The University of Pisa took part in the activity with two research teams from the Department of Civil and Industrial Engineering (*Italian achronim* DICI) and the Department of Energy, Systems, Territory and Constructions (*Italian achronim*, DESTEC).

1.2 Magnetorheological fluids and vehicles

The use of smart materials in vehicle applications is not a novelty. Indeed, the unconventional characteristic of these materials to change their constitutive properties in dependence of external parameters, as the temperature, the magnetic or electric fields, the stress which they are subjected to etc., made them of large interest. Some examples of the most widespread smart materials are:

- **piezoeletric materials:** can produce voltage when subjected to stress or vice versa;
- **shape memory alloys:** can change their deformation as a function of temperature and stress due to the martensitic transformation;
- **ferrofluids and magnetorheological fluids:** can change their rheological properties (viscosity and yield stress) if they are subjected to magnetic fields;
- **electrorheological fluids:** can change their rheological properties (viscosity and yield stress) if they are subjected to electric fields.

Nowadays, this kind of materials is a challenging research topic and the automotive industry is interested in it, mainly because smart materials can actuate systems or change their constitutive properties by imposing external parameters.

Recently an entire book has been published on the use of magnetorheological fluids (MRF) on vehicle systems [13]. The most important applications are listed in the following sections, whereas a detailed description of the behavior of MRF is proposed in Chapter 2.

Magnetorheological suspension systems The automotive suspension elements can be classified, among the others, on the basis of the capability to change their response actively. The traditional suspensions, composed by classical springs and dampers, are called *passive suspensions*. Their response is determined by the spring and damper characteristics, which can not be varied during the car operation. On the other hand, the *active suspensions* combine traditional elements and electric actuators, in order to change the suspension response on the basis of the road profile input. The results in terms of comfort and car-performance which can be achieved by the active suspension are good but their complexity is high

and the reliability is lower if compared to conventional ones. In particular, active suspensions require many sensors to monitor the suspension state and high power sources to allow the actuators to exert high force values.

An intermediate solution is the *semi-active suspension system*, which makes use of tunable components (usually dampers) whose properties can be controlled as a function of the input road profile. This system requires sensors to monitor the suspension state and a control unit to change the parameters which adjust the damper properties, but does not require any force actuator.

The MR dampers belong to the *semi-active suspension system* class. The damping response, in terms of force vs. damper speed, can be varied as a function of the magnetic field applied to the damper. In Fig. 1.14 the damping characteristic of a commercial device (Rheonetic ® damper, [14]), produced by *Lord Corporation Ltd*, is shown.

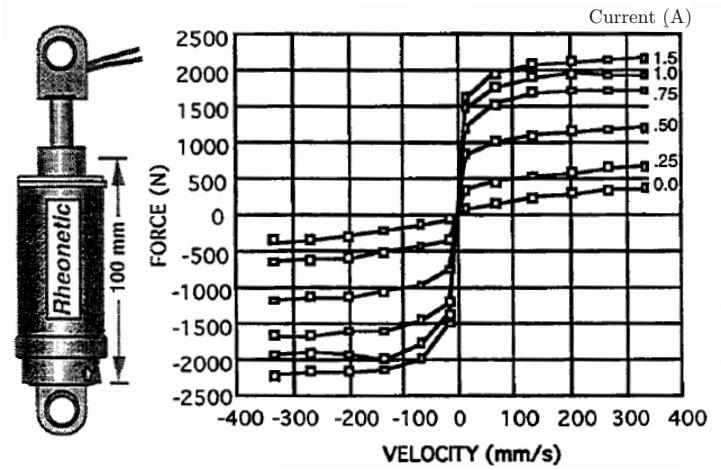

Figure 1.14: The Rheonetic ® damper characteristics - Source [14]

If no current is applied to the damper coils, no magnetic field is produced and the dynamic response is identical to the dynamic response of a traditional damper with the same geometry and the same fluid viscosity. If the current is applied, the damper response changes, increasing the stiffness as the current rises, due to the increased apparent viscosity of the MRF.

In the literature two different damper architectures are usually pro-

posed. The first one has the coil fixed on the damper case and an oiltight piston which can move axially. The MR fluid is forced by the piston to flow within calibrated orifices, as shown in Fig. 1.15. In this architecture, as in conventional dampers, the fluid behaves in flow mode (see Chapter 2) and the damping effect is related to the apparent viscosity of the fluid

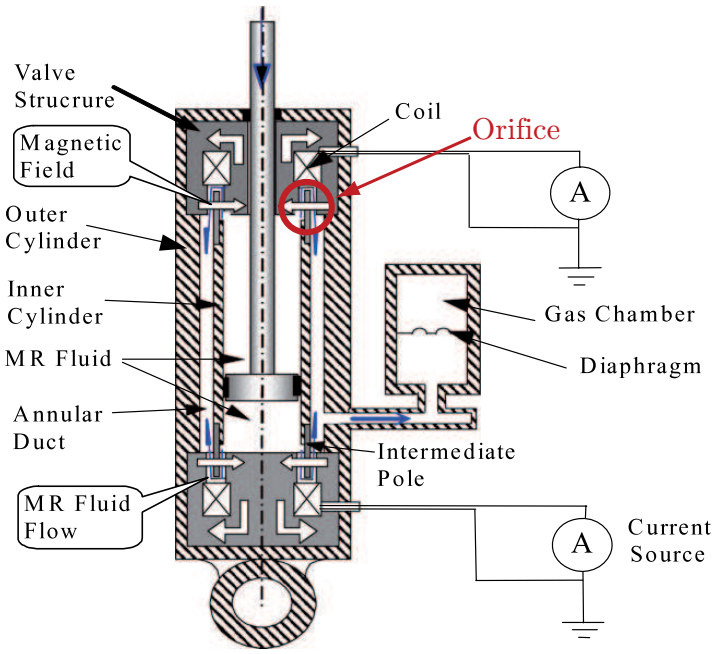

Figure 1.15: A flow mode MR damper - Source [15]

The second architecture shown in Fig. 1.16 has the coils embedded into the piston and the fluid can flow in the gap between the piston and the cylinder. In this case, the way of exploiting the fluid properties is a mix of the flow and the shear mode (see Chapter 2).

MR engine mounts and impact-absorbers Internal combustion engines are an important vibration source in passenger vehicles. In order to reduce the noise and vibration perceived by the passengers, passive mounts are usually fixed between the engine and the chassis. Recently, controllable engine mounts have been proposed in order to improve the vibration mitigation for different engine speed values. Some

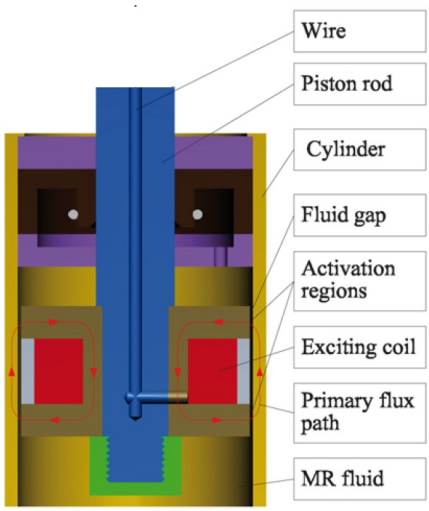

Figure 1.16: A flow mode MR damper - Source [16]

of these controllable mounts are based on electrorheological (ER) and magnetorheological fluids.

The MR-based engine mount shown in Fig. 1.17 was recently proposed by [17]. It is composed of an upper and a lower rod (no. 10 and no. 12) which are connected to the engine and the chassis respectively. The core of the system, enclosed by the gaskets no. 1 and no. 2, is filled with MR fluid, which can flow in the gap no. 7 and is compressed between the plates no. 4 and no. 11. The system includes two coils, the no. 5 coil which generates the magnetic field in the gap no. 7 and the no. 3 coil which generates the magnetic field between the two parallel plates.

As the mount moves, the magnetic field in the gap is almost constant, whereas the magnetic field between the plates varies as a function of the distance between the plates, guaranteeing different damping response for different mount compression values.

Similarly, ER and MR mount dampers are also used in impact mitigation [18].

Magnetorheological brakes and clutches The oldest application of MRF was a clutch (see Chapter 2) and in the present-day MR clutches are still one of the most studied and used MR devices. By comparing

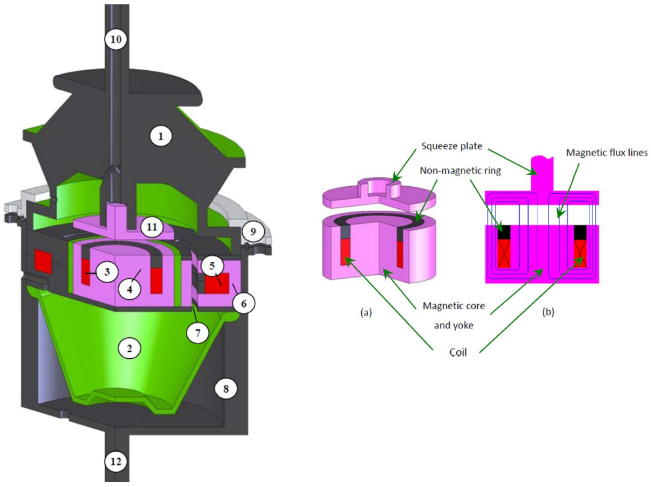

Figure 1.17: Orbit radius - Source [17]

clutches and brakes, no prominent conceptual difference can be found and these may be used indifferently only with small adjustments to their interfaces.

In the literature several papers were proposed on the simulation process aimed at dimensioning the automotive magnetorheological brakes [19, 20, 17, 21] considering also the brake self-heating. The only paper which deals with prototype testing of a MR brake shown in Fig. 1.18 is [22].

As the authors state, the agreement between simulation and experimental results is good, but the brake performance (see Tab. 1.1) is far from that of a conventional friction brake (breaking torque more than 2000Nm).

Some different applications deal with magnetorheological clutches and limited slip differentials. In [23] a MR clutch for automotive transmission is proposed, which incorporates a highly absorbent polyurethane foam to reduce the centrifuging of fluid particles. However, the maximum transmitted torque is about 11 Nm, which is one order of magnitude lower than the torque transmitted by traditional transmission clutches or torque converters. In [24] a high-torque limited slip differential for automotive transmission was developed and tested and its drawing is shown in Fig. 1.19. The differential consists of 46 plates, arranged in a

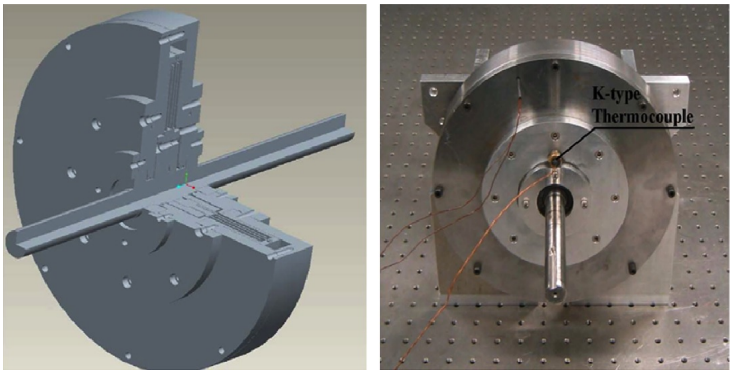

Figure 1.18: A MR automotive brake - Source [22]

Weight (kg)	11.8
Diameter (mm)	240
Number of discs	2
Volume of MRF used	205 cm^3
Coil wire diameter (mm)	0.77
Number of turns	236
Maximum current (A)	1.8
Maximum braking torque (Nm)	23

Table 1.1: MR automotive brake characteristics

57 mm outer diameter inner casing which has a total length of 114 mm. By controlling the current in the external coil, the slippage torque can be controlled up to 250 Nm (3 A current input).

Another application of MR clutches deals with the control of the cooling system in internal combustion engines, by means of a MR fan clutch [25]. The fan clutch can be connected to or disconnected from the leading motor by controlling the current supplied to the MR clutch. The current is controlled on the basis of the engine temperature and is conceived in order to guarantee clutch engagement when the engine temperature is higher than a threshold value. On the basis of MR properties and clutch dimension, the use of MR clutches to manage auxiliary devices seems more promising than the use as a transmission clutches.

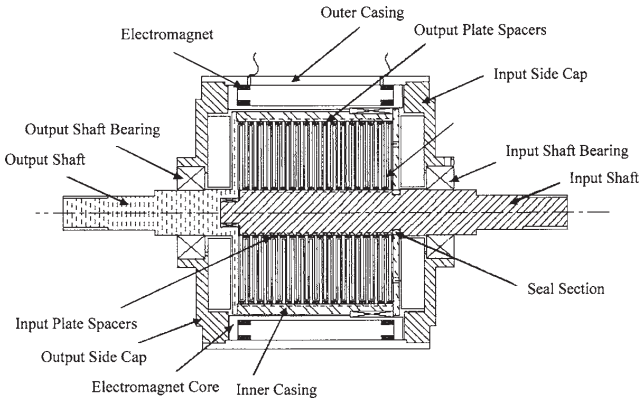

Figure 1.19: A MR limited slip differential - Source [24]

Chapter 2

Magnetorheological fluids

The first application of magnetorheological fluids dates back to 1948, when Jacob Rabinow presented a so-called *magnetic fluid clutch* [26, 27], which made use of MR fluids excited by a magnetic field produced by electromagnetic coils.

In more recent years, MR fluids have been used mainly for dampers and biomedical applications [28]. Recently a book has been published which gathers much information on the state of the art of MR fluis [29].

2.1 Composition and characteristics

Magnetorheological fluids are non-colloidal suspensions of polarizable particles, whose size is of a few micrometers. The most important and original property is the change of their rheological behavior depending on the magnetic field which they are subjected to. Indeed, by applying a magnetic field, the suspended particles in the fluid polarize and the resulting dipoles align in columnar structures, which arrange themselves parallel to the magnetic field. An idealized representation of the particles arrangement is shown in Fig. 2.1, while a SEM microscopy of actual cobalt fibers in a carrier fluid is shown in Fig. 2.2.

The carrier fluids are usually hydrocarbonil oils but water or silicon oils are often used [30]. The dispersed particles size is typically in the range 1-10 µm (three order of magnitude greater than in ferrofluids) and they have to be ferromagnetic. The maximum interparticle attraction and the MR effect depend directly on the saturation magnetization of the particles. Usually the following materials are employed: powdered iron,

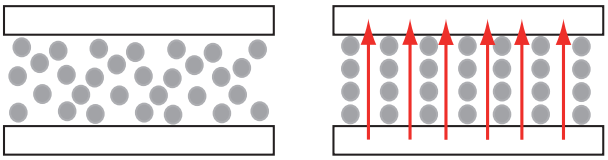

(a) Without magnetic field (b) With magnetic field

Figure 2.1: Particles suspension in carrier fluid

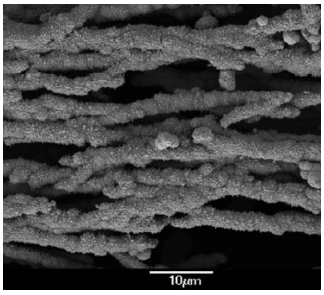

Figure 2.2: SEM microscopy of cobalt particles suspension - Source: [29]

water- or gas-atomized iron, nickel alloys, iron/cobalt alloys, magnetic stainless steels, and ferrites. However, the most widely used material for MR fluid particles is carbonyl iron.

The volume fraction of the particles is usually in the range 20–45%. The choice of the right volume fraction is a trade off between the capability of the fluid of transmitting shear stress and the fluid viscosity; both increase as the volume fraction rises, but they have opposite effect on the MR fluid effectiveness. In general, a high value of shear stress is desirable when the fluid is magnetized, whereas an high value of the viscosity might be a handicap for the unmagnetized fluid.

The size distribution of the particles is a key-factor in the MR composition, and several studies and patents were proposed on this topic [31, 32, 33].

Many additives can be added to the mixture, to make the fluid more stable and durable, prevent sedimentation and agglomeration, enhance lubricity, prevent oxidation, modify viscosity and inhibit wear. Sedimentation is typically controlled by the use of organic or inorganic thixotropic

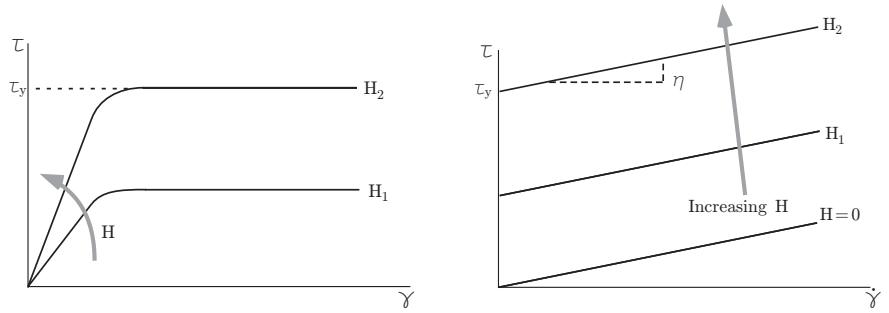

(a) Shear stress vs. Strain (b) Shear stress vs. Shear rate

Figure 2.3: Mechanical properties of MRF

agents and surfactants.

The typical mechanical characteristics of MRF are presented in Fig. 2.3 as a function of the magnetic flux density H. The shear stress vs. shear rate characteristic (Fig. 2.3(a)) points out an elasto-perfectly plastic behavior of the fluid. The shear modulus G, defined as the ratio of shear stress to shear strain, rises as the magnetic flux density increases. The plastic stress threshold, usually called yield stress τ_y, is the value beside which the fluid flow starts and after that the stress is rises monotonically with H. Several studies were proposed on how to measure accurately the shear stress of MRF and ferrofluids [34, 35, 36]. Some strategies of increasing the yield stress were proposed operating on the fluid composition or on the fluid pressure [37, 38].

The fluid viscosity η, defined as $\frac{\mathrm{d}\tau}{\mathrm{d}\dot{\gamma}}$, is, to a first approximation (see § 2.3), constant and independent from the magnetic field. More in depth studies consider also the dependence of the viscosity on the shear rate, highlighting the shear thinning behavior of MRF [39].

The most popular MR fluid supplier is Lord Corporation Ltd. which currently produces three different fluids [40], whose properties are listed in the Appendix. The three fluids (MRF-122EG, MRF-132DG, MRF-140CG) have different particle volume fractions and consequently different yield stress and viscosity values. Others suppliers are BASF [41] and Liquid Research [42].

2.2 MRF operational modes

The MRF properties are usually exploited in three different ways [43]: flow mode, shear mode and squeeze mode.

Flow mode It is used in dampers and shock absorbers. It consists in imposing relative motion between the fluid and two rigid elements (Fig. 2.4) under the effect of a magnetic field perpendicular to the surfaces.

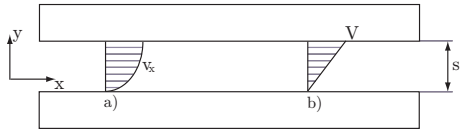

Figure 2.4: Flow mode

The pressure p which is necessary to let the fluid flow in the gap can be computed as the sum of the viscous pressure p_v and the magnetorheological pressure p_{MR}[43]. Assuming rectangular surfaces:

$$p = p_v + p_{MR} = \frac{12\eta QL}{s^3 w} + \frac{f\tau_y L}{s} \tag{2.1}$$

where η is the viscosity of the fluid, Q is the flow rate and L, w are the length, the width of the plates respectively, while s is the gap thickness and f is an empirical factor which has to be determined experimentally.

Shear mode The shear mode is the way of exploitation of clutches and brakes. In this case, the fluid is fenced between two rigid elements, which can move relatively (Fig. 2.5) and a magnetic field is imposed perpendicularly to the surfaces.

Assuming rectangular plates, the force F which is necessary to move the upper element in Fig. 2.5 at a given speed V is composed of a viscous term F_v and a magnetorheological term F_{MR}

$$F = F_v + F_{MR} = \frac{\eta V L w}{s} + \tau L w \tag{2.2}$$

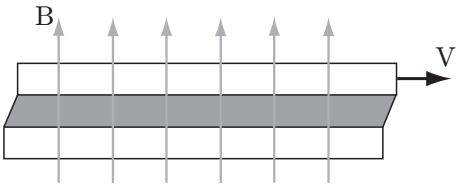

Figure 2.5: Shear mode

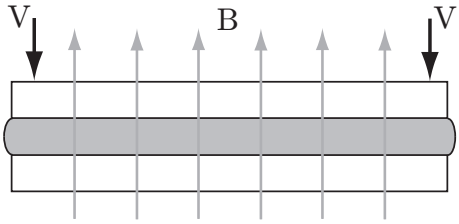

Figure 2.6: Squeeze mode

Squeeze mode It is the less diffused MRF operating mode and it consists of shrinking the MRF between two plates in presence of a magnetic field perpendicular to the plates (Fig. 2.6).

A detailed description of this operating mode can be found in [44].

2.3 MR fluids models

MR fluids belong to the non-Newtonian fluid category [45]. A useful overview on MR fluids was presented in [43] where the rheological behavior of fluids is described by two physical quantities, the shear stress τ and the viscosity η, both in terms of the shear rate $\dot{\gamma}$. These quantities, in one-dimensional representation, were defined by Newton and, with reference to Fig. 2.4, are related by the following relationship

$$\tau_{yx} = \eta \frac{dv_x}{dy} \tag{2.3}$$

which, if the Couette hypotheses are verified [46], can be reduced to

$$\tau_{yx} = \eta \frac{V}{s} \tag{2.4}$$

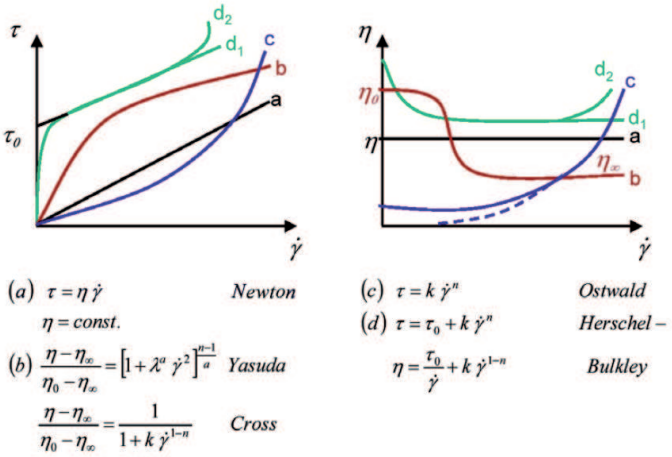

Figure 2.7: Different fluid behaviors - Source [43]

where the ratio $\frac{V}{s}$ corresponds to the viscosity η.

The rheological behavior of MR fluids is usually modeled by the Bingham-plastic (BP) model [47, 48]. The model was conceived more than 30 years before the experimentation on MR fluids and describes the behavior of non-Newtonian fluid which present a shear yield stress threshold τ_y to be overcome, before the fluid starts to flow. Once the flow is started, the increase of shear stress is proportional to the shear rate. The BP law is expressed in Eq. 2.5

$$\tau \begin{cases} \leq \tau_y \operatorname{sgn}(\gamma) & , \dot{\gamma} = 0 \\ = \tau_y \operatorname{sgn}(\dot{\gamma}) + \eta\dot{\gamma} & , \dot{\gamma} \neq 0 \end{cases} \tag{2.5}$$

In MR fluids, the shear yield stress is related to the magnetic flux density H in the fluid, as stated in the supplier data [40], whereas the viscosity η is independent (Fig. 2.8). If no magnetic field is applied, the BP model is usually made equal to the Newtonian model, neglecting the yield stress threshold for the unmagnetized MR fluid.

Another useful model used for MR fluids was proposed in 1926 by Herschel-Bulkley (HB) [49]. As the BP model, it presents a shear yield stress threshold to be overcome to have fluid flow, followed by a power

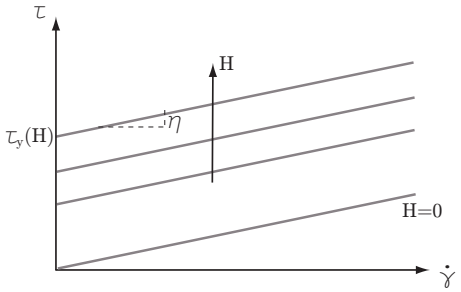

Figure 2.8: Bingham-plastic model

law.

$$\tau(H)\begin{cases} \leq \tau_y \operatorname{sgn}(\gamma) & , \ \dot{\gamma} = 0 \\ = \tau_y \operatorname{sgn}(\dot{\gamma}) + K\dot{\gamma}^n & , \ \dot{\gamma} \neq 0 \end{cases} \tag{2.6}$$

The parameter K is usually called consistency, whereas the power index n denotes the effect of the shear rate on the fluid viscosity. If $n < 1$, as usually happens in MR fluids, the fluid has the shear-thinning behavior, whereas if $n > 1$ the fluid has the shear-thickening behavior. It is worth noting that the HB model is equivalent to the BP model if $n = 1$ and, consequently, $K = \eta$.

An interesting comparison between the BP and MR model was proposed in [50] and it is deepened in Chapter 4. Figure 2.9 shows a qualitative comparison between the two models. It is worth noting that, in general, the shear yield stress for the two models could result different (see Chapter 4).

Recently, new phenomenological models [51] have been developed starting from the classical ones. An empirical model has also been proposed to find the relationship between the particle volume fraction and the shear yield stress threshold of MR fluids [52]. The constitutive equation is

$$\tau_y = 271700\, C\, \phi^{1.5239} \tanh\left(6.33\, 10^{-6}\, H\right) \tag{2.7}$$

where C has a constant value which equals 1.0, 1.16 or 0.95 depending on whether the carrier fluids are hydrocarbon oil, water or silicon oil, H is the magnetic field expressed in $\mathrm{A\,m^{-1}}$ and ϕ is the volume particle density.

In [53] an analytical model, which can be applied in presence of a magnetic field not perpendicular to the fluid gap, is proposed.

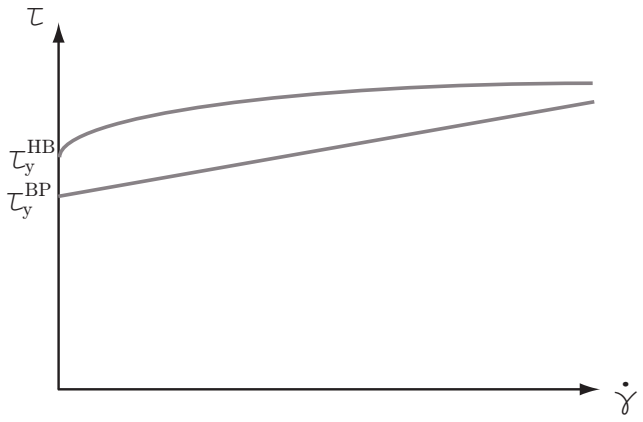

Figure 2.9: Bingham-plastic and Herschel-Bulkley models

At a lower scale, several micro-mechanical models have been proposed to investigate the magneto-mechanical interactions between the particles in the fluid [54, 55, 56], but they were not used in the present work.

2.4 MR devices

Even if some MR devices have been already described in § 1.2, an additional paragraph is mandatory to have a wider overview on MR devices, even if they are not applied to vehicles and vehicle systems.

2.4.1 MR dampers

The most diffused category of MR devices are the MR dampers. The first prototype of MR damper was commercially developed by Lord Corporation Ltd. in the 90s and several MR geometries are described in the patent [57]. The most important application of MR dampers are civil structures, automobiles and railway vehicles. On the basis of the motion of the piston, the dampers can be categorized as linear and rotary dampers.

Concerning civil applications, a review was presented in 2004 [58], and the most cited paper [59] deals with the control of a linear damper for mitigating the seismic effects. Figure 2.10 shows a scheme of a damper for civil applications , which has the coils embedded into the axial piston.

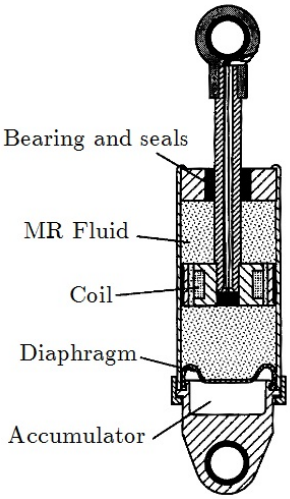

Figure 2.10: Scheme of a MR damper used for seismic applications - Source [59]

The magnetic field in the fluid can be varied as a consequence of the electric tension applied to the coil, and the resulting force is shown in Fig. 2.11.

The characteristic of the MR damper is usually modeled by the Bouc-Wen model [50], which takes also into account the hysteresis effect. A scaled model of a building was considered, and the control unit was set to induce the right voltage time history to the coils, in order to achieve the optimal control of the modeled system.

Some examples of automotive suspensions and mount systems have been proposed in § 1.2.

Concerning the rotor dampers, some interesting examples of MR devices were presented in [60, 61]. In particular, in [61] a drum type dumper was proposed, where the thickness of the MR gap depends on the eccentricity between the two axes connected to the damper. The device was used to mitigate the vibrations of an unbalanced rigid rotor, by changing the electric tension applied to the coils and consequently the rheological properties of the fluid.

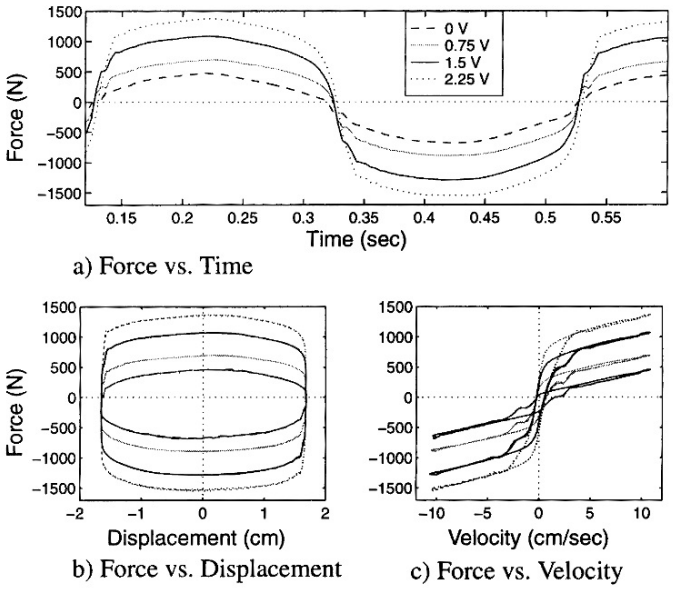

Figure 2.11: Force diaphragms for the axial damper - Source [59]

2.4.2 MR clutches and brakes

As soon as the MRF properties were discovered [26], several MR clutches architectures were patented. In Fig. 2.12-2.15 some examples of geometries are shown, drawn from the Rabinow patent [27].

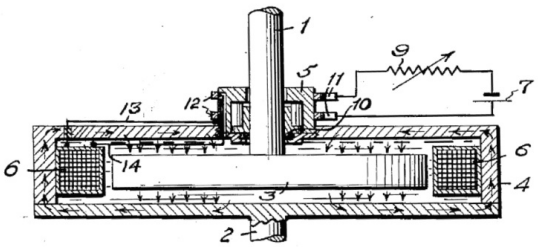

Figure 2.12: MR clutch with coils and plane gaps - Source [27]

In the first patent, several clutch geometries were proposed, including the more basic gap geometries, as the single disc or the single cylinder

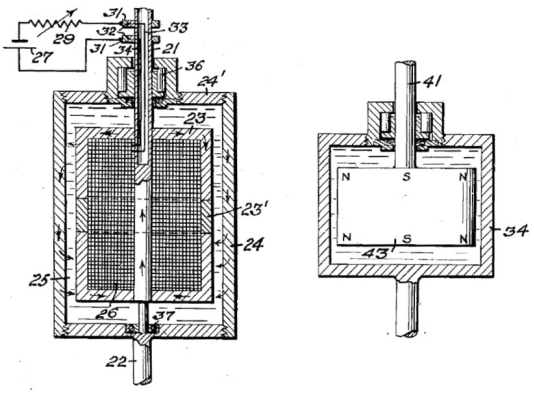

Figure 2.13: MR clutch with coils or permanent magnet and cylindrical gaps - Source [27]

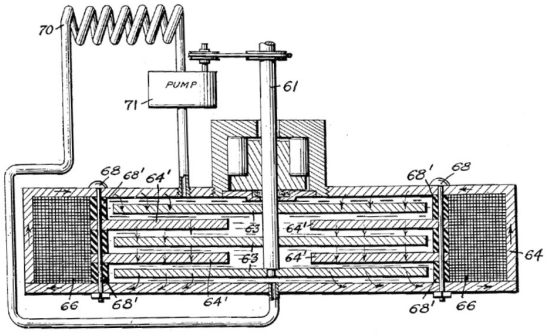

Figure 2.14: MR clutch with coils and multi-disc gaps - Source [27]

ones, up to more elaborated ones with multi-disc configurations or variable gap size. Even the use of permanent magnet (PMs) was proposed since the beginning.

Thereafter, few MR clutches were developed, mainly due to the weaknesses in the MRF production and in the control of the magnetic field. In the 90s, a commercial device was proposed by Lord Corporation [14], based on plane disc gaps and coils. In the 2000s, several research papers and patents dealing with MR clutches and brakes with classical geometries were presented (e.g. [62, 23, 63, 64, 65]), which made use of

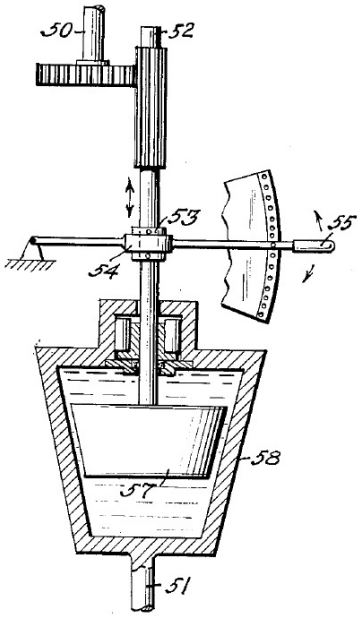

Figure 2.15: MR clutch with variable thickness gap - Source [27]

coils to generate the magnetic field.

Recently some innovative applications of MR clutches were proposed in [66, 67], for physical rehabilitation and biomedical devices. In particular biomedical applications make use of very compact devices, where the MR gap is reduced up to 50 µm.

The gap geometry was examined in depth in [17, 68, 69], where the optimization algorithms were used to design the gap shape.

In [70] and [71] the MR clutch was integrated in a multi-purpose coupling device, whereas in [72] the complex geometry shown in Fig. 2.16 was proposed to enhance the torque transmission.

Few papers and patents considered the use of permanent magnets. In particular, in patent [73], a variable gap size clutch with permanent magnet was presented but no information is provided about its realization and testing. Also in patent [74] a reference to the use of PMs is made. Concerning research papers, an interesting study was proposed in [75], where a fail-safe MR clutch is presented. In this application, the magnetic field in the gaps is normally generated by a PM, which guarantees the

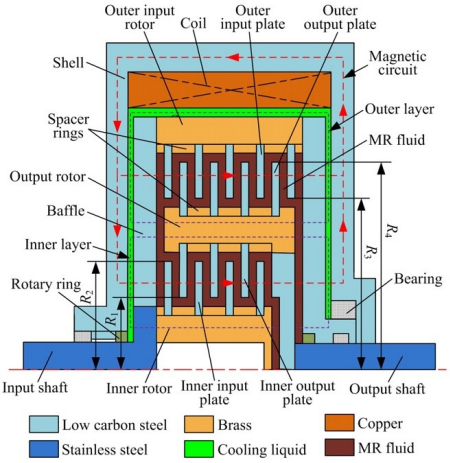

Figure 2.16: A two-layer multi-disc MR clutch - Source [72]

clutch to be engaged continuously. When the clutch has to be disengaged, a magnetic field is generated by coils, opposed to the one generated by the PM, making the total magnetic field theoretically equal to zero. A drawing of the system is shown in Fig. 2.17.

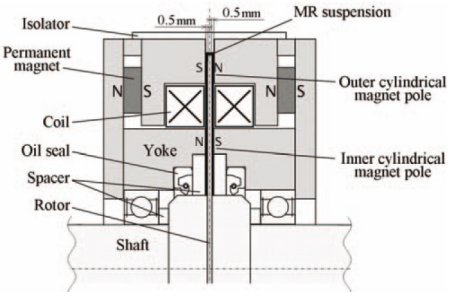

Figure 2.17: A combined PM-coils clutch - Source [75]

Recently, in [76], an enhanced version of the device making use of PMs and coils described in [75] was proposed, where the coils can be used to cancel or increase the magnetic field in the MR gap, by varying the current direction.

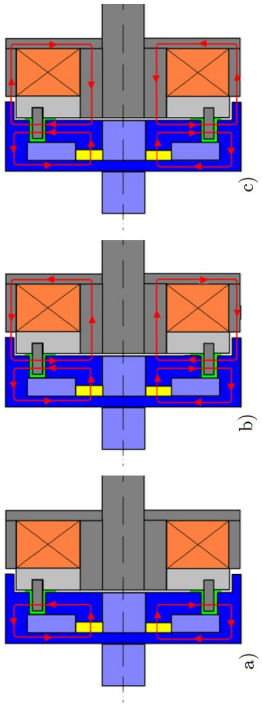

Figure 2.18: A combined PM-coils clutch - Source [76]

Chapter 3

Development of a MR clutch for the disengagement of vehicle auxiliaries

As described in the previous chapter, in the literature many magnetorheological clutches have been proposed. In almost all the clutches, the magnetic field is generated by coils and can be controlled by the applied electric tension. Besides being controllable, MR clutches have also the advantage, with respect to conventional clutches, of not requiring axial loads to transmit the torque and, in case of clutch slip, no appreciable wear arises. For these reasons, which will be examined in depth in the following sections, the development of a MR clutch was envisaged to disengage the vacuum pump of Diesel engines from the cam shaft.

3.1 The vacuum pump and power-brake system

The vacuum pump is assembled in all the Diesel engines and almost all the petrol engines and it is used to draw air from the auxiliaries which need operating pressure below the atmospheric one. The most important device connected to the vacuum pump is the power-brake system, either due to the amount of air to be drawn or to safety reasons. Other devices which can be connected to the vacuum pump are the turbo-system and the air conditioning system.

3.1.1 The power-brake unit

The power-brake unit is placed between the brake pump and the pedal and it is conceived in order to amplify the force applied to the pedal by the driver, exploiting the difference of pressure between two chambers which are separated by a membrane (Fig. 3.1). In normal driving condition, when the brake pedal is not pushed, both chambers of the power unit are connected to the vacuum pump and, in steady condition, the pressure in the chamber is below the atmospheric pressure (usually 0.2 bar).

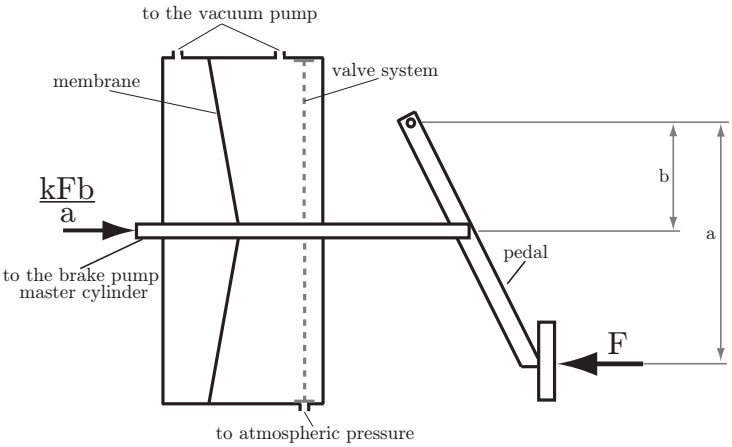

Figure 3.1: Power-brake conceptual sketch

When the force F is exerted on the brake pedal, the valve system (see [77] for the detailed description) connects the right chamber to the atmosphere, producing a difference of pressure between the two sides of the membrane. The reaction force on the left side of the power-brake rod, which is equal to the force which acts on the master cylinder of the brake pump, is amplified by a factor k. The amplifying factor is equal to 1 when the pressure is the same on both the membrane sides, whereas it is greater than one if a difference of pressure occurs.

3.1.2 The vacuum pump

The vacuum pump supplied by PPT, which is shown disassembled in Fig. 3.3, is a volumetric machine which is connected to the cam shaft of the vehicle engine (Fig. 3.2) by means of a Holdam joint. Its role is to

draw air, mainly from the power-brake chambers.

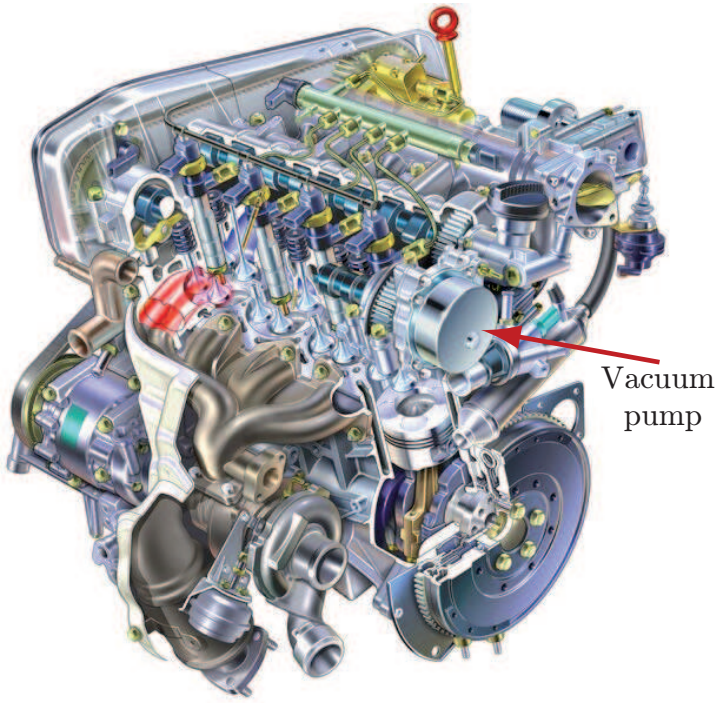

Figure 3.2: The vacuum pump in a 4-cylinder engine

It is composed of an external pseudo-cylindrical case, within which two skids can slide, lubricated by the engine oil. The skids are led by a palette, which can slide into the rotor, which is set in motion by the cam-shaft. The palette and the rotor split the vacuum pump volume into three chambers, which volumes vary during the volumetric cycle.

Two holes, the inlet and the exhaust one, on the pump casing connect the chambers to the power-brake and to the atmosphere respectively. The shape of the external case is designed in order to get a pressure value at the inlet hole lower than the atmospheric pressure, in order to draw air from the power-brake.

Starting from the atmospheric pressure, the vacuum pump succeeds in drawing air from the power-brake chambers up to the steady value of the pressure ($\simeq 0.2$ bar) in less than 20 s.

The torque absorbed by the vacuum pump is not constant during the

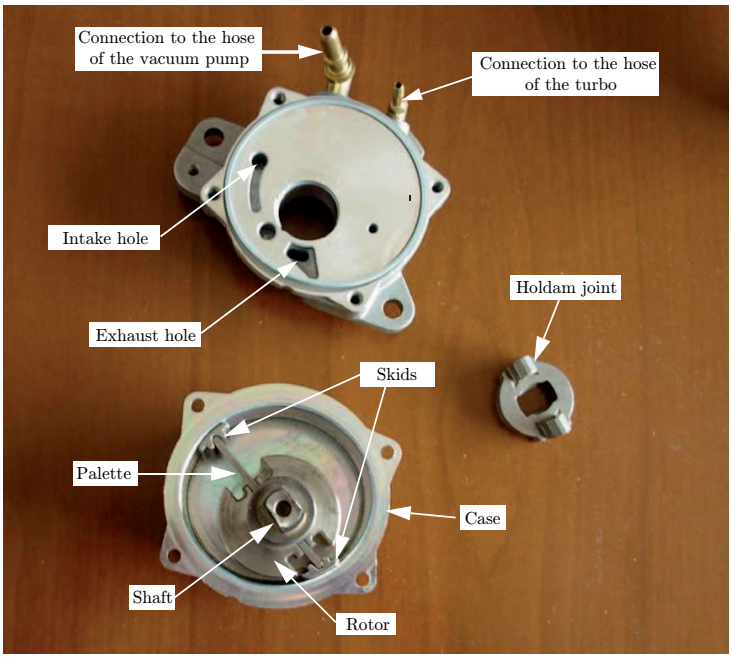

Figure 3.3: The vacuum pump components

cycle and it depends on several factors. A reference average value of the torque absorbed by the vacuum pump is shown in Fig. 3.4 as a function of the speed of the cam-shaft, which is half the engine speed.

The power dissipated by the vacuum pump at the maximum engine speed is more then 0.4 kW.

3.1.3 The unplugging device proposal

In order to reduce the energy dissipated during car operation due to the vacuum pump absorption, two different strategies were conceived:

- reducing the power loss due to friction and pneumatic reasons;
- designing an innovative fail-safe device, using magnetorheological fluids, aimed at unplugging the vacuum pump from the cam-shaft when it is not needed.

The former is a common strategy, which is pursued for all the engine devices. The latter is more original and specific for the application. Indeed,

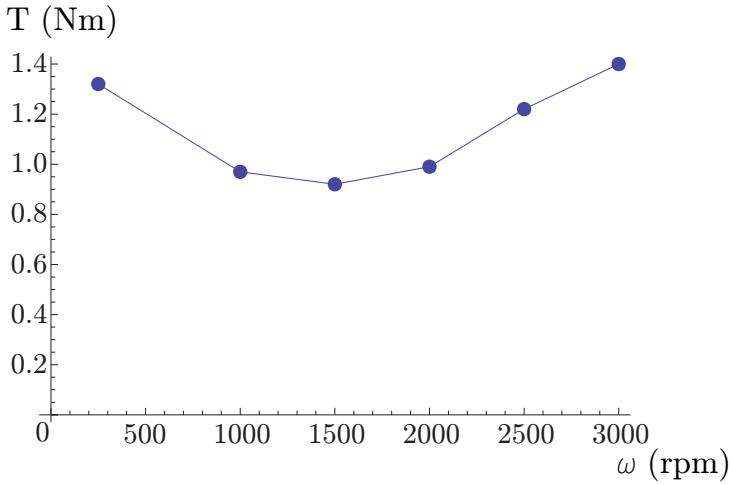

Figure 3.4: Torque absorbed by the vacuum pump as a function of cam-shaft speed

especially during the extra-urban drive, the vacuum pump continuously absorbs energy, even if the brake pedal is rarely pushed. For this reason, the vacuum pump could be disconnected from the cam-shaft when the desired pressure value in the power-brake chambers were reached, and re-connected once the pedal is pushed.

On the basis of PPT specifications, the unplugging device has to be autonomous, sensor-less and fail-safe and the MR clutch proved to be a good hypothesis to be studied.

3.2 Design background

Some examples of MR clutches which were useful in the clutch design have already been described and they can be gathered into two groups: with multidisc geometry [78], [64], [79] or drum-type geometry [80], [23]. The response time of these devices (i.e. the time to reach the steady torque) is about 10^{-1}s and the torque in some applications goes beyond 10 Nm. MR brakes have also been proposed in [81], [63] and [22]; in those papers the limits of the maximum achievable torques and the problem of frictional heating are discussed.

All the above cited references make use of coils which is definitely

more common than the use of permanent magnets, rarely mentioned in the literature. The use of coils, indeed, makes the actuation and control easier even though fail-safe problems have to be addressed.

In this dissertation a magnetorheological clutch with permanent magnets is presented and discussed. The clutch was envisaged to disengage a power brake vacuum pump, when not needed, from a Diesel engine [8] in order to reduce the fuel emissions. When required, the clutch has to keep engaged, in order to assure a proper operation of the vacuum pump. A simple ON-OFF operation is then required for this application, with no control requirement. It is worth noting that, referring to the usual automotive transmission clutches and brakes, this application requires a very limited torque. Additional requirements for the specific application were the absence of any axial load and a fail-safe operation. The novelty of the proposed device is the actual MR automotive application with strict design torque and volume specifications to be simultaneously satisfied, with the employment of a permanent magnets [82]. Compared to MR clutches with coils, though the maximum torque is not controllable and the response time is longer, it is fail-safe because the magnetic field does not depend on current and does not require energy for actuation. A feasibility study for clutch actuation is also presented in this chapter.

3.3 Clutch design

The design requirements for the clutch are given in Tab. 3.1. The nominal torque (ON condition) necessary to drive the vacuum pump is about 1 Nm. A somewhat higher torque, i.e. 2.5 Nm, may be requested at vehicle start-up, for short times, in case of low temperatures (due to the high viscosity of the lubricant in the vacuum pump, which causes an increase of the absorbed torque); a model for accounting clutch slip during these transients is discussed in Chapter 8 [6]. On the other side, the torque in the disengaged (OFF) condition must be as low as possible, in order to minimize losses. Additional required specifications were the absence of any axial load on the input or output shaft, a fail-safe operation in case of electric failure (e.g. due to exhausted batteries) and strict size constraints, due to the small volume available for the device. For the foreseen application the clutch should be directly coupled with the camshaft, therefore the rotating speed limit in Tab. 3.1 is referred to 6000 rpm of the vehicle engine. The expected operating temperatures

and service life are those typical for automotive components (i.e. −20°C to 100°C and one year maintenance program).

Outer Diameter	<	70 mm
Length	<	50 mm
Nominal operating torque		1 Nm
Maximum engaged Torque		2.5 Nm
Disengaged Torque at 1500 rpm	<	0.5 Nm
Rotational speed	<	3000 rpm

Table 3.1: Design Specifications

MR fluids allow to fulfill the following requirements: short response time, absence of axial loads, temperature resistance and life length. In order to satisfy the torque, size and operating speed requirements, a suitable choice of geometry, materials and fluid gap sizing was undertaken.

3.3.1 Preliminary geometry selection

In the initial design step, in order to define an appropriate clutch geometry, the configurations shown in Fig. 3.6 were examined, having defined a design room, based on the size limits of Tab. 3.1.

In order to estimate the torque capabilities, each configuration was assumed to be made of a combination of single plane or single cylindrical gaps (Fig. 3.5). For the elementary plane gap the yield and viscous torques can be computed as follows:

$$T_Y^p = \int_0^{2\pi} \int_{R_i}^{R_e} \tau_y(H(\theta, r))\, r^2\, d\theta\, dr \tag{3.1}$$

$$T_v^p = \int_0^{2\pi} \int_{R_i}^{R_e} \frac{\eta(\omega^I - \omega^{II})}{s} r^3\, d\theta\, dr \tag{3.2}$$

where the geometrical parameters are defined in Fig. 3.5 and ω^I and ω^{II} are the angular speeds of the primary and secondary shaft respectively. On the other hand, the following expressions hold for the elementary cylindrical gap:

$$T_Y^c = \int_0^{2\pi} \int_0^{L} \tau_y(H(\theta, l))\, R_m^2\, d\theta\, dl \tag{3.3}$$

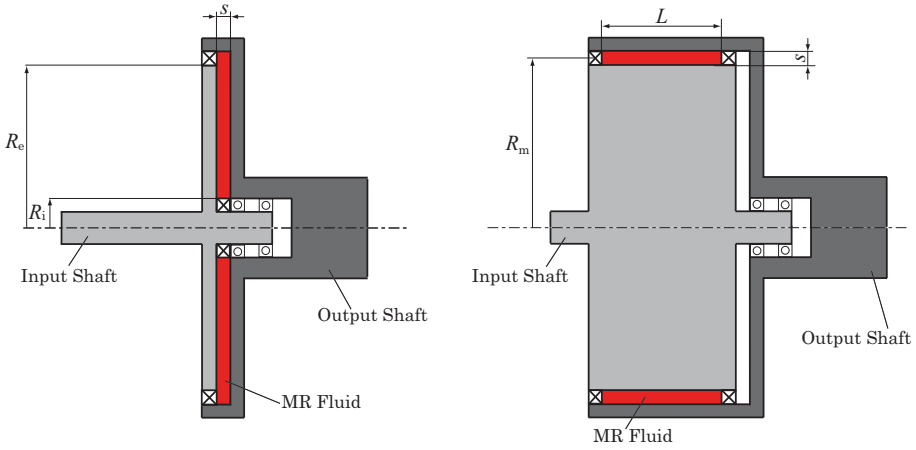

Figure 3.5: Plane and cylindrical geometry

$$T_v^c = \int_0^{2\pi} \int_0^L \frac{\eta(\omega^I - \omega^{II})}{R_e - R_i} R_m^3 \, d\theta \, dl \tag{3.4}$$

The magnetic field distribution, necessary for evaluating the yield stress $\tau_y(H(\theta, r))$ to be used in (3.1) and (3.3), was obtained by means of 2D axisymmetric finite element (FE) simulations, carried out with a numerical magnetic code [83] by the electric team involved in the project [3], together with the constitutive property of the employed MR fluid (Lord Corporation MRF140CG) which was taken from manufacturer data sheet. The fluid was chosen due to the high value of shear yield stress in the magnetized condition.

With reference to the multi-disc scheme (Fig. 3.6(a)) with coils, the torque is transmitted by five thin discs. The coils were assumed to be placed along an external ring and subjected to the maximum endurable direct current. Magnetic FE simulations showed that the magnetic flux density along the fluid was almost constant but very low (<0.1 T see Fig. 3.7), due to the small cross sectional area of the coils and to the long path through the MR fluid, whose permeability is low. Then, this solution appeared not to be a valid one; moreover, with this scheme the viscous torque absorbed by the unmagnetized fluid is significant, due to the high number of disc surfaces and the fail-safe operation cannot be obtained.

The alternative multi-disc configuration, in which the magnetic field

is provided by an internal permanent magnet is presented in Fig. 3.6(b). In this case, due to the fact that the discs extend to the maximum clutch

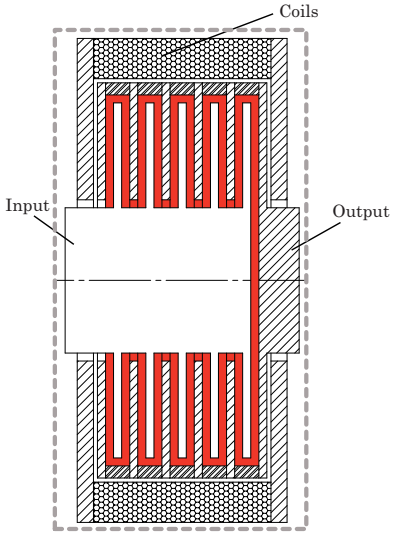

(a) Multi-disc with coils

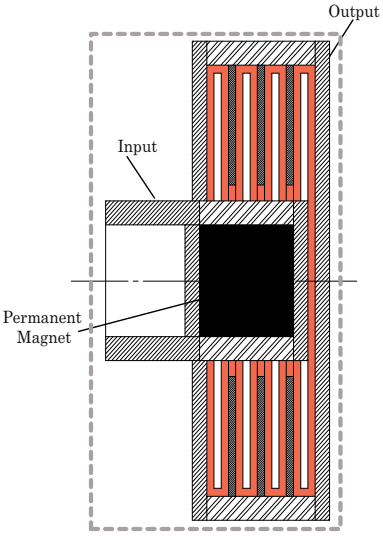

(b) Multi-disc with PM

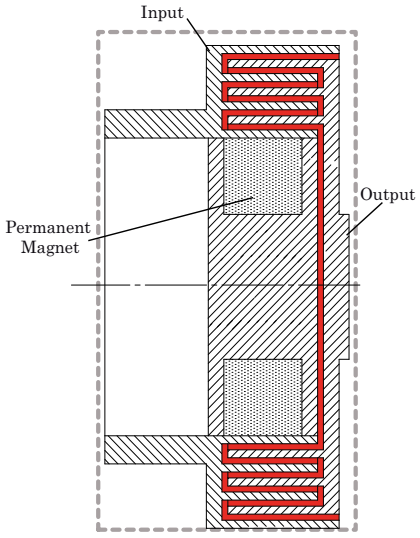

(c) Multi-cylinder with PM

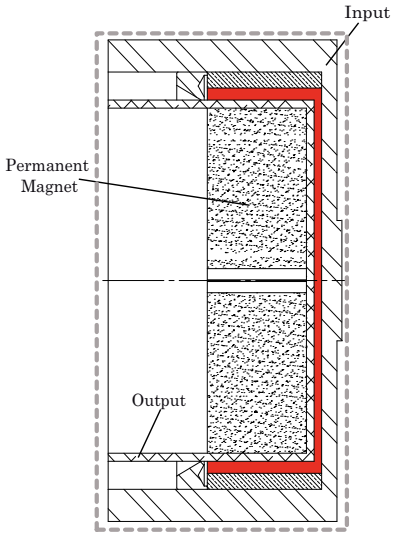

(d) Hybrid (disc-cylinder) geometry with PM

Figure 3.6: Analyzed clutch geometries

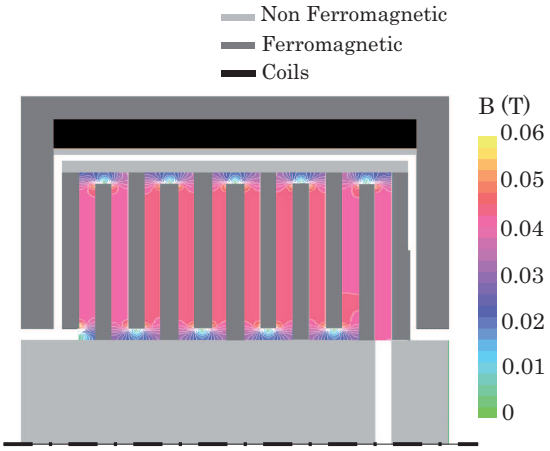

Figure 3.7: Multi-disc with coils

diameter, a considerable increase of the magnetic field in the fluid can be achieved (Fig. 3.8). In this solution the magnet should be moved axially to obtain the engaged/disengaged operation and, therefore, only half of the total volume could be dedicated to the discs. As a consequence, the total path of the magnetic field is shorter and the magnetic field intensity through the fluid results higher with respect to the previous solution, even if the fluid still appeared to be far from saturation. In this case, the viscous torque is higher than that of the previous solution because of the larger average diameter of the fluid gap.

In the multi-cylindrical geometry shown in Fig. 3.6(c), a permanent magnet with radial magnetization, which can be moved axially, was considered. Also in this case only half of the total volume can be used for the cylinders. Magnetic simulations revealed that only the first cylindrical gap, the one closer to the magnet, was sufficiently magnetized, whereas the external ones were only marginally affected by the magnetic field (Fig. 3.9). The result is that the yield torque is rather low, while, as in the previous case, the viscous torque is relatively high.

With reference to the examined solutions, Tab. 3.2 summarizes the yield and viscous (computed for an angular speed difference of 1500rpm) torques, obtained by Eq. 3.1-3.4. From the preliminary analysis the following conclusion can be drawn:

- the coils can not be used since the magnetic flux density is low, due

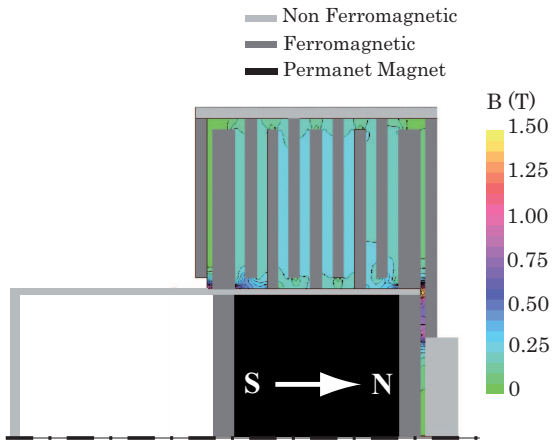

Figure 3.8: Multi-disc with permanent magnet

to the small available room, and for the fail-safe requirements;

- the multi-disc geometry creates a path too long for the magnetic field, which leads to a low average magnetization of the fluid, and to a relatively high viscous torque;
- the multi-cylindrical geometry appears unsuitable because the magnetic field affects only the first (i.e. the most internal) fluid gap, whereas all the gaps contribute to the viscous torque.

This analysis allowed to develop the device schematically represented in Fig. 3.6(d), which is composed of a cylindrical and a plane gap and has a torque capability which proved to be greater than that of the other analyzed schemes (see Tab. 3.2). In particular, the advantages of this solution are given by the large size of the permanent magnet which is able to provide a high magnetic flux density in the cylindrical gap and in the large diameter of the cylindrical gap, which means a higher moment arm of the tangential forces and therefore a higher torque. The plane gap is not strongly magnetized but it also contributes to torque transmission. The viscous torque is lower than that obtained for the solutions (a), (b) and (c), due to the reduced total area of the facing surfaces.

From a magnetic point of view, the ferromagnetic and non-ferromagnetic materials distribution around the fluid was deeply investigated in order to confine the magnetic field within the regions of interest, trying to

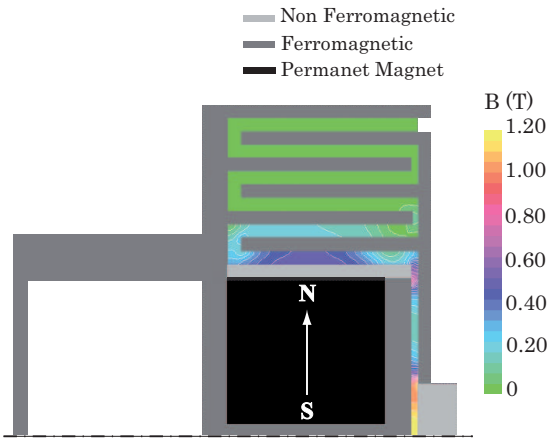

Figure 3.9: Multi-cylinder with permanent magnet

	Solution (a)	Solution (b)	Solution (c)	Solution (d)
T_y (Nm)	0.5	2.3	0.6	3.03
T_v (Nm)	0.15	0.30	0.30	0.10

Table 3.2: Calculated yield and viscous torque

maximize the mechanical torque. The MRF gap geometry, the permanent magnets configuration as well as the materials selection were obtained at the end of an iterative procedure based on several FE analyses.

During this phase the 3-D magnetostatic FE model shown in Fig. 3.10 was employed, which, considering the problem symmetries, represents only one quarter of the whole structure. The FE model is made up of about 1×10^6 elements and takes about 40 minutes of CPU time on a Linux machine with 24 GB of RAM.

The numerical simulations allowed also to design the excitation system, which is based on a rare-earth NdFeB hollow cylinder. The poles number and the magnetization type were chosen in order to maximize the torque within the given geometry, also taking into account the feasibility of the magnetic configuration with respect to the device dimensions and the reduction of the axial magnetic force. Figure 3.11 shows the radial and diametral magnetization for a four-pole magnet, while Fig. 3.12 shows

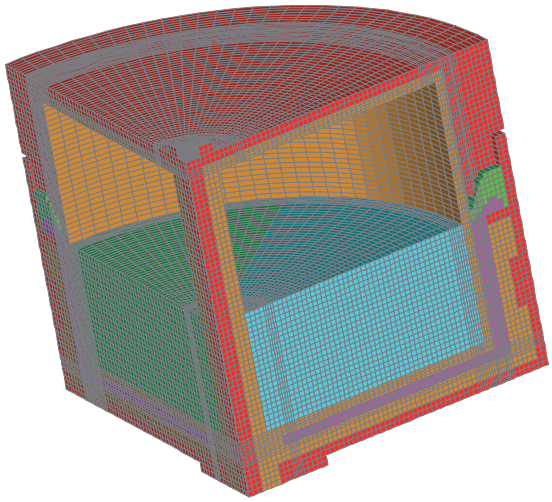

Figure 3.10: Hybrid geometry with PM; 3D model.

the magnetic flux density B in the MRF, for different numbers of poles p (from 2 to 8) and for different kinds of magnetization (radial or diametral). The results showed that the highest MRF excitation level was obtained by using a PM system composed of four 90°–poles, alternately magnetized along their diameter direction, whose characteristics and dimensions are reported in Tab. 3.3.

Table 3.3: Characteristics of the PM

Material	Physical Characteristics	Dimensions
NdFeB	$B_r = 1.36$ T	$D_e = 52.8$ mm
	$H_c = 10.2 \times 10^5$ A/m	$d_i = 6.2$ mm
	$T_{max} = 150^o$ C	l = 12 mm

Finally, Fig. 3.13 shows the map of the magnetic flux density B in the MRF in the disengaged (left) and engaged (right) configurations. As can be observed, when the PM is in the engaged state, the magnetic flux density is high enough to give in a high level of transmissible torque. On the contrary, the disengaged state is characterized by very low magnetic flux density.

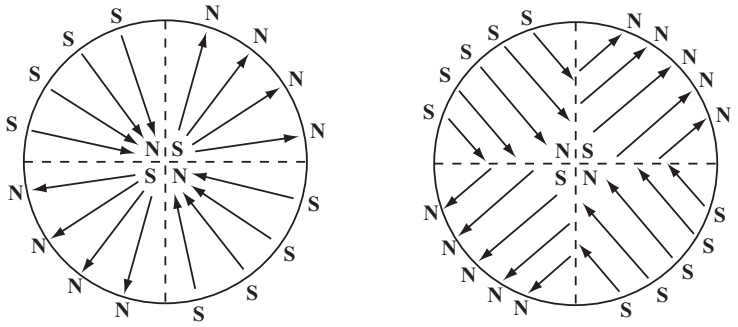

Figure 3.11: Radial (left) and diametral (right) magnetization for a 4 poles PM system

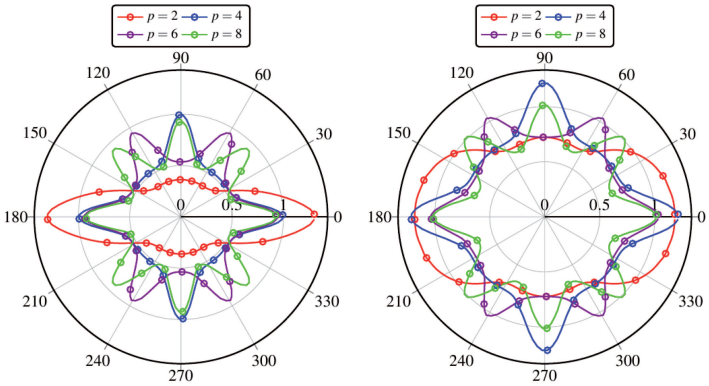

Figure 3.12: Magnetic flux density (T) in the MRF as a function of the number of poles of the PM system. Radial magnetization (left); diametral magnetization (right)

3.3.2 Prototype description

The developed prototype is depicted in Fig. 3.14 and Fig. 3.15. The primary and secondary shafts are indicated as element no.1 and no.2 respectively. The MR fluid film is represented in red. The gap is filled

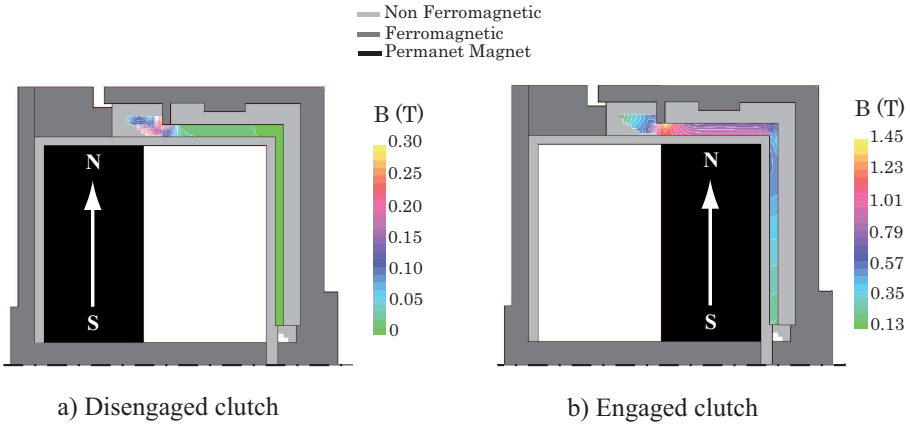

Figure 3.13: Magnetic field distribution in the engaged and disengaged configurations

by removing the screws (no.3) and is contained by the seals (no.4 and 5). The magnetic field is generated by the magnets (no.6) which can slide axially. The two main parts that form the clutch are aligned by the bearings (no.9); in particular, the primary shaft is centred with respect to the shell housing the magnets (no.10), whereas, the secondary shaft is centred with respect to the crown, by three dowel pins; the Seeger ring (no.11) fixes the relative axial position of the two halves and consequently the thickness of the plane gap. The external diameter and length of the prototype are 65 mm and 40 mm, respectively (see Fig. 3.15), while the diameter of the input and output shaft is 15 mm. The MRF gap has an average diameter of the cylindrical part of 57 mm, while its thickness is 1.5 mm and 1 mm in the cylindrical and plane portion, respectively.

The operating principle of the prototype is represented schematically in Fig. 3.16; when the magnets are moved towards the MR fluid gap (Fig. 3.16a), the fluid is excited and the clutch is engaged; when the magnets are moved to the opposite side (Fig. 3.16b) the fluid behaves like a Newtonian fluid and the clutch is disengaged. The first prototype was built without providing any actuation for the magnets axial motion as its main purpose was to measure the transmissible torque in various conditions and validate the models. The magnets actuation will instead be discussed in the next section.

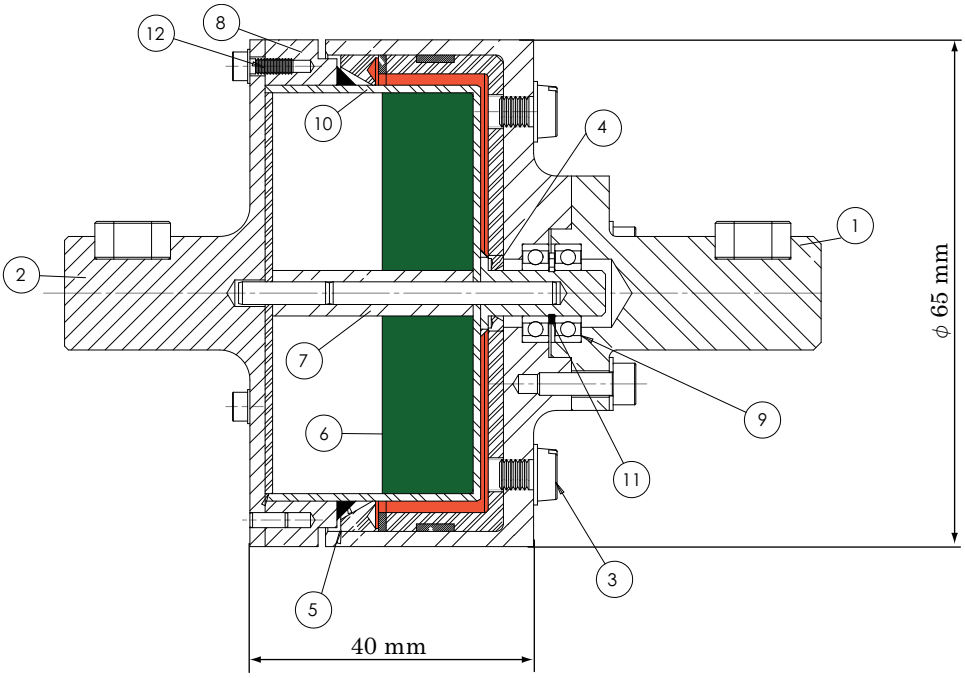

Figure 3.14: Designed prototype scheme

3.4 Clutch actuation

A feasibility analysis for the clutch actuation was carried out with a simple model, even if the actuation system was not included in the first prototype. In order to ensure a fail-safe operation, the PM should be normally positioned so that the clutch is in the engaged configuration. Then, in order to disengage the clutch, a driving force must be supplied to overcome the magnetic force, the friction force and any other counteracting force in the axial direction. Pneumatic actuation was recognized as the most suitable for the specific application (an electrical actuation was also considered), thanks to the availability of the vacuum pump [84]. To this aim, the chamber containing the PM is separated in two rooms by means of a pneumatic seal attached to the PM, which can slide with low friction along the ON–OFF path. One of the chambers (the one on the right side) is connected to the atmospheric pressure p_1, whereas in the other one (on the left side), the pressure $\bar{p}_0$ is determined by the vacuum pump. In

this way, the resultant of the pressure forces can be used to move the PM from the ON to the OFF state when a sufficient level of vacuum is reached. A proper coil spring has to be employed, instead, to guarantee a fail safe operation, when both chambers are in communication with the atmospheric pressure.

With reference to Fig. 3.17 the following equation of motion holds for the magnet:

$$F_S(\delta) + F_M(\delta) + \bar{p}_0(\delta)\pi\frac{D^2}{4} - \bar{p}_1(\delta)\pi\frac{D^2}{4} - F_F = m_M\ddot{\delta} \tag{3.5}$$

where F_S, F_M and F_F are the spring force, the magnetic force and the friction force, $\bar{p}_0$ and $\bar{p}_1$ are the pressures inside the left and right chambers, δ identifies the position of the magnet and m_M is the mass of the magnet. The magnetic force F_M was computed by means of FEM analysis [3] as a function of the magnets position (see Fig. 3.18), while an estimate of the friction force (about 5N) was obtained on the basis of the seals data sheet.

Equation 3.5 was numerically solved considering a constant time step

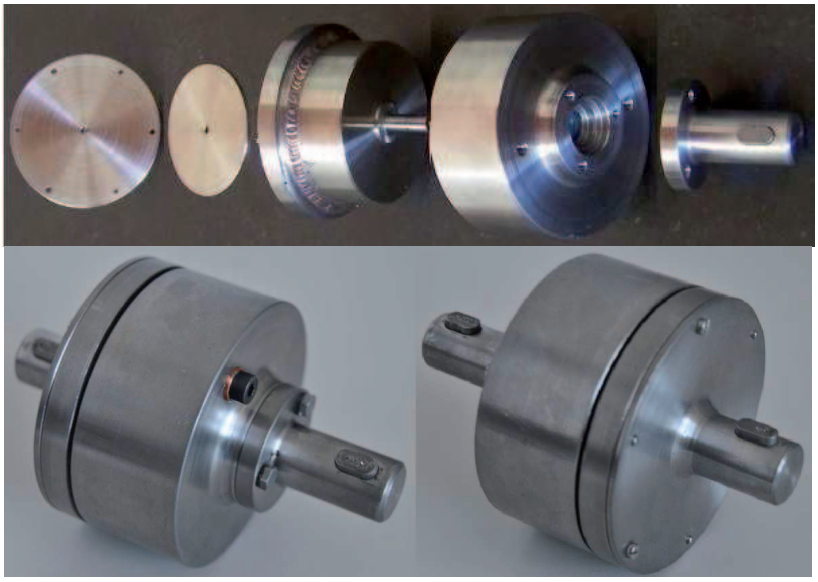

Figure 3.15: Pictures of the clutch prototype

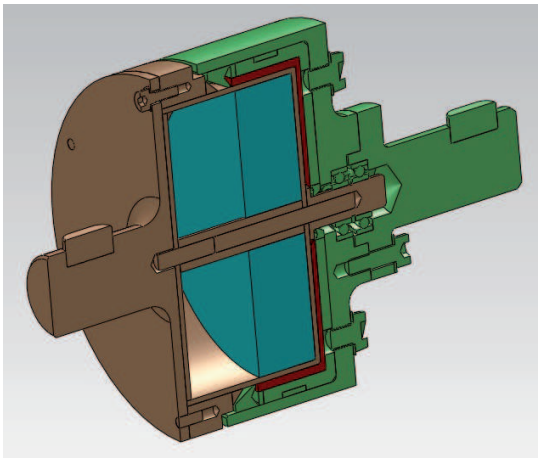

(a) Clutch in the engaged configuration

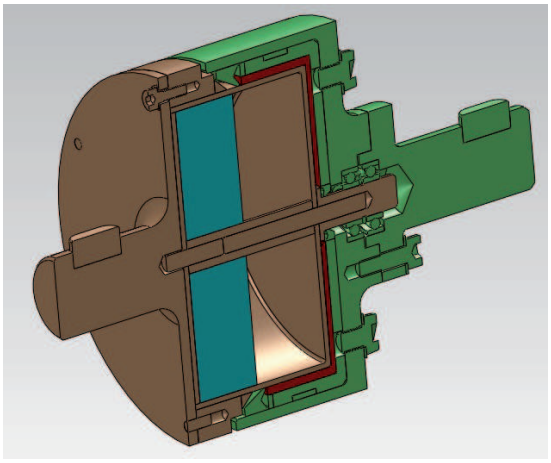

(b) Clutch in the disengaged configuration

Figure 3.16: Clutch operating principle

($\Delta t = 0.1$ ms). The pressure values inside both chambers ($\bar{p}_0$ and $\bar{p}_1$) were calculated at each time-step using a simple model, based on lumped efflux coefficients, which are given for any value of the diameter of the orifices that are necessary on the primary and secondary shaft (see Fig. 3.17).

Let $(i-1)$ and (i) be two consecutive time-steps. The density $\rho_0^{(i-1)}$

of air in the left room is obtained by the following relationship:

$$\rho_0^{(i-1)} = \frac{m_0^{(i-1)}}{V_0^{(i-1)}} \tag{3.6}$$

where the mass $m_0^{(i-1)}$ and the volume $V_0^{(i-1)}$ are known from the previous time-step. Consequently, the pressure $\bar{p}_0^{(i-1)}$ is determined, by assuming an adiabatic transformation, according to:

$$\bar{p}_0^{(i-1)} = \left(\frac{\rho^{(i-1)}}{\rho^{(i-2)}} \right)^k \bar{p}_0^{(i-2)} \tag{3.7}$$

The mass of air at the next time-step (i) is then obtained by the following relationship

$$m_0^{(i)} = m_0^{(i-1)} + \Delta m_0^{(i)} \tag{3.8}$$

where, $\Delta m_0^{(i)}$ is evaluated considering the Saint-Venant–Wantzel law on incompressible flow through an orifice

$$\Delta m_0^{(i)} = \dot{m}_0(A_H, \rho_0^{(i-1)}, p_0, \bar{p}_0^{(i-1)})\, \Delta t \tag{3.9}$$

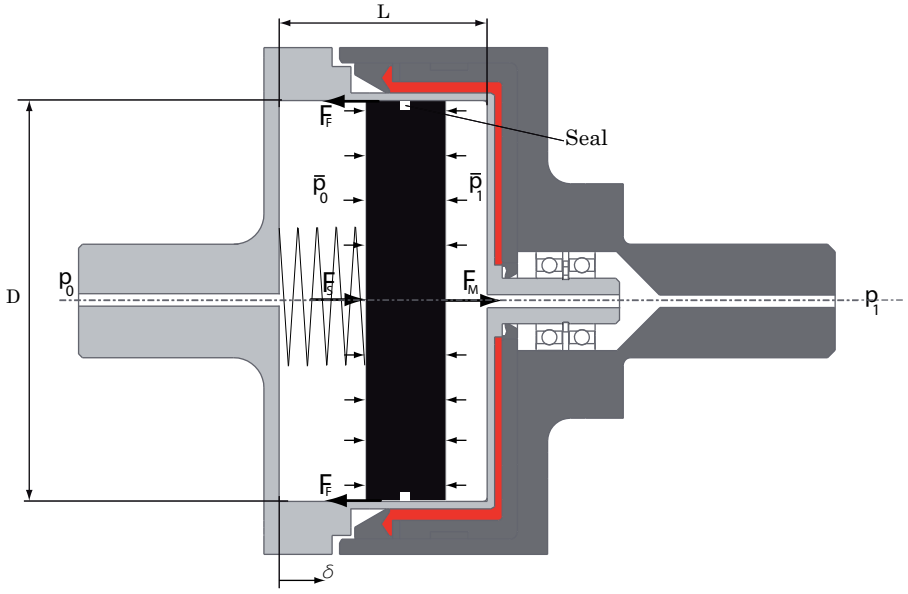

Figure 3.17: Magnet Movement

where A_H is the cross section area of the hole in the left shaft and p_0 the pressure upstream. At the same time, the volume of the room at time-step (i) is obtained by the displacement of the magnets δ, which is computed by integrating Eq. 3.5 at time-step (i)

$$V_0^{(i)} = V_0^{(i-1)} + \Delta V_0^{(i)} = V_0^{(i-1)} + \pi \frac{D^2}{4} \left(\delta^{(i)} - \delta^{(i-1)} \right). \tag{3.10}$$

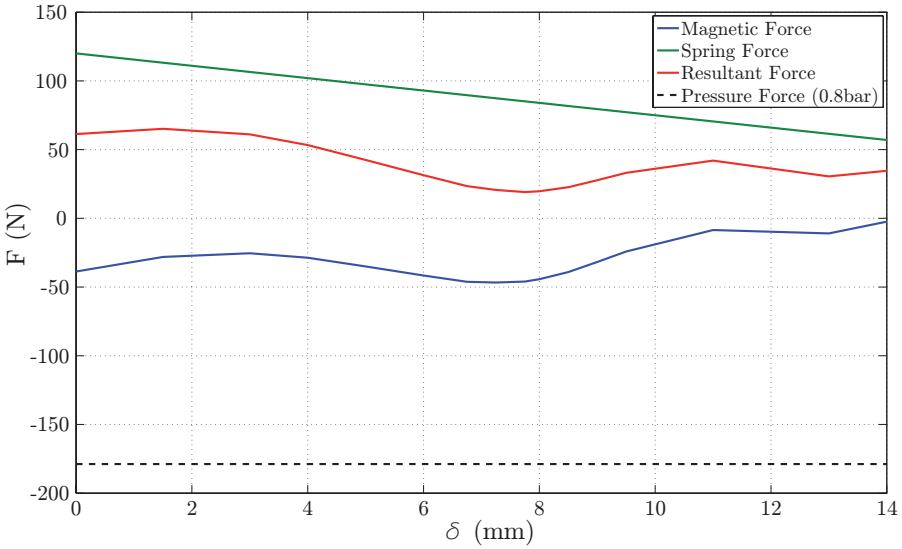

Figure 3.18: Forces acting on the magnet

Then, the density and pressure in the left chamber are updated by Eq. 3.6 and Eq. 3.7 and the process iterated. The pressure $\bar{p}_1^{(i)}$ inside the right room, which is necessary to obtain the pressure resultant force acting on the magnets in the axial direction, is determined by the same procedure.

A spring stiffness and pre-load were then determined by some analyses in which the numerical procedure was employed. The final spring force is shown in Fig. 3.18 together with the magnetic force. It can be observed how the magnetic force results always negative (directed leftward in Fig. 3.17) and lower than the spring force. The magnet and spring resultant force is positive if no pressure force is applied, so in this configuration the steady equilibrium of the magnet is in the engaged

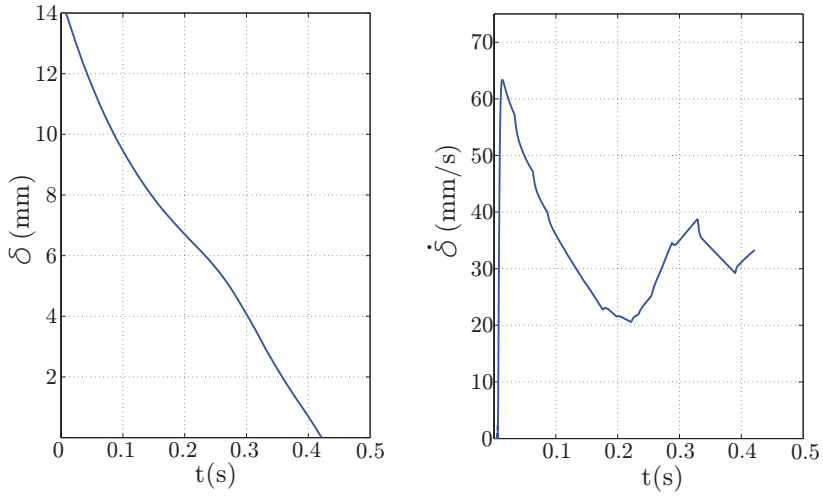

Figure 3.19: Magnet displacement and speed profiles - Engagement phase

condition. On the contrary, if the difference of pressure is exerted, also the pneumatic steady force has to be considered and, in this condition, the magnet is in the steady equilibrium in the disengaged condition.

The transient from the disengaged to the engaged configuration was also analysed. For the transient analysis, an initial condition with pressure values of $p_0 = 0.2$ bar and $p_1 = 1$ bar was considered; then, an instantaneous step of pressure in the left chamber from 0 to 1 bar was imposed. The so obtained displacement and speed profiles ($\delta(t)$ and $\dot{\delta}(t)$) of the magnets are shown in Fig. 3.19.

As it can be seen, the transient takes few tenths of a second and the speed of the magnets approaching the end of the engaged chamber is about 0.03 m/s. In conclusion, both results in terms of engagement time and impact velocity can be considered satisfactory even though an experimental validation, employing the real system, is necessary to obtain additional insights for a optimal definition of the actuation device.

Chapter 4

Test bench and preliminary characterization of the MR clutch

Once the first clutch prototype was designed, an experimental bench was set-up to test the clutch performances. The aim of the bench was to measure the torque transmitted by the magnetorheological clutch in several working conditions and to verify the accuracy of the models used during the design phase, by comparing the results of the simulations and of the experimental tests.

Several experimental setups developed for testing MR devices can be found in the technical literature. In [22] a multiphysics design optimization of a magnetorheological brake is proposed and a prototype was built and tested. Results show viscous torque with unmagnetized fluid and total torque in presence of a magnetic field generated by coils. Experimental data are compared with simulated ones; the measured torque is smaller than that obtained by simulation, due to the lack of information on material properties and to thermal effects. In [63] a disc-type clutch was designed and tested and torque versus speed diagrams were obtained. Steady state experiments were performed and the transmitted torque was measured at different speeds. A linear relationship between torque and rotational speed was observed, in the test conditions, which include a medium magnetization (0.4 T) and low shear rates (up to 100s). In [62] a torque control clutch was tested and then in [24, 79] a novel slip control differential was tested, taking into account also time response

delay. Very high torque were reached (up to 250 Nm) but no information on dimensions nor magnetization are given. A different approach was used in [85], where a mathematical model is proposed to consider the shear thinning effect produced by fluids subject to high shear rates in drum type clutches. More than on the transmitted torque, the attention is focused mainly on a mechanical model used to analyse the velocity profile in the fluid, according either to the Bingham-plastic or the Herschel-Bulkley model. Results show substantial differences, depending on the considered model, either at very high shear rate ($\dot{\gamma} > 2000$s) or in estimating the yield stress ($\dot{\gamma} \to 0$).

In [50] a model to predict the dependence of the parameters considered in BP and HB models with magnetization is proposed. In [20] this model was employed to predict the torque value in a magnetorheological brake. Several commercial fluids were tested and fitting methods were employed to obtain the model parameters, which were used to predict the brake torque. Using the HB model, interesting differences on the fluid properties were obtained, which highlight the importance of the gap dimension in the fluid choice. In [86] the parameters of the BP e HB models were obtained either through a fitting technique or identified using genetic algorithms.

In this chapter the experimental equipment set up to test the first prototype of the clutch and to measure the torque transmitted, at different speeds, as a function of the relative velocities of its two shafts is described. In addition, an analysis of the results using the Bingham-plastic and Herschel-Bulkeley model is proposed.

4.1 Testing equipment

A test bench was developed in order to obtain the torque transmitted by the clutch, considering different working conditions and braking torque profiles. This was achieved by a control and measurement system consisting in a PC endowed with a *National Instruments* DAQ and a specifically developed *NI LabView* program.

Figure 4.1 shows the set-up equipment. The primary and secondary shafts (element no. 1-2 in Fig. 4.1 respectively) are connected to the clutch (element no. 10 - Fig. 4.1) and are supported by three bearing units, one of which is fixed on an elastic mat to avoid overconstraining. Both shafts are connected to electric motors by two orientable joints (elements no. 5,

Fig. 4.1). An asynchronous motor controlled by an inverter (element no. 3, Fig. 4.1) drives the primary shaft, while a brushless motor controlled by a servo drives system (element no. 4, Fig. 4.1) brakes the secondary shaft. The rotational speed of the primary group is measured by means of a digital encoder (element no. 8, Fig. 4.1), whereas the rotational speed of the secondary group is measured by an encoder embedded into the brushless motor. The torque transmitted by the clutch and acting on the secondary shaft is measured by means of a torque-meter (element no. 9, Fig. 4.1).

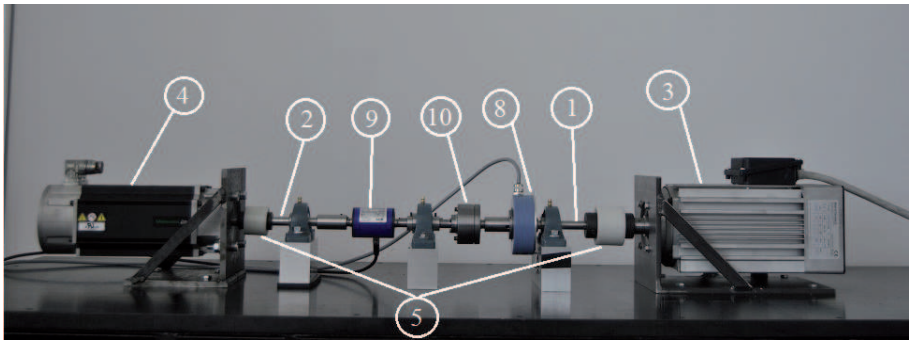

Figure 4.1: Testing equipment

The control scheme for experimental tests is described in Fig. 4.2. The sample time was set to 50 ms. The user can define a desired speed profile ω_T^I of the primary group. This is driven by an asynchronous motor regulated by an inverter employing a traditional V/f control, so that the reference frequency signal is computed by Eq. (4.1), taking into account the synchronous rotational speed of the motor ω_S^I

The rotational speed of the primary group ω^I is acquired by the encoder and compared with the target speed ω_T^I. The difference between signals is processed by a PID controller to adjust the frequency signal to f_0.

The secondary group is braked by the brushless motor. The user directly defines the desired torque (T_T) to be submitted to the controller. The torque (T) measured by the torque-meter corresponds to the torque acting on the secondary shaft which, neglecting dynamic effects, can be assumed equal to the torque transmitted by the clutch. The measured rotational speed of the secondary group (ω^{II}) is used to evaluate the rota-

tional speed difference ($\Delta\omega$) between the primary and secondary groups. Transmitted torque and the rotational speeds can also be monitored in real-time during tests.

$$f_s^I = \frac{\omega_s^I \, p}{60} \tag{4.1}$$

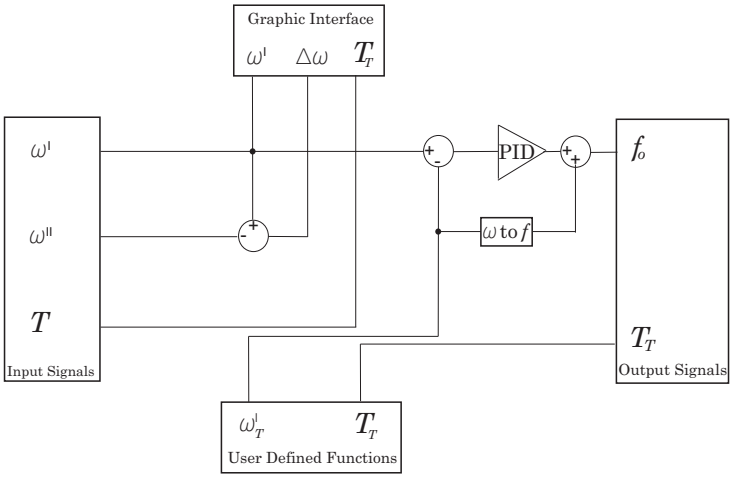

Figure 4.2: Control diagram

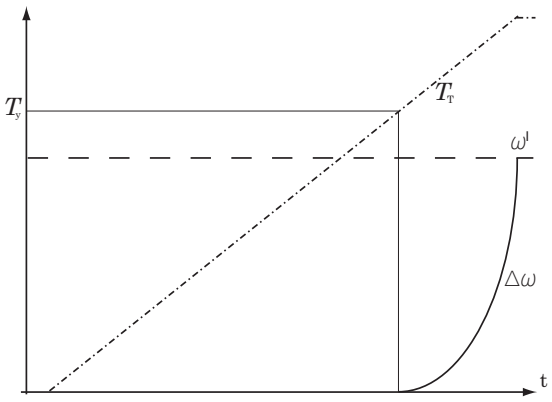

Figure 4.3: Testing procedure

4.2 Testing procedure

An experimental campaign was planned in order to analyse the torque transmitted by the clutch at several primary rotational speeds and several relative speeds. As far as the engaged clutch (ON condition) is concerned, the reference testing procedure is represented in Fig. 4.3.

The rotational speed of the primary group is imposed by the user and it is kept constant by a PID controller. In the meantime an opposing torque ramp is imposed to the brushless motor, in order to brake the system. The primary and secondary shaft keep synchronous ($\Delta\omega = 0$) until a yield torque (T_y) is reached. Afterwards, slip between the two shafts begins, while the torque is still rising. The test is completed once the secondary group of the clutch comes to a stop ($\Delta\omega = \omega^I$). To avoid any dynamic effect, the torque was applied at a low rate (0.05 $\mathrm{N\,m\,s^{-1}}$). The data acquired by the torque meter were filtered by a sixth order low pass filter to remove signal noise. As far as the disengaged clutch (OFF condition) is concerned, tests were performed imposing a low rate of rotational speed to the primary group, while keeping the secondary one fixed. The torque measured by the torque meter and the corresponding primary rotational speed were recorded.

4.3 Results

Tests involved two configurations with the disengaged clutch, i.e. with the permanent magnet located in the shielded position (OFF condition) and outside the clutch (OUT condition, aimed at estimating the torque due to non perfect shielding of the magnetic field) and one configuration with the clutch engaged, with the magnet located close to the fluid (ON condition).

4.3.1 Disengaged clutch

Some preliminary tests were aimed at measuring the friction torque due to seals and bearings and the amount of viscous torque, by applying an increasing angular speed to the primary group and keeping the secondary one stopped.

The amount of viscous torque was computed considering the geometry of the clutch and an ideal Newtonian behavior of the unmagnetized fluid. In Eq. 4.2 the contribution of viscous torque is obtained by the sum of a

first contribution due to the effect of the fluid in the drum-like gap and of a second contribution related to the planar gap.

$$T_V = \int_{Drum} \tau_v R_m^2 \, d\theta \, dl + \int_{Plane} \tau_v r^2 \, d\theta \, dr \tag{4.2}$$

The viscous shear stress τ_v can be expressed, assuming a Couette flow, as a function of viscosity (η) and shear rate ($\dot{\gamma}$). The latter is related to the angular speed difference ($\Delta\omega$) and to the clutch geometry, i.e. local gap thickness s and radius r, as shown in Eq. 4.3.

$$\tau_v = \eta\dot{\gamma} = \eta\frac{\Delta\omega r}{s} \tag{4.3}$$

By using Eq. 4.2 and Eq. 4.3 the viscous torque of the proposed prototype is obtained, Eq. 4.4

$$T_V = \pi\eta\Delta\omega\left(\frac{2R_m^3 L}{s_d} + \frac{R_e^4 - R_i^4}{2s_p}\right) \tag{4.4}$$

where s_p and s_d are respectively the thickness of the plane and drum gaps, R_i and R_e are the disc inner and outer radii, whereas R_m and L are the drum gap mean radius and length.

Figure 4.4 shows the experimental results obtained with the disengaged configuration, in relation to both the clutch without the magnet (OUT condition) and the clutch with the magnet located in the shielded position (OFF working condition). Considering the OUT condition, the yield torque value, corresponding to the stick-slip transition, can be totally ascribed to Coulomb friction between the seals and the rotating part of the clutch, whereas in the OFF condition residual magnetization is also present.

Once the clutch slip occurs, a linear relationship between torque (T) and relative angular speed ($\Delta\omega$) is observed. The yield torque T_y and the slope m of the $T(\Delta\omega)$ line were found, by means of the least square fitting method, Tab. 4.1

A global viscosity index $\widetilde{\eta}$ of the clutch can be computed, knowing the geometry of the clutch and considering Eq. 4.4, as shown in Eq. 4.5

$$\widetilde{\eta} = \frac{T_V - T_y}{K_g \, \Delta\omega} \tag{4.5}$$

where K_g collects the geometric parameters of the clutch.

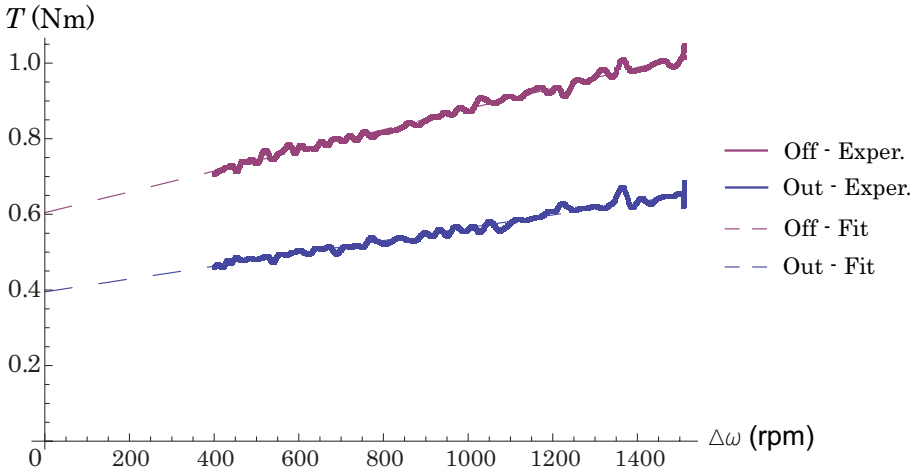

Figure 4.4: Out and Off torque

Table 4.1: Out and Off torque

Condition	T_y (N m)	m (N mrpm)	$\widetilde{\eta}$ (Pa s)
OUT	0.60	0.00027	0.49
OFF	0.39	0.00017	0.79

This index can be assumed as a valid estimation of the fluid viscosity, especially in the OUT working condition. The $\widetilde{\eta}$ index obtained in this condition can be compared with the viscosity of the fluid. The value obtained by experimental test appeared slightly higher than the value declared by the supplier, that is 0.28 ± 0.07 Pa s.

Concerning the OFF condition a higher value of $\widetilde{\eta}$ is found, which can be hardly ascribed to the enhanced fluid viscosity due to residual magnetization, but can be likely imputed to the small leakage of the larger seal, which creates a very small additional fluid gap, under the effect of the magnetic field.

4.3.2 Engaged clutch

Once the clutch was tested in the disengaged mode, a detailed test campaign in the engaged mode (ON condition) was performed. In this case, as described in Fig. 4.3, the transmitted torque was measured imposing several rotational speeds to the primary group and imposing an increasing braking torque to the secondary one. Figure 4.5 shows a typical diagram of the measured torque as a function of relative angular velocity.

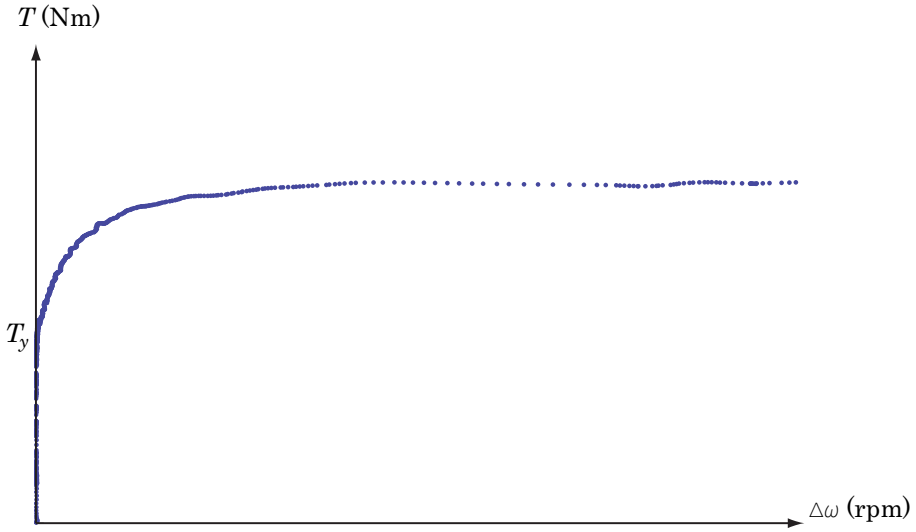

Figure 4.5: Torque in the engaged configuration

It is possible to observe a synchronous motion of the primary and secondary group until a yield torque is reached (T_y). Then the torque increases further up to a limit value. Experimental results revealed no correlations between the rotational speed imposed to the primary group (ω^I) and the measured torque, so results were processed and analyzed taking into account only the relative speed between the two groups of the clutch.

In order to fit experimental measures, avoiding imbalances caused by the uneven spacing of the acquired raw data, the following numerical procedure was adopted: a piecewise linear interpolation was firstly performed on $T(\Delta\omega)$ raw data, to obtain a continuous function; then, a fixed-step

resampling was made, based on the interpolated function, in order to obtain an ordered discrete list of $T(\Delta\omega)$. The friction contribution was removed from data values, as shown in Eq. 4.6

$$\widetilde{T} = T(\Delta\omega) - T_y^{OUT} \tag{4.6}$$

Four different primary speeds were imposed: 500rpm, 800rpm, 1000rpm, 1500rpm. At each speed, the test was repeated three times, obtaining a total of 12 runs. Two fitting functions were considered to obtain an analytical form of the relation between torque and relative speed. Firstly, a Bingham-like model was proposed (Eq. 4.7) to fit experimental data.

$$\widetilde{T} = \widetilde{T}_y^{BP} + \widetilde{\eta}\,\Delta\omega \tag{4.7}$$

A least square fit was performed on the whole data set obtained by the 12 runs, obtaining $\widetilde{T}_y^{BP}$ and $\widetilde{\eta}$.

Then the same group of data was fitted taking into account an Herschel-Bulkley-like (Eq. 4.8) model, applied again to the relation between torque and relative speed

$$\widetilde{T} = \widetilde{T}_y^{HB} + \widetilde{K}\,\Delta\omega^{\widetilde{n}} \tag{4.8}$$

obtaining $\widetilde{T}_y^{HB}$, $\widetilde{K}$ and $\widetilde{n}$ as output values.

Figure 4.6 shows a comparison between the measurements and the best fit interpolations, according to the BP and the HB models applied directly to the transmitted torque.

The BP model appeared less accurate to fit experimental torque data, due to a constant slope and to its intrinsic incapability to represent the observed profile at low speed. Furthermore, if the least square fit is applied to the whole data set, a secant line to the experimental curve is obtained, which overestimates the yield torque and the high speed torque, whereas underestimates the transitional range, as shown in Fig. 4.6. If the fit is applied to the data related to low speed, a right estimation of the yield torque can be found, but an excessive slope is computed (see Fig. 4.7). On the contrary, if only higher speeds are considered, a quasi-horizontal line is found, which strongly overestimates yield stress and does not present appreciable viscosity (see Fig. 4.7).

On the other hand, the HB model appeared to fit better experimental data. In this case the model parameters were obtained as follows. An initial value of the yield torque $\widetilde{T}_{yi}^{HB}$ was firstly estimated, as the torque

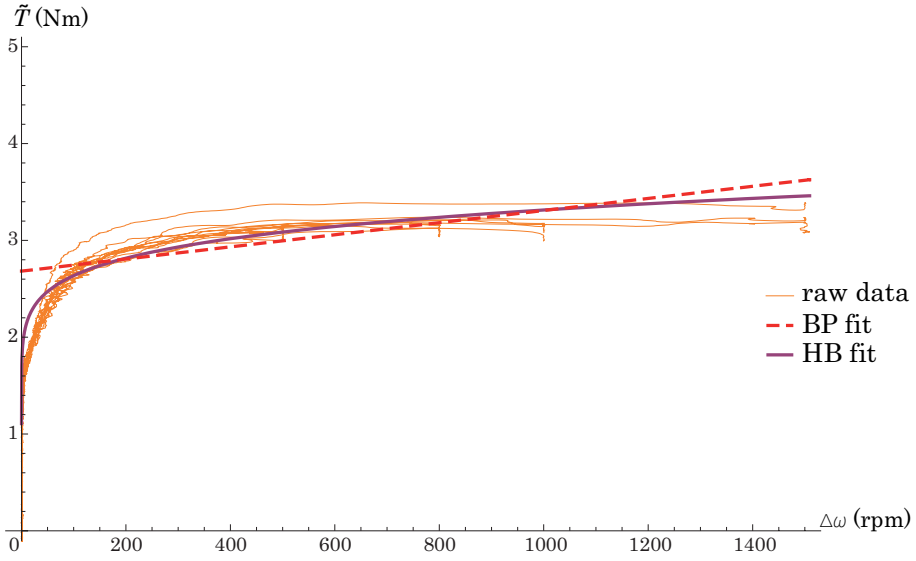

Figure 4.6: Torque in the engaged configuration - Raw and fitted data

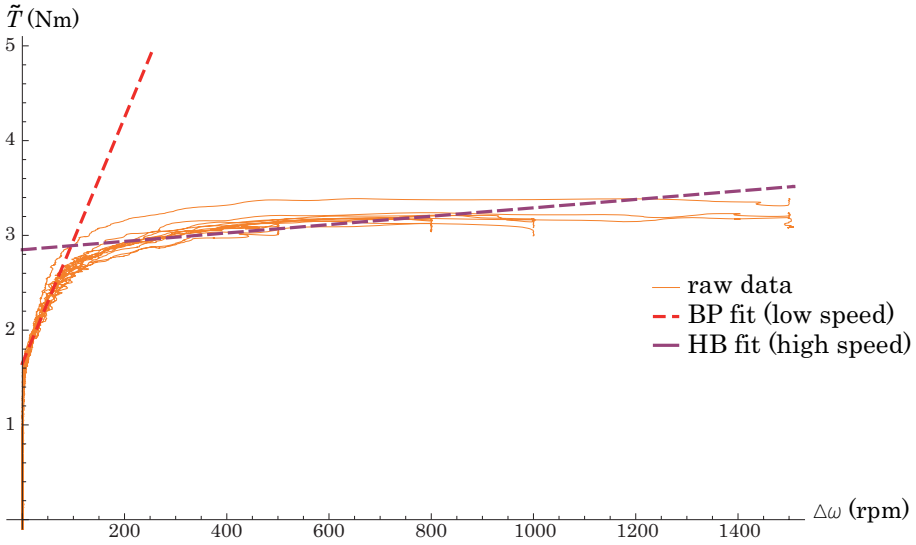

Figure 4.7: BP fitting based on low and high relative speed data

that occurs at a user defined threshold (near zero) of the relative speed; then, the model parameters ($\widetilde{T}_y^{HB}$, $\widetilde{K}$, $\widetilde{n}$) were obtained, considering all the acquired data, by a best fit procedure in which a tolerance around $\widetilde{T}_{yi}^{HB}$ was fixed for $\widetilde{T}_y^{HB}$ and it was required that $0 < n < 1$.

Figure 4.6 shows some differences between the HB fitting and raw data. At low speed the torque is overestimated, whereas at high speed an asymptotic behavior of the curve cannot be achieved due to the HB monotonically increasing function. Also in this case, the fitting could be performed considering alternatively the low or the high speed range, as shown in Fig. 4.8. If the considered data set is related to the low speed range, the fit follows closely the rigid-perfectly plastic transitional phase, whereas it strongly overestimates the torque in the high speed range. In the other case, the fitting function is smooth, but the torque is strongly overestimated at low speed.

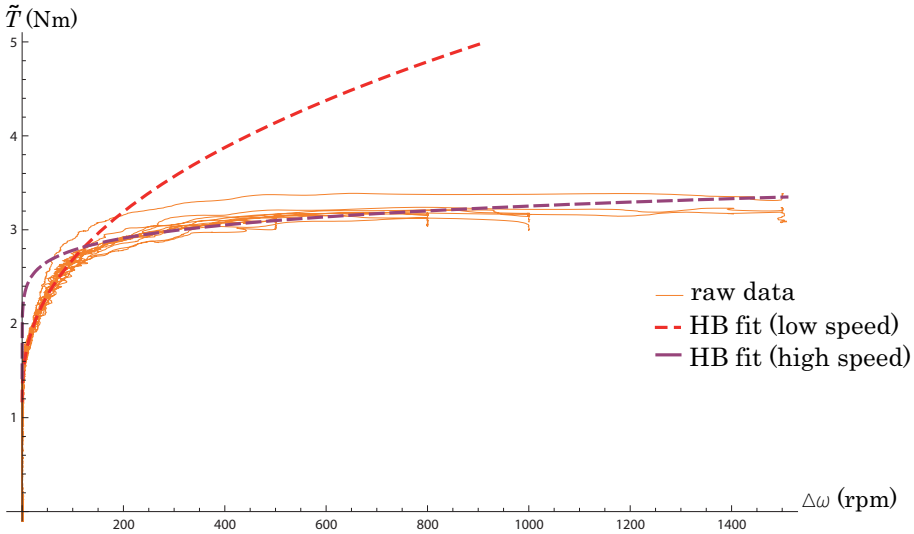

Figure 4.8: HB fitting based on low and high relative speed data

The BP and HB models were also more properly used to infer the behavior of the fluid on the basis of acquired data. In the same way as explained in Eq. 4.2 for the disengaged clutch, the torque $\overline{T}$ for the engaged clutch was calculated according to Eq. 4.9

$$\overline{T} = \int_{Drum} \tau \, R_m^2 \, d\theta \, dl + \int_{Plane} \tau \, r^2 \, d\theta \, dr \tag{4.9}$$

If the constitutive BP model is considered to describe the shear stress,

$$\tau_y = \tau_y^{BP} + \eta \frac{\Delta\omega \, r}{s} \tag{4.10}$$

then Eq. 4.9 is equivalent to Eq. 4.11.

$$\overline{T} = 2\pi \left(\left(\frac{R_e^3 - R_i^3}{3} + L \, R_m^2 \right) \tau_y^{BP} + \left(\frac{R_e^4 - R_i^4}{4 \, s_p} + \frac{L \, R_m^3}{s_d} \right) \eta \, \Delta\omega \right) \tag{4.11}$$

On the other hand, if HB model is considered, the constitutive relation is described in Eq. 4.12

$$\tau_y = \tau_y^{HB} + K \left(\frac{\Delta\omega \, r}{s} \right)^n \tag{4.12}$$

and the transmitted torque can be computed as described in Eq. 4.13.

$$\overline{T} = 2\pi \left(\left(\frac{R_e^3 - R_i^3}{3} + L \, R_m^2 \right) \tau_y^{HB} + \left(\frac{R_e^{n+3} - R_i^{n+3}}{(n+3) s_p^n} + \frac{L \, R_m^{n+2}}{s_d^n} \right) K \, \Delta\omega^n \right) \tag{4.13}$$

By using Eq. 4.11 and Eq. 4.13, a least square fit can be applied to experimental data to obtain the constitutive parameters of the fluid. However, it is worth noting that the so computed parameters are strictly related to the device and do not represent the actual fluid parameters, because the magnetic field through the fluid is not uniform and its value and orientation are neither exactly known nor directly measurable. Figure 4.9, to be compared with Fig. 4.6, shows the transmitted torque obtained considering BP and HB models applied directly to the fluid. Even though the ways to compute the fitted torque were different, no perceptible difference can be found between torque functions obtained by applying BP and HB models either to the torque ($\overline{T}$) or to the shear stress (τ). So the models confirm the previously described limitations.

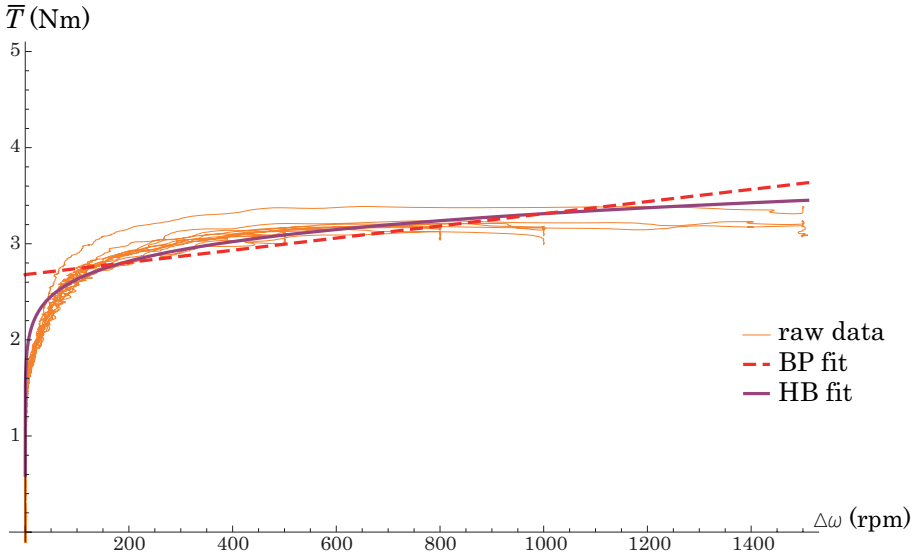

Figure 4.9: Torque in the engaged clutch condition, as obtained starting from the shear stress in the fluid

Furthermore, it has to be noticed that BP and HB models are usually used to represent the fluid behavior, while in this chapter the whole clutch behavior is considered and other phenomena, e.g. thermal and electric (eddy currents), can occur.

Chapter 5

Experimental analysis on different prototypes and performance indices

5.1 Introduction

After the design and the preliminary testing of the first clutch prototype, which confirmed the validity of the chosen architecture and pointed out some limits in modeling the MR behavior, two further prototypes of MR clutch were built on the basis of geometrical similarity, in order to analyze the effect of geometric parameters on the device properties. The torque characteristics of the three prototypes are investigated in the present chapter after performing some adjustments on the sealing, aimed at reducing the friction losses. For the envisaged application (overall efficiency of the powertrain), in addition to the minimum torque requirements in the engaged condition, the device is requested to have a low dissipation when it is disengaged. For this aim, two new performance indices were introduced, in order to evaluate the MR fluid exploitation and the device efficiency in the engaged and disengaged condition, respectively. The proposed indices are more specific and give additional information with respect to the turn-up ratio, which is usually used for MR clutches and brakes [87]. The experimental results for the three prototypes are then compared and discussed, with reference to the expected torques and on the basis of the introduced performance indices.

5.2 Prototypes geometry

Once the first prototype was developed, two additional prototypes were manufactured in order to evaluate any possible influence on the performance of the clutch. Those prototypes, which are represented in Fig. 5.1, differ from the first one, named as A in the figure, in the average diameter D (prototype B) and in the length L of the cylindrical gap (prototype C) as shown in Tab. 5.1.

In order to get an evaluation of the performance of all prototypes, the expected torques $\widetilde{T}_j^{ON}$ and $\widetilde{T}_j^{OFF}$ of the j prototype (j = B, C), related to the engaged and disengaged conditions, were estimated on the basis of the results obtained for prototype A, without performing any additional FE simulation of the magnetic field. To this aim, the normalized radial and axial coordinates $\bar{r} = r/R_j$ and $\bar{s} = s/L_j$, related to the average radius R_j and to the axial length L_j of the cylindrical gap of each prototype were introduced, respectively. The same distribution of the yield stress $\tau_j(\bar{r}, \bar{s}, \theta)$, function of the normalized radial and axial coordinates $\bar{r}$, $\bar{s}$ and of the angular coordinate θ was then assumed for all prototypes and that previously obtained for prototype A on the basis of FE analysis and MR fluid properties was considered to this aim.

With this assumption a linear dependence of the torques on the length L, together with a quadratic and a cubic dependence of the MR and of the viscous torque, respectively, on the average gap diameter is obtained for the cylindrical gap. In similar way, for the plane portion of the gap, a cubic and a fourth order dependence of the MR and of the viscous torque on the average diameter of the cylindrical gap were obtained, respectively. Therefore, with reference to Fig. 5.2, considering also that $D_e \simeq D$ and $D_i \ll D_e$, the expected MR and viscous torques for the j prototype are given by:

$$\hat{T}_j^{ON} = \hat{T}_j^0 + \hat{T}_j^v = \hat{T}_{A,c}^0 \left(\frac{D_j}{D_A}\right)^2 \left(\frac{L_j}{L_A}\right) + \hat{T}_{A,d}^0 \left(\frac{D_j}{D_A}\right)^3$$

Table 5.1: Geometrical properties and estimated characteristic torques

Prototype	D(mm)	L (mm)	$\widetilde{T}^{ON}$ (Nm)	$\widetilde{T}^{OFF}$ (Nm)	T^M (Nm)	$T^m(\Delta\omega)$ (Nm s/rad)
A	57	14	3.14	0.11	6.66	0.00068 $\Delta\omega$
B	62	14	3.77	0.15	8.16	0.00091 $\Delta\omega$
C	57	19	4.08	0.13	8.03	0.00080 $\Delta\omega$

$\widetilde{T}^{ON}$ and $\widetilde{T}^{OFF}$ calculated at 1500 rpm

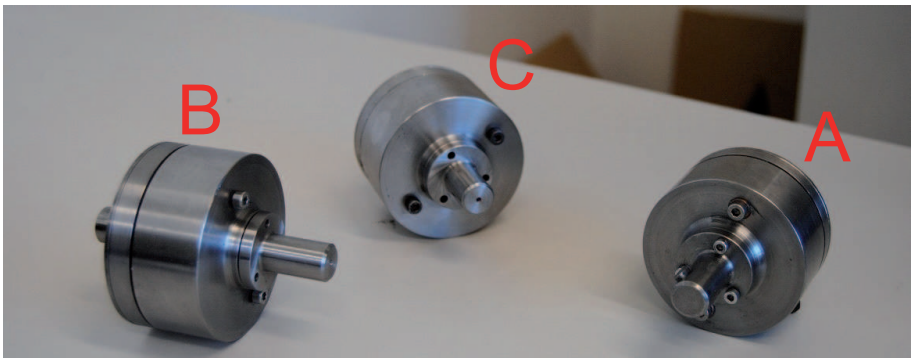

Figure 5.1: Built prototypes

$$+\hat{T}^v_{A,c}\left(\frac{D_j}{D_A}\right)^3\left(\frac{L_j}{L_A}\right)+\hat{T}^v_{A,d}\left(\frac{D_j}{D_A}\right)^4 \quad (5.1)$$

and

$$\hat{T}^{OFF}_j=\hat{T}^v_j=\hat{T}^v_{A,c}\left(\frac{D_j}{D_A}\right)^3\left(\frac{L_j}{L_A}\right)+\hat{T}^v_{A,d}\left(\frac{D_j}{D_A}\right)^4 \quad (5.2)$$

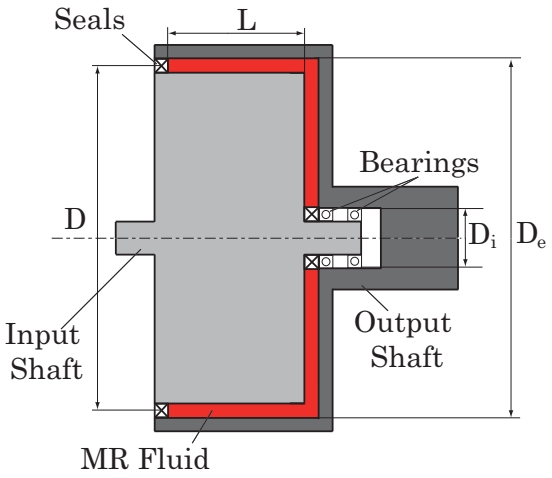

Figure 5.2: Prototype geometry

5.3 Prototypes performance indices: fluid exploitation and clutch efficiency

In order to evaluate the design of an MR clutch or brake and, in particular for the present case, to analyse the capability of the clutch prototypes, two performance indices are introduced to compare the actual magnetorheological torque and the actual disengaged torque to two ideal reference torques, i.e. the maximum magnetorheological torque and the minimum dissipative torque which can be ideally achieved, respectively:

$$\varepsilon^{ON}(\Delta\omega) = \frac{T^{ON}(\Delta\omega) - T^{OUT}(\Delta\omega)}{T^{M}} \tag{5.3}$$

$$\varepsilon^{OFF}(\Delta\omega) = \frac{T^{m}(\Delta\omega)}{T^{OFF}(\Delta\omega)} \tag{5.4}$$

In the previous equations, $T^{ON}(\Delta\omega)$ and $T^{OFF}(\Delta\omega)$ are the experimentally measured torque in the engaged and disengaged conditions respectively, $T^{OUT}(\Delta\omega)$ is the transmitted torque which is measured with the magnet removed from the clutch; T^{M} represents the ideal magnetorheological torque that can be obtained if the maximum shear stress τ^{M} is exploited throughout the whole gap and $T^{m}(\Delta\omega)$ is the minimum torque due to the viscous stresses in the fluid, that is ideally dissipated in the disengaged condition in case of perfect shielding of the magnet and negligible friction losses. T^{OUT} differs from T^{OFF}, since the latter includes any possible contribution due to the spurious magnetic field, in case of non perfect shielding.

Therefore, with the exploitation index, ε^{ON}, the actual magnetorheological torque of a given prototype is compared to the maximum torque which could be ideally achieved for the considered geometry. On the other side, the efficiency index ε^{OFF} evaluates the actual disengaged torque with respect to the minimum torque that would be obtained in the ideal case of no friction or losses due to spurious magnetic field.

The indices ε^{ON} and ε^{OFF} are bound in the [0 1] range in absence of shear thinning or thickening phenomena and, separately, evaluate the performance of a given MR clutch or brake design in the engaged and disengaged condition respectively. For this reason they provide a more in-depth insight with respect to the usually employed turn-up ratio ξ, which is simply defined as the ratio $T^{ON}/T^{OFF}(\Delta\omega)$ (see [87]). The turn-up ratio, indeed, cannot be compared to any absolute reference

value, in order to be able to evaluate a given design, and doesn't show how improvements can be achieved, i.e. with reference to the ON or to the OFF condition. Moreover, it can be seen that, if T^{OUT} can be neglected in comparison with T^{ON}, the turn-up ratio can be obtained on the basis of the previously defined indices, by the following approximate expression:

$$\xi(\Delta\omega) = \frac{T^{ON}(\Delta\omega)}{T^{OFF}(\Delta\omega)} \approx \varepsilon^{ON}(\Delta\omega)\varepsilon^{OFF}(\Delta\omega)\frac{T^{M}}{T^{m}(\Delta\omega)} \tag{5.5}$$

The maximum magnetorheological torque T^M of the developed prototypes A, B and C is obtained considering the maximum shear stress τ^M ($\tau^M \approx 55$ kPa for the selected fluid) and the given geometries. The following relationship is obtained:

$$T^M = T_d^M + T_c^M = \pi\tau^M \left(\frac{D_e^3 - D_i^3}{12} + \frac{D^2}{2}L\right) \tag{5.6}$$

where T_d^M and T_c^M are the maximum magnetorheological torques that can be obtained by the plane and the cylindrical portion of the gap.

At the same time, the minimum torque $T^m(\Delta\omega)$, that is ideally dissipated in the disengaged condition, due to the only viscous contribution, can be evaluated by replacing τ with the viscous stress τ_v. In this case the following relationship is obtained:

$$T^m(\Delta\omega) = T_d^m(\Delta\omega) + T_c^m(\Delta\omega) = \pi\frac{\eta\Delta\omega}{s}\left(\frac{D_e^4 - D_i^4}{32} + \frac{D^3}{4}L\right) \tag{5.7}$$

Considering the actual geometry of the three prototypes the numerical values given in Tab. 5.1 were obtained.

5.4 Experimental Testing of the three prototypes

The transmitted torque was measured for each of the developed prototypes in four different clutch configurations:

1) without the MR fluid and with the PM removed from the clutch, in order to get only the friction contribution to the measured torque;

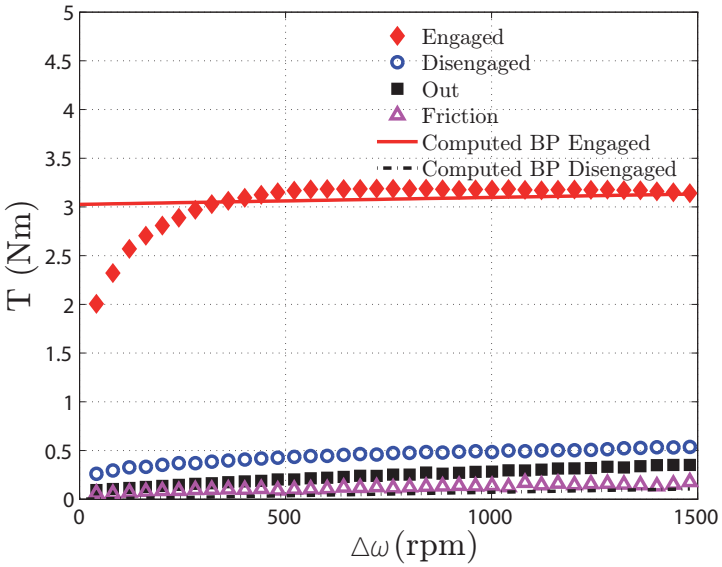

Figure 5.3: Characterization of prototype A

2) with the gap filled and the PM removed from the clutch (OUT condition), to get the friction and viscous contribution to the transmitted torque;

3) with the gap filled and the PM in the OFF position, to get the torque transmitted in the disengaged condition and evaluate any contribution due to spurious magnetization of the fluid (unproper MR gap shielding);

4) with the gap filled and the PM in ON position, to get the torque transmitted in the engaged condition.

Each test was carried out at room temperature and lasted about 20 s; due to the shortness of the tests, any possible temperature effect on the fluid was neglected.

5.5 Results and discussion

The results obtained with the three prototypes are shown in Fig. 5.3, Fig. 5.4 and Fig. 5.5, respectively, together with the expected torques,

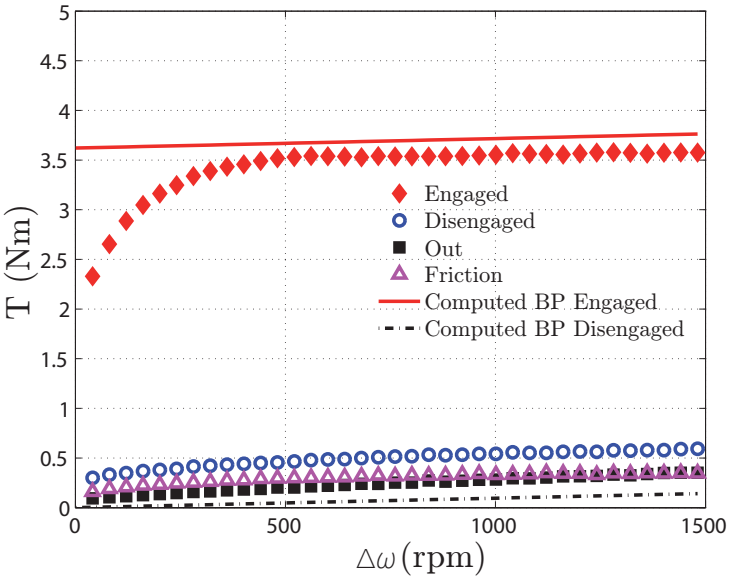

Figure 5.4: Characterization of prototype B

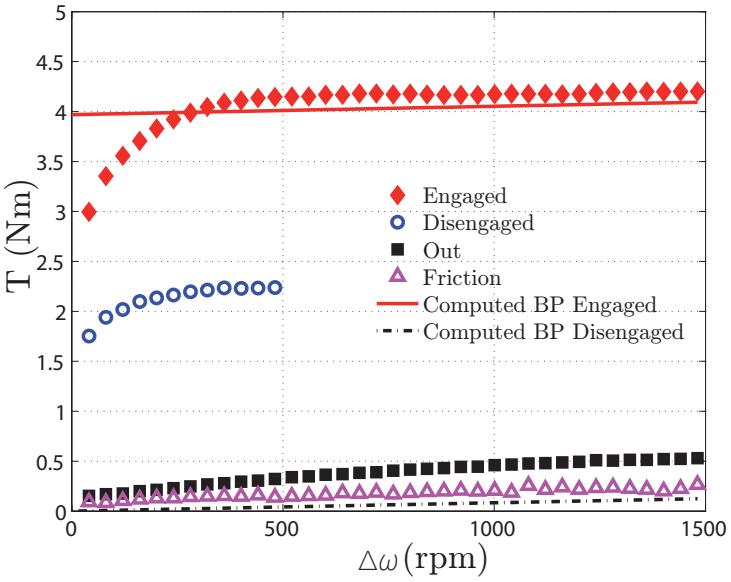

Figure 5.5: Characterization of prototype C

calculated considering the BP model. Each experimental curve was obtained as the average of five acquisitions. The relative standard deviation obtained from the measured data was less than a few percent and gives an evidence of the good repeatability of the test. The computed torques did not consider any friction contribution.

The torque measured without MR fluid and permanent magnet is due to the sliding friction of the seals and to the rolling resistance of the bearings. By testing the clutches filled with MR fluid and without PM (OUT) it is possible to isolate the viscous contribution of the unmagnetized fluid. When the PM is in the OFF position, the clutch is disengaged. The torque transmitted in this configuration is usually higher than in the OUT condition because the MR fluid gap is not completely shielded from the magnetic field and the spurious magnetic field causes an undesired, though small, transmission of torque.

In all cases, as expected, when the PM is in the ON position and the clutch is engaged, the transmitted torque is the highest possible. Fig. 5.3, 5.4 and 5.5 show a fairly good agreement between the expected and the experimental torques in the engaged condition and between the expected and experimental viscous torques. In addition, for the prototypes A and B, a very small difference between the measured OUT and OFF (disengaged) torques was observed, indicating a very effective shielding of the magnet in the disengaged condition. On the contrary, for prototype C, which was somewhat longer than prototype A, a too high spurious magnetization was observed. This shows how, in this case, the shielding effect of element no.8 (Fig. 3.14) could not be properly obtained simply by similarity and how a detailed FE magnetic analysis would be mandatory. Moreover, for this prototype the magnetic field in the disengaged condition caused MR fluid leakage through the seals and for this reason tests were interrupted at 500 rpm.

In order to deepen the analysis and verify the accuracy of the predicted magnetorheological torques (estimated on the basis of the FE simulation carried out on prototype A) the magnetorheological torque for each prototype was obtained by subtracting the torque relative to the OUT condition from that relative to the ON condition. The comparison is shown in Fig. 5.6. As it can be seen, for all the prototypes the yield torque is significantly overestimated and this was attributed to a non proper definition of the yield strength given in the MR fluid data sheet.

However, a fairly good assessment of the engaged torque for $\Delta\omega > 500$ rpm was obtained by the presented methodology.

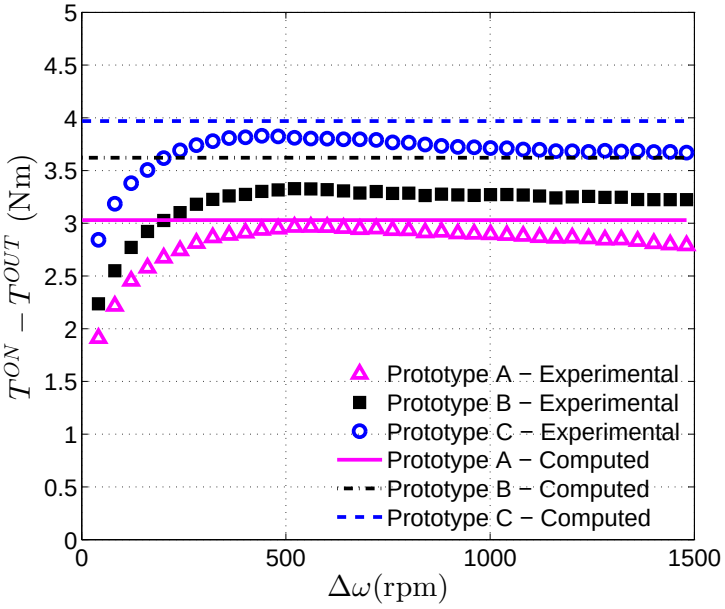

Figure 5.6: Comparison between computed (dashed lines) and experimental net torques for the engaged clutch

The previously defined fluid exploitation index (ε^{ON}) and the clutch efficiency index (ε^{OFF}) are shown in Fig. 5.7 and Fig. 5.8. For all prototypes the fluid exploitation results in the range [0.25 0.35] at yielding and in the range [0.40 0.55] in slip condition. Such relatively low values were due both to the magnetic field, which had a cyclical periodicity, and to the very low magnetization of the MR fluid in the circular plane gap.

On the other hand, the ε^{OFF} index shows how seals and bearings give a friction contribution which is significantly higher than the viscous contribution of the MR fluid, especially at low speed. For prototype C, in particular, the spurious magnetization gave an additional contribution to losses which resulted in even lower index values.

Finally, the turn-up ratio ξ, defined as the T^{ON} to T^{OFF} ratio, is given in Fig. 5.9. As already discussed, it mainly represents a relative indication of the torque gain from the disengaged to the engaged condition and its interpretation is somewhat ambiguous since it is neither referred

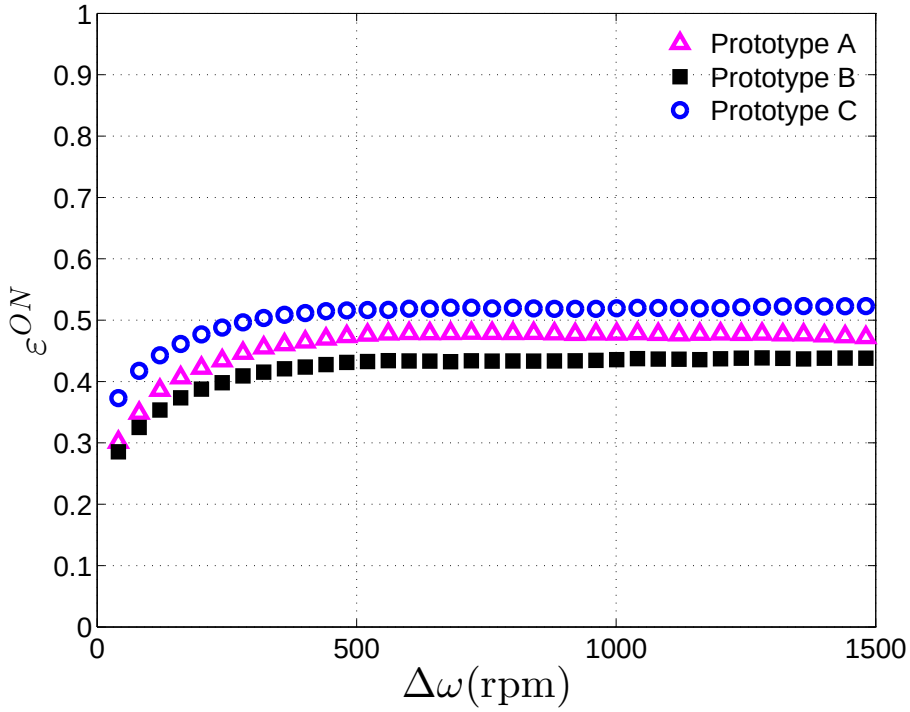

Figure 5.7: Fluid exploitation index (ε^{ON})

to any precise value nor bounded. On the contrary the exploitation and efficiency indices give precise information about improvements that can be obtained with reference to the engaged and disengaged conditions, separately.

5.6 Conclusions on the characterization of the three prototypes

The theoretical and experimental characterization of the torque transmission of three prototypes of an MR fluid clutch with permanent magnet was presented and discussed in the chapter. For the envisaged application the clutch has to be capable of transmitting a given requested torque, when engaged, and to have a very small dissipation if disengaged. For this reason two new indices were introduced and used to independently

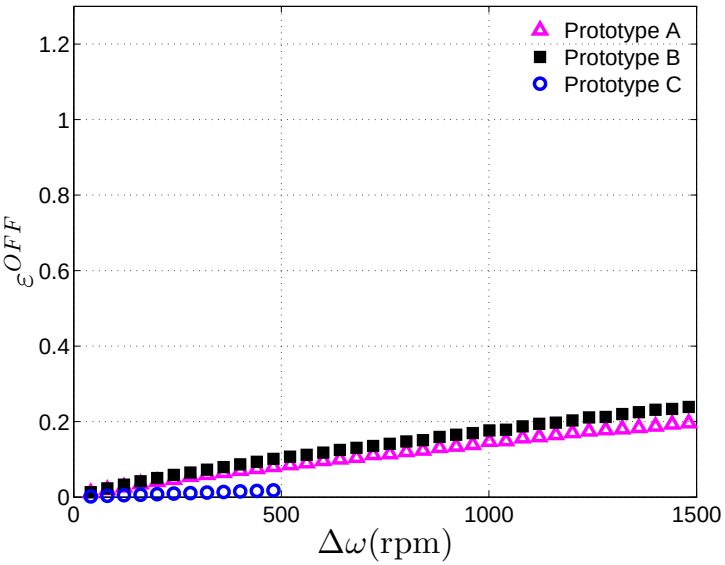

Figure 5.8: Efficiency index in disengaged condition (ε^{OFF})

evaluate the prototype performances with reference to the engaged and disengaged conditions. From this point of view the newly proposed indices are much more useful than the turn-up ratio, since they give a precise and quantitative indication about the possibility of improving a given design, with reference to the ON and to the OFF state. The analysis allowed to point out the importance of the magnetic field distribution and intensity in determining the MR fluid exploitation. The exploitation index was between 40% and 55%, indicating the possibility of further design improvement. The relatively low exploitation index was mainly due to the low yield stress achieved in the plane portion of the gap and marginally due to the circular periodicity of the yield stress in the cylindric portion of the gap.

With reference to the disengaged condition, it was shown how the efficiency was affected by friction losses and by the spurious magnetization of the fluid. At 1500 rpm the efficiency index was about 20% for two of the prototypes, while one of them showed a poor shielding of the MR gap, giving a very low efficiency (few %).

The exploitation and efficiency indices appeared more appropriate

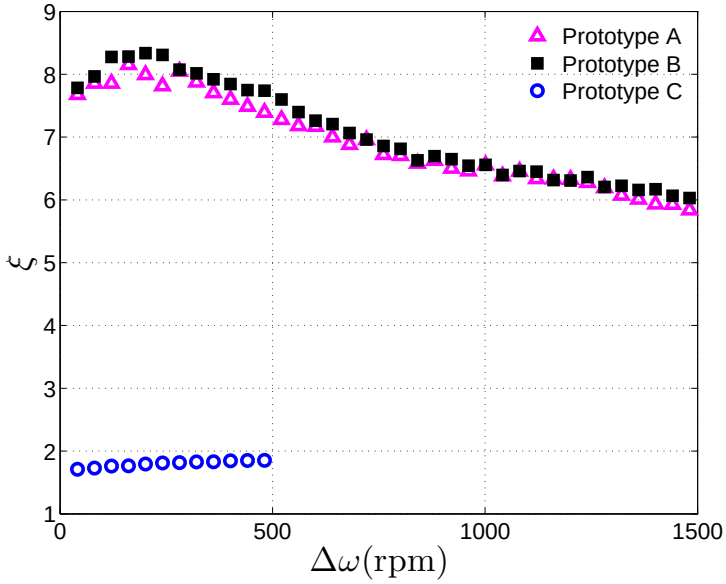

Figure 5.9: Turn-up ratio (ξ)

than the sometimes used turn-up ratio, to give an in-depth evaluation of the performance of an MR clutch or brake and are proposed for future design evaluations.

The obtained experimental results validated the FE based analytical model but pointed out the limits of the geometric similarity assumption and therefore the need of specific magnetic FE analyses to accurately predict torque transmission in all conditions. At the same time, the experimental activity confirmed the feasibility of the developed MR device for the selected application (i.e. for the vacuum pump in diesel engine), in compliance with the constraints of small available volume, axial load absence and fail-safe operation. The obtained torque guarantees that normally, in the engaged condition, there is no slip and then there is no dissipation, with the exception of a short engagement transient.

Chapter 6

Design and experimentation of a novel MR clutch prototype

Once the experimental campaign on the three prototypes was concluded, some drawbacks of the clutch design arose, which led to the design of a novel prototype, which is the one successfully presented at the end of the funded project. In particular, the main drawbacks of the previous prototypes were:

- leakages from the external sealing at high speed;
- torque loss due to the friction on the external sealing;
- undesired magnetization of the fluid in the OFF condition;
- absence of the magnet movement system.

At the same time, the design specification (Tab. 6.1) were lightly modified, allowing the design of a bigger prototype with higher torque value in ON condition.

6.1 Design of the novel prototype

The basic idea which drove the design of the novel prototype was to remove the external sealing which allowed some leakages and caused torque loss due to the friction, and move it to the internal part of the

Outer Diameter	$<$	75 mm
Length	$<$	50 mm
Maximum engaged Torque	$>$	5 Nm
Disengaged Torque at 1500 rpm	$<$	0.5 Nm
Rotational speed	$<$	3000 rpm

Table 6.1: Design specifications for the novel prototype

clutch. For this reason, a new gap shape was conceived, which has two cylindrical and two plane parts, which allows to place the sealing at the inner diameter. The new gap shape was a challenging idea, which gave rise to a difficult mechanical design phase aimed at developing a novel feasible device.

In Fig. 6.1 the assembly of the new clutch prototype is shown. The primary group is composed of a shaft fixed to a bell-shaped rotor, whereas the secondary shaft has a more complex layout, fulfilling external case and magnet housing functions. The MR fluid is interposed between the primary and the secondary groups as in the previous prototypes, but its shape is more complicated, in order to reduce friction losses and prevent leakages. Indeed, both the seals which confine the fluid are positioned at low diameters, reducing the effects of torque loss due to friction and the increase of pressure at the seals due to the fluid centrifugation.

Two holes are made axially in the front cover of the external case in order to allow the fill the gap with the MR fluid. Primary and secondary parts are aligned by a couple of bearings, one of which also guarantees the axial fixing of the parts by means of two Seeger-rings.

The fluid magnetization is provided by a rare earth NdFeB magnet, composed of four 90degree parts with diametral magnetization. As in the previous prototype the magnet can slide axially in the housing chamber. Two magnet steady positions are possible: the former, which is shown in Fig. 6.1, consists in placing the permanent magnet close to the MR gap (on the right of the chamber in Fig. 6.1) in order to assure the fluid magnetization required by the engaged clutch use; the latter, on the contrary, consists in placing the permanent magnet far away from the MR gap (on the left of the chamber in Fig. 6.1), shielding the magnetic field by means of the external ferromagnetic ring of the case.

The magnet, by means of an o-ring seal, splits the chamber in two parts which result hermetically separated. The primary and secondary

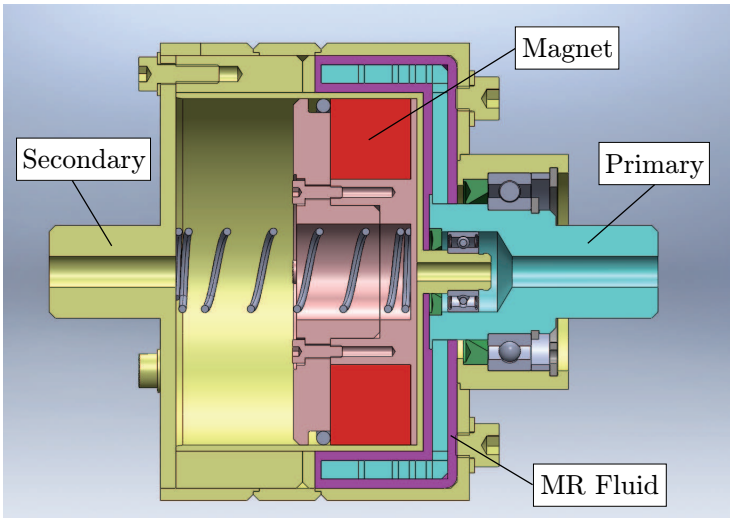

Figure 6.1: Novel prototype drawing

shafts present a hole on their axis, which connects each part of the magnet chamber with an external pressure source. A spring pushes the magnet toward the fluid gap zone in order to guarantee the fluid magnetization in the case the pressure in both chambers resulted the same.

6.1.1 Primary group

The primary group (Fig. 6.2) is composed of alternated ferromagnetic and non-ferromagnetic parts, as resulted from finite elements simulations. The primary shaft is fixed to the bell-shaped part by means of a welding, whereas the thin discs which form the bell are connected by axial pins.

Four holes were made in the flat part of the bell to connect the external and internal fluid gaps, in order to achieve a good filling.

6.1.2 Magnet group

The annular NdFeB magnet is supported by two shields whose thickness was chosen by the finite element simulations (magnetic field orientation in ON and OFF configurations, axial forces) and due to the necessity of housing the o-ring pneumatic sealing, which allows the magnet pneumatic movement.

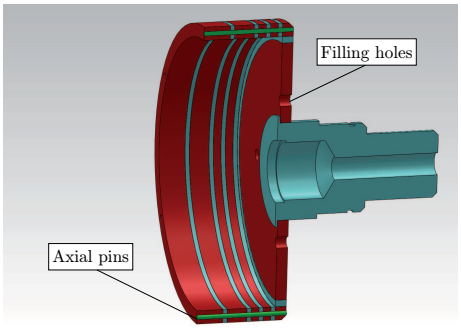

Figure 6.2: Primary group drawing

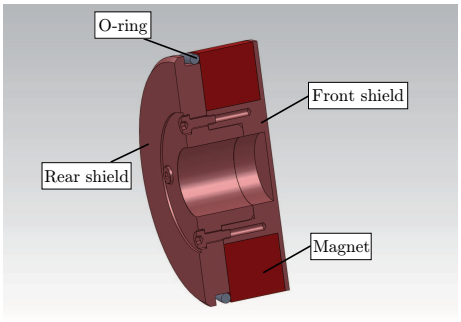

Figure 6.3: Magnet group drawing

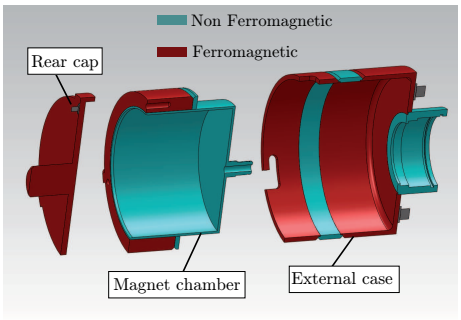

Figure 6.4: Secondary group drawing

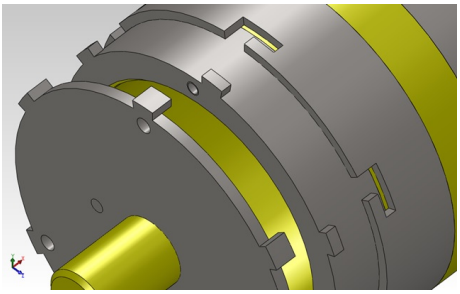

Figure 6.5: Bayonet coupling of the secondary group parts

The shields can be unmounted by removing four axial screws, in order to permit the magnet assembly and positioning.

6.1.3 Secondary group

The secondary group (Fig. 6.4) is made up of three components. Each component is made of ferromagnetic and non-ferromagnetic parts which are welded together.

The magnet chamber can slide within the external case in order to assure the complete disassembling of the prototype. The rear cap is fixed to the magnet chamber by means of three screws. The circumferential locking among the parts is obtained by the bayonet coupling shown in Fig. 6.5.

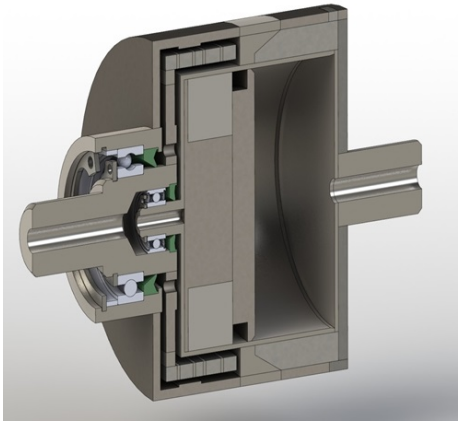

Figure 6.6: Render of the novel prototype

6.2 Production and experimentation of the novel prototype

In Fig. 6.6 the render drawing of the new prototype is shown, as it was obtained at the end of the design phase. Subsequently, the prototype was built and it is shown in Fig. 6.7.

In Fig. 6.8 the disassembled prototype is shown and the main parts can be identified: in rightward order, the external case, the multidisc rotor, the internal cylinder, the magnets system with shields and pneumatic o-ring, the spring and the rear cap.

In order to test the pneumatic magnet movement, whose design procedure was illustrated for the first prototype in § 3.4, the test rig shown in Fig. 6.9, was developed. It can measure the magnet displacement for different pressure values imposed in the magnet chamber.

The linear potentiometer no.1 is fixed to the front side of the magnet system and on the other side of the magnet pressure is imposed. In particular, by means of the switch no.3, the right room (Fig. 6.1) of the prototype can be connected either with the atmosphere or with the vacuum boost no.5. The pressure in the vacuum boost is determined by the vacuum pump no.6 which draws air continuously and the pressure value is measured by the manometer no.7. The steady value of the pressure in the vacuum booster was 0.2 bar.

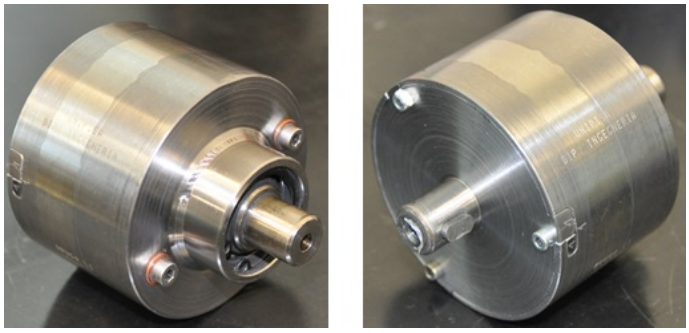

Figure 6.7: The novel prototype

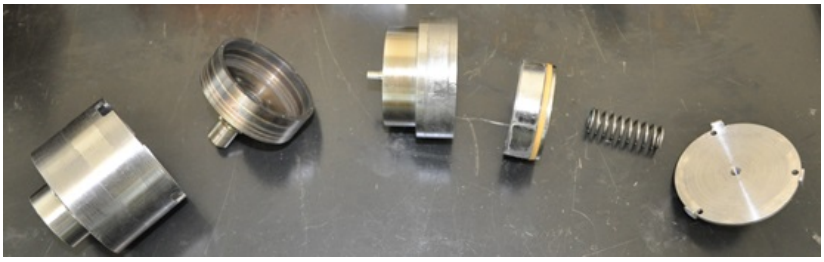

Figure 6.8: The novel prototype - Disassembled

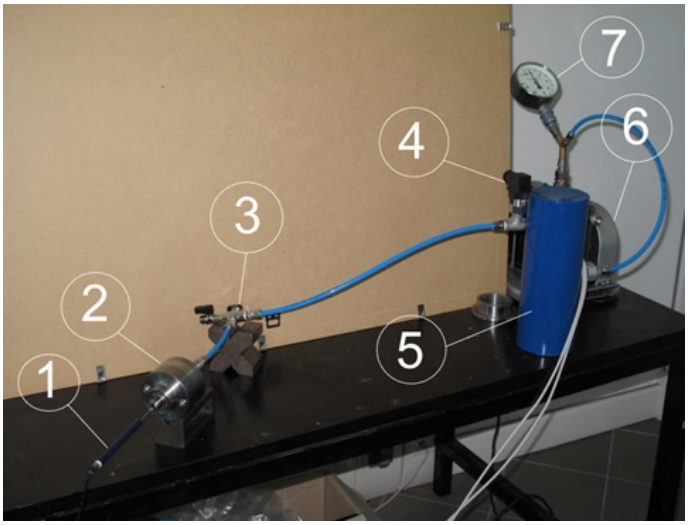

Figure 6.9: The pneumatic movement test rig

6.2.1 Movement tests results

Two movement test were performed:

- from ON to OFF (ON–OFF): starting from the atmospheric pressure, the right chamber is quickly connected to the booster, by means of the switch no.3, and the magnet displacement is measured. This test simulates the disengagement of the clutch which should occur once the steady pressure in the power-brake boost is reached. In such a way, the magnet is drawn in the disengaged position by the difference of pressure acting on the two sides of the magnet, whose effect exceeds the spring and magnetic forces.

- from OFF to ON (OFF–ON): starting from the vacuum boost pressure, the right chamber is quickly connected to the atmosphere and the magnet displacement is measured. This test simulates the engagement of the clutch which should occur once the pressure in the power-brake rises. The magnet is pushed in the engaged position by the effect of the spring and the magnetic forces.

Figures 6.10 and 6.11 prove the feasibility of the pneumatic actuation. The magnet displacement d, which is assumed 0 when the magnet is

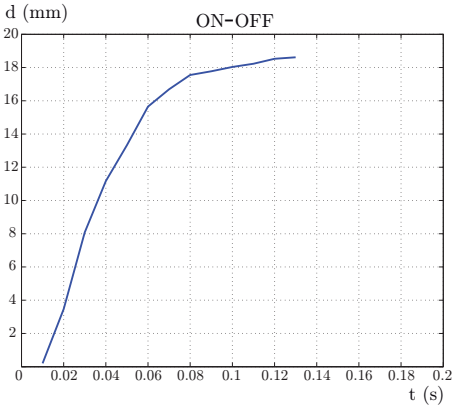

Figure 6.10: ON–OFF movement - Experimental result

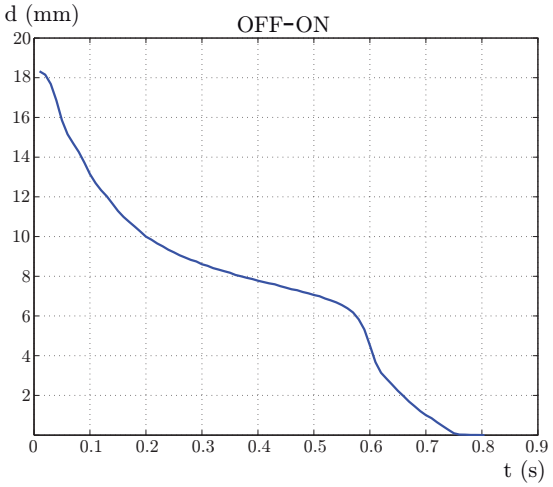

Figure 6.11: OFF–ON movement - Experimental result

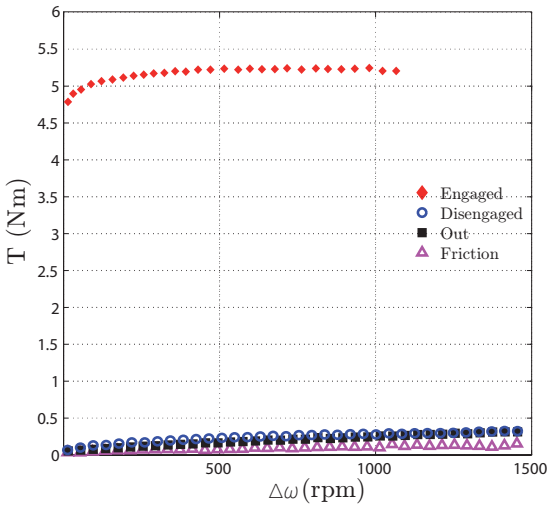

Figure 6.12: Novel prototype - Experimental characterization

in the disegnaged condition, is plotted against time. The total magnet stroke is 19 mm. Indeed, the engagement time is about 0.75 s, which is lower than the value indicated in the design specification (Tab. 6.1).

6.2.2 Torque transmission results

As for the previous prototypes, the novel prototype was tested at the bench described in Chapter 4 in the four different conditions listed in Chapter 5.

The torque characteristics fulfilled the design specification in both the ON and OFF conditions. Indeed, the torque transmitted by the engaged clutch, as shown in Fig. 6.12 is higher than 5 Nm in almost all the operating range, whereas the torque in the OFF condition was lower than 0.5 Nm.

In addition, the difference between the OFF clutch operating condition and the no-magnet one is negligible, proving the goodness of the magnetic field shielding for the new prototype.

The performance indices (see Chapter 5) were computed for the novel prototype and compared to the one obtained for the three previous ones.

Concerning the fluid exploitation index (Fig. 6.13) the new prototype is worse than the previous one, due to the different geometry of the MR

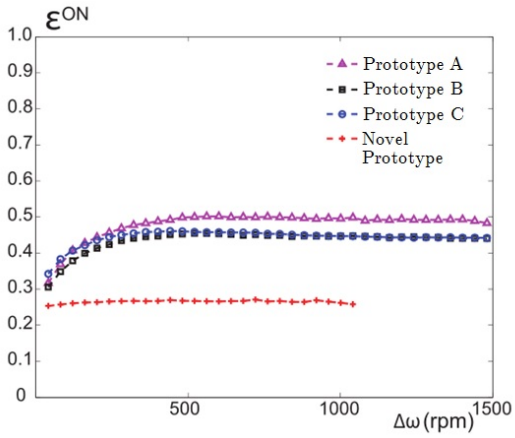

Figure 6.13: Fluid exploitation index - Comparison between prototypes A, B, C and novel prototype

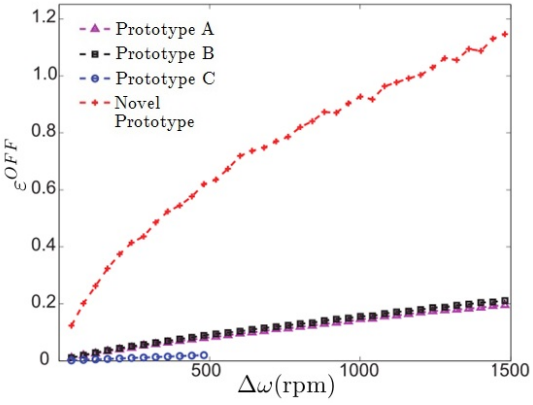

Figure 6.14: Efficiency index - Comparison between prototypes A, B, C and novel prototype

gap. Indeed, the magnetic field in the external cylindrical gap is weak and decreases the value of the index. On the contrary, the efficiency is very high, expecially at high speed, where the shear thinning phenomenon appears, and the torque absorbed by the clutch is lower than the one predicted by the Newtonian model ($\eta^{OFF} > 1$).

As a final remark, the design specifications were all fulfilled with the new geometry and no leakages occurred, confirming the goodness of the design.

Chapter 7

Thermal effects on the torque characteristics of the MR clutch

In this chapter the torque characteristic of the first magnetorheological clutch (Chapter 3) is investigated focusing on the influence of temperature. An experimental campaign was carried out on the test bench described in Chapter 4, which was specifically equipped with a caulk oven to heat the clutch working environment up to 80°C. The torque characteristics were measured by a torquemeter and acquired as a function of the speed difference between the primary and secondary clutch parts and the environment initial temperature. Both the fluid temperature and the clutch case temperature were monitored at the beginning and at the end of each test.

In the literature, few papers deal with the effect of temperature on MR fluids and elastomers. In [88] the apparent viscosity in MR dampers was studied as a function of the magnetic field and temperature by means of a shear rate controlled rheometer. Arrhenius equation was used to fit results which showed the decrease of viscosity with rising temperature. In [89] the rheological properties of an in-house developed fluid were investigated in relation to the magnetic field and temperature. Data were fitted according to power law models [90]. In addition to MR fluids, also MR grease temperature properties were investigated in [91] and [92] revealing a decrease of viscosity as the temperature was increased. In particular in [91] the complex modulus of the fluids was investigated as a

function of temperature.

7.1 Experimental procedures at room temperature

As shown in Fig. 4.3 the power law speed-profile was chosen as the reference test for characterizing the MR clutch, which is able to accurately identify the yield torque, thanks to the low rate at low speed. Figure 7.2 shows the torque profile obtained imposing the speed profile shown in Fig. 7.1, starting from environmental temperature $T \simeq 20°C$.

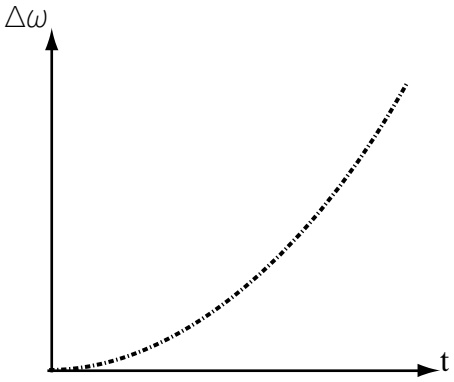

Figure 7.1: Difference in shafts speed time history. Power-law speed profile.

In addition to the test procedure shown in Fig. 7.1, an alternative speed profile of the primary group was employed to simulate the engaging phase of the clutch. According to this new profile, once the maximum speed was reached, the speed was kept constant for 5 s and then the power ramp was inverted and the speed decreased, as shown in Fig. 7.3.

Figure 7.4 shows the torque profile obtained. The first part of the torque curve is comparable to that already shown in Fig. 7.2. Then, at constant speed, a torque decrease was observed and, finally, during the decelerating phase, the torque resulted lower than that previously obtained for each $\Delta\omega$. The loss in the transmitted torque can't be explained by any classical model so an analysis of the clutch torque behavior was conducted at different temperatures.

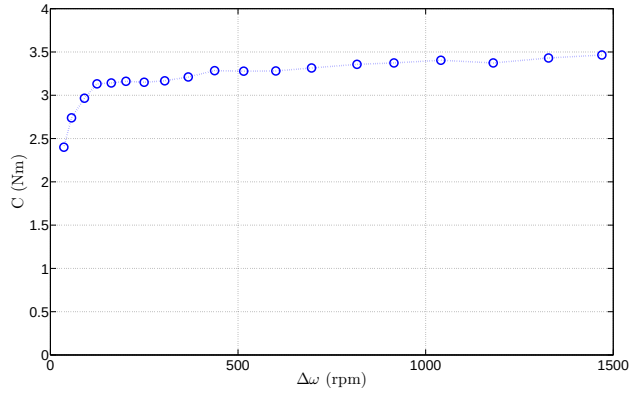

Figure 7.2: Torque profile at 20° C.

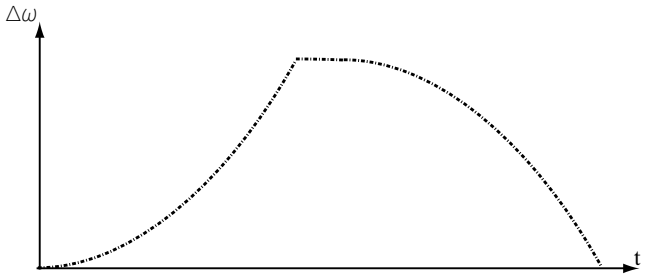

Figure 7.3: Alternative testing procedure aimed at simulating clutch engagement.

7.2 Tests carried out at different temperatures

The test bench described in Chapter 4 was equipped with a caulk oven which can warm the environment surrounding the clutch. As shown in Fig. 7.5 the caulk environment was warmed up by four heating elements supplied by an adjustable AC transformer and the case was caulked by mineral wool and refractory tape.

Three thermocouples were used to measure the temperature. Two thermocouples (TC1 and TC2) were secured on the external case of the clutch and one thermocouple (TC3) was included coaxially in the screw cap of the MR fluid, in order to measure the corresponding fluid temperatures (Θ_1, Θ_2, Θ_3). A schematic drawing of the thermocouples

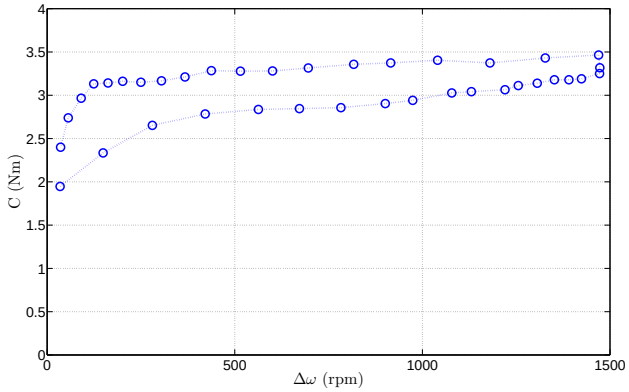

Figure 7.4: Torque profile at 20° C following the testing procedure 2.

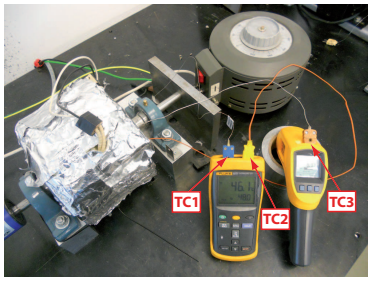

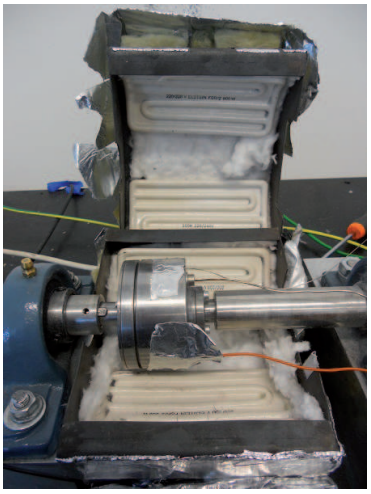

Figure 7.5: External and internal view of the oven.

positioning is shown in Fig. 7.6, whereas the real positioning on the tested prototype is shown in Fig 7.7. The temperature was displayed on two thermocouple readers.

By means of the AC transformer the heating elements were slowly heated up to the average value of the temperature read by TC1 and TC2 that was about 5°C higher than the desired environmental temperature. Then the power supply was switched off to let the temperature level into

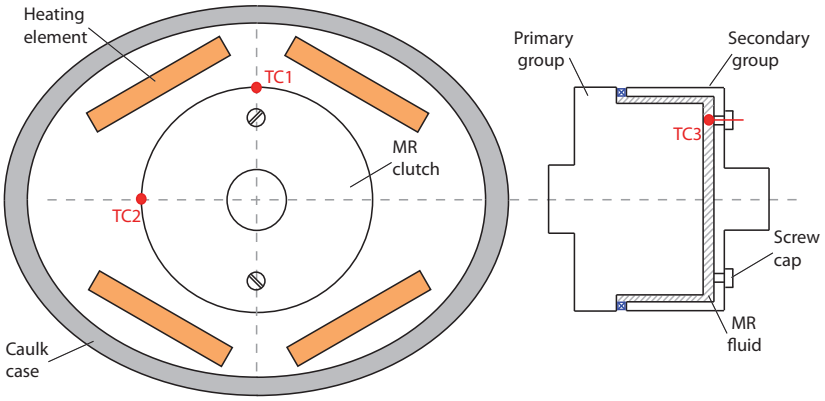

Figure 7.6: Schematic frontal view of the oven and lateral view of the clutch.

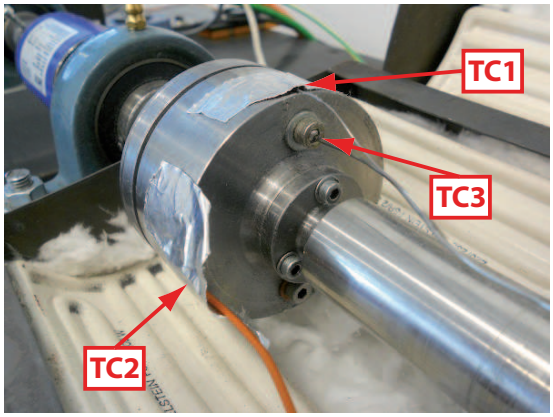

Figure 7.7: Thermocouple positioning.

the whole oven room. Once the desired value of temperature was read on the thermocouple readers the test was started.

The speed of the primary shaft was imposed following the profile shown in Fig. 7.1. The torque measured by the torquemeter and the primary shaft speed measured by the encoder were acquired at 100Hz. The tests were conducted starting from six different initial temperatures (20°C, 30°C, 40°C, 50°C, 60°C, 80°C) and three tests were repeated for each temperature value. In addition the temperature was measured 30s after the end of each test, when the steady temperature value was

reached and the thermocouples transient could be neglected. Table 7.1 summarizes the acquired temperature values.

	Initial			Final		
Ref. Θ (°C)	Θ_1 (°C)	Θ_2 (°C)	Θ_3 (°C)	Θ_1 (°C)	Θ_2 (°C)	Θ_3 (°C)
20	21	21	21	41	41	38
20	22	22	22	41	40	38
20	22	22	22	41	40	39
30	30	30	30	47	46	44
30	32	31	32	47	46	46
30	32	31	32	50	48	47
40	42	42	43	58	56	56
40	42	41	42	60	58	58
40	43	42	43	59	56	57
50	52	51	50	68	67	63
50	52	51	52	67	65	65
50	50	49	51	65	62	64
60	62	61	60	73	71	71
60	62	60	62	76	73	74
60	60	58	61	75	70	73
80	84	82	82	97	93	93
80	81	77	81	94	89	92
80	81	77	82	94	88	92

Table 7.1: Acquired temperatures.

For each test, the initial values of Θ_1, Θ_2 and Θ_3 are similar, proving a uniform temperature distribution within the oven. In particular, the difference between the higher and lower measured values never results more than 5%. Similarly, at the end of each test the temperature distribution is fairly uniform.

7.3 Experimental results and fitting

The raw acquired data were filtered by a moving average (100 samples) to reduce electromagnetic noise. Results are plotted in Fig. 7.8. The influence of the initial temperature is clear and produces an almost constant loss in the transmitted torque, which at the highest temperature is of about 0.8 Nm over the whole examined speed range.

In order to identify more specifically the temperature dependence, the average value of the measured torque was calculated for the tests conducted at the same temperature. Figure 7.9 shows the averaged results. The differences between lower and higher starting temperature result remarkable, whereas the difference between two next temperature values (e.g. 30°C and 40°C) are comparable with the measurement error.

The average torque data set shown in Fig. 7.9 was then used to find a fitting surface $T(\Delta\omega, \Theta)$. In particular, on the basis of [90, 92], a formulation composed of a power law to represent the relationship $T(\Delta\omega)$ and the Arrhenius law to express the dependence $T(\Theta)$ was chosen as

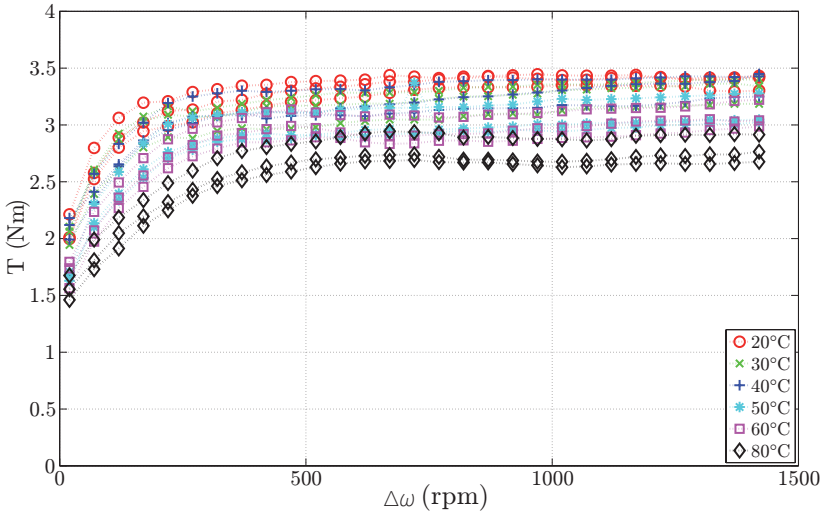

Figure 7.8: Acquired torque data (three curves for each temperature).

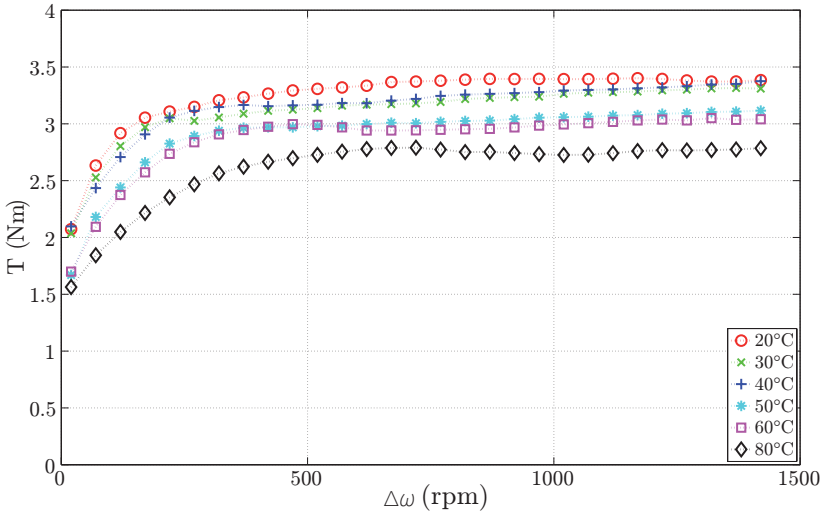

Figure 7.9: Averaged torque data.

follows

$$T(\Delta\omega, \Theta) = A\Delta\omega^n e^{-\frac{B}{\Theta}} \tag{7.1}$$

where $\Delta\omega$ and Θ are the speed difference and initial temperature (measured in K) considered in the data set, T is computed as the mean of the

acquired torque values corresponding to given $\Delta\omega$ and Θ and A, B and n are the parameters to be determined by the fitting technique.

The *MatLab Curve Fitting Tool* was used to obtain the parameters values listed in Tab. 7.3 which, if included in the Eq. 7.1, give the surface represented in Fig. 7.10.

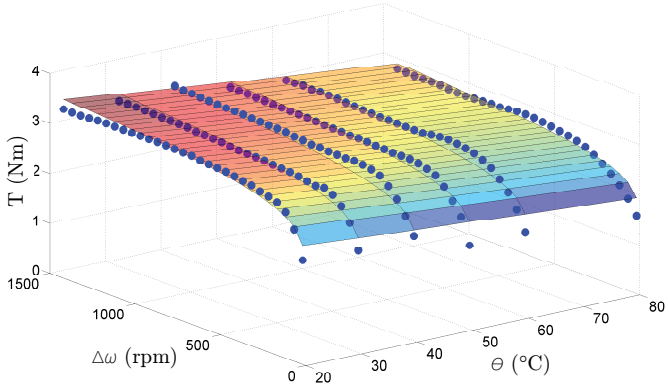

Figure 7.10: Torque fitting surface.

A (Nm/rpm^n)	0.5227
n	0.09611
B (K^{-1})	-360.5

Table 7.2: Fitting parameters.

The R-square value computed for the fitting was 0.8793. In order to improve the goodness of fit, the acquired average data were manipulated considering the fluid warming during each test. The temperature of the fluid (measured by thermocouple 3) at the beginning (Θ_{3i}) and at the end (Θ_{3f}) of each test was considered along with the energy dissipated (E) during the test, which, referring to a generic test time ($\bar{t}$), is given in Eq. 7.2.

$$E(\bar{t}) = \int_0^{\bar{t}} T(t)\Delta\omega(t)\ \mathrm{d}t \tag{7.2}$$

The fluid temperature value during the test was supposed to vary, between its initial and final values, proportionally with the dissipated energy, i.e.

neglecting any thermal transient. The updated temperature value (Θ), referring to a generic test time ($\bar{t}$), then resulted

$$\Theta(\bar{t}) = \Theta_{3i} + \frac{E(\bar{t})}{E(t_f)}(\Theta_{3f} - \Theta_{3i}) \tag{7.3}$$

where $E(t_f)$ is the energy total energy dissipated at the end of each test. On the basis of the updated temperature values, the *MatLab Curve Fitting Tool* was used to find the parameters of the relationship defined by Eq. 7.1. The new fitting parameters are listed in Tab. 7.3.

A (Nm/rpm^n)	0.4146
n	0.1123
B (K^{-1})	-410.6

Table 7.3: Fitting parameters.

The goodness of fit resulted enhanced as proven by the R-square index which resulted 0.9085.

7.4 Assessment of the temperature effect on the shear stress

In order to generalize the obtained results, the dependence of the shear stress on the temperature was estimated, with some simplifying hypotheses. The torque T is function of the speed difference $\Delta\omega$ and of the temperature Θ and is composed of two parts

$$T(\Delta\omega, \Theta) = T^d(\Delta\omega, \Theta) + T^c(\Delta\omega, \Theta) \tag{7.4}$$

where T^d is the torque transmitted by the discoidal surface of the MR fluid and T^c is the one transmitted by the cylindrical gap.

In the clutch design phase, finite element simulations were carried out [3] to obtain the distribution of the magnetic field and the shear stress τ_0 was then calculated on the basis of the formulation proposed by Carlson in [52] (Eq. 7.5)

$$\tau_y = 271700\,\phi^{1.5239}\tanh\left(6.33\,10^{-6}\,H\right) \tag{7.5}$$

where ϕ is the volume particle fraction which is 0.4 for the selected fluid, H is the magnetic field expressed in A/m computed at $\Theta = 20$°C and τ_0

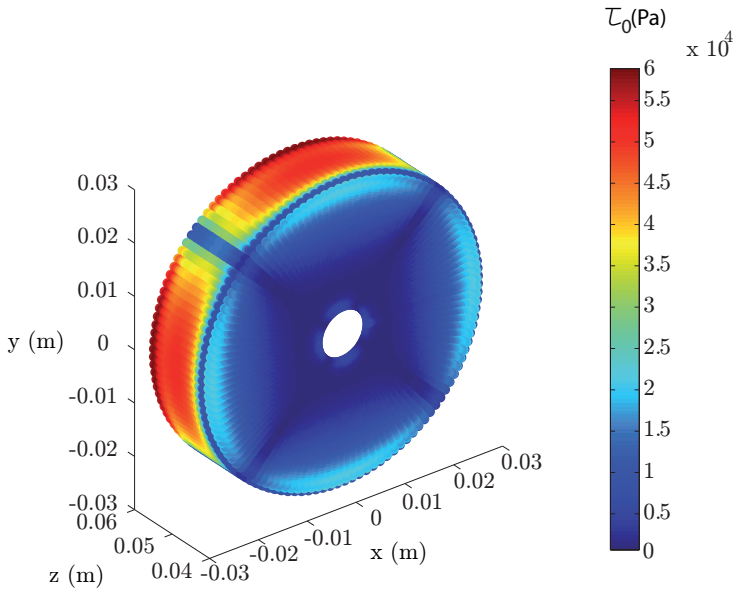

Figure 7.11: Computed yield stress distribution.

is expressed in Pa. Figure 7.11 shows the distribution of τ_0 in engaged condition. The simulations were used to compute the ratio α between T_d and T_c at room temperature ($\Theta = 20°\text{C}$) and at yielding ($\Delta\omega = 0$)

$$\alpha = \frac{T_d(0, 20°\text{C})}{T_c(0, 20°\text{C})} = 0.122 \tag{7.6}$$

The obtained value proves the low contribution of the discoidal MR gap due to both the geometry and the low magnetic field intensity; considering also the results reported by Sahin in [92] on MR greases, a low value of the magnetic field is expected to produce a fairly constant shear stress with respect to temperature and therefore

$$T_d(\Delta\omega, \Theta) \simeq T_d(\Delta\omega) = \alpha T_c(\Delta\omega, 20°\text{C}) \tag{7.7}$$

The amount of torque due to the cylindrical MR gap then is prevalent and, assuming α to be constant with respect to $\Delta\omega$, can be expressed as

$$T_c(\Delta\omega, \Theta) = T(\Delta\omega, \Theta) - \alpha T_c(\Delta\omega, 20°\text{C}) \tag{7.8}$$

The average shear stress in the cylindrical portion of the meatus $\bar{\tau}(\Delta\omega, \Theta)$ can finally be computed as

$$\bar{\tau}(\Delta\omega, \Theta) = \frac{T_c(\Delta\omega, \Theta)}{2\pi L R_m^2} \tag{7.9}$$

where L and R_m are the length and the mean radius of the cylindrical gap, respectively.

The average value of the shear stress on the cylindrical gap is plotted in Fig. 7.12 as a function of $\Delta\omega$ and Θ. Concerning the dependence on temperature, considering all data shown in the right graph of Fig. 7.12, an average rate of -0.12kPa/°C was obtained. This trend can not be

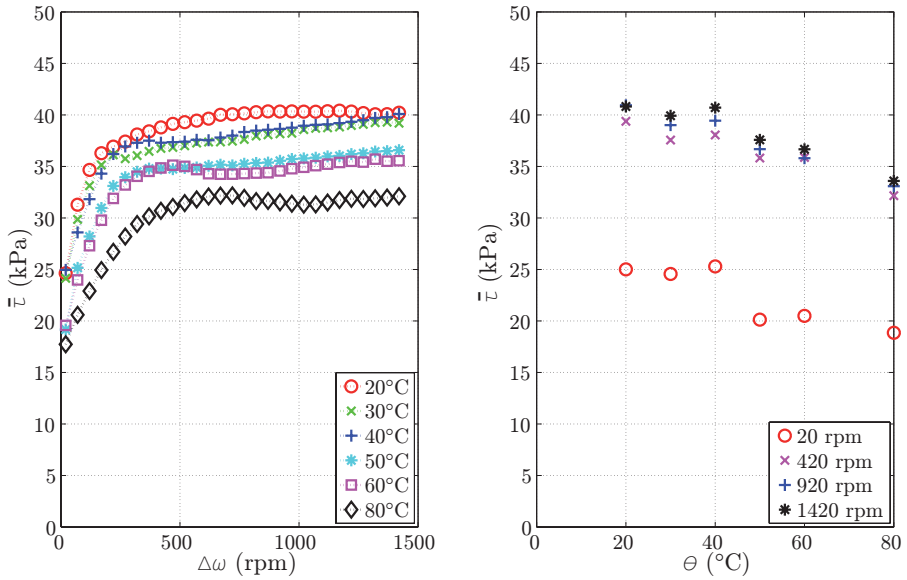

Figure 7.12: Estimated average stress in the cylindrical gap function of relative speed and temperature.

considered as a precise estimation of the dependence of the fluid shear stress on temperature, due to both the simplifying hypotheses made and the non uniform distribution of τ_0 along the cylindrical gap as shown in Fig. 7.11. However, it may be usefully employed to estimate the performance of similar MR devices at different temperatures.

Chapter 8

A MR clutch model based on neural networks

In this chapter, starting from the experimental characterization of the first MR clutch prototype, an accurate model of the device is proposed, based on the use of neural networks.

The aim of the model was to predict the clutch behavior in different operating conditions. Indeed, during normal operation the proposed device is capable of assuring an operation without clutch slip. During particularly severe transients, i.e. relatively high resistant torque due to oil accumulation in the pump, clutch slip could occur leading to energy dissipation in the MR fluid (and hence temperature increase). For this reason, in order to assure the operation of the vacuum pump in every condition, it is necessary to have a model which describes the transmissible torque with high accuracy, taking into consideration several operating and environmental factors. Such model could be implemented in on-board systems, which may predict the torque transmitted by the clutch without requiring additional sensors (e.g. thermocouples), either in real or hardware in the loop environments.

Recently, phenomenological models based on computational intelligence were proposed to describe the behavior of many complex systems. In particular, concerning MR devices, many studies, mainly focused on control strategies of active or semi-active shock absorbers in vehicle [93, 94] and civil [95, 96] applications, were carried out. In this chapter an alternative application of neural network to MR devices, i.e. aimed at their characterization, is proposed. A huge set of experimental data

obtained in different tests, was used to train a feedforward neural network, with one hidden layer, to determine the clutch torque model. The most significant parameters were considered as inputs in a feedforward neural network with one hidden layer, getting as output the torque transmitted by the clutch.

8.1 Experimental data set

During the whole experimental activity, many tests in many different operative conditions were carried out on the first clutch prototype. The acquired data represent an important database on the clutch torque. In particular, concerning the engaged condition, the torque characteristic proved to be dependent on the rest time of the MR fluid, the energy dissipated by slip, and the rate of relative rotational speed. In order to verify these contributions, six different test protocols were used. In all the protocols, the speed of the primary shaft ω^I was controlled, whereas the secondary shaft was kept fixed. The reference speed profiles are shown in Fig. 8.1, where for the sake of concision, ω^I is replaced by ω:

a) the speed ω rises from 0 to the maximum speed (1500 rpm) at constant rate; the test lasts about 20 s and, once the maximum speed is reached, the acquisition is interrupted; this test protocol was the first and simplest choice to characterize the clutch;

b) the speed ω rises from 0 to the maximum speed (1500 rpm) following a power law; once the maximum speed is reached the acquisition is interrupted; this speed profile was chosen to obtain slowly increasing speed profiles at low shaft speed, to better identify the yield torque;

c) the speed ω rises from 0 to the maximum speed (1500 rpm) at constant rate and then is kept constant for about 60 s; this speed profile was chosen to acquire the torque profile in presence of extended slip;

d) the speed ω rises from 0 to the maximum speed (1500 rpm) at constant rate and, once the peak is reached, it starts decreasing with the same absolute rate;

e) the speed ω rises from 0 to the maximum speed (1500 rpm) at constant rate, then is kept constant for about 10 s and, finally, it decreases with the same absolute rate;

f) the speed ω rises from 0 to the maximum speed (in the range 500–1500 rpm) at constant rate, then it decreases with the same absolute rate; the resulting triangular speed profile was repeated three times.

The speed profiles c), d), e) and f) combine both the continuous slip and the speed ramp profile. The rest time between two consecutive tests randomly varied in the range 5 to 60 minutes.

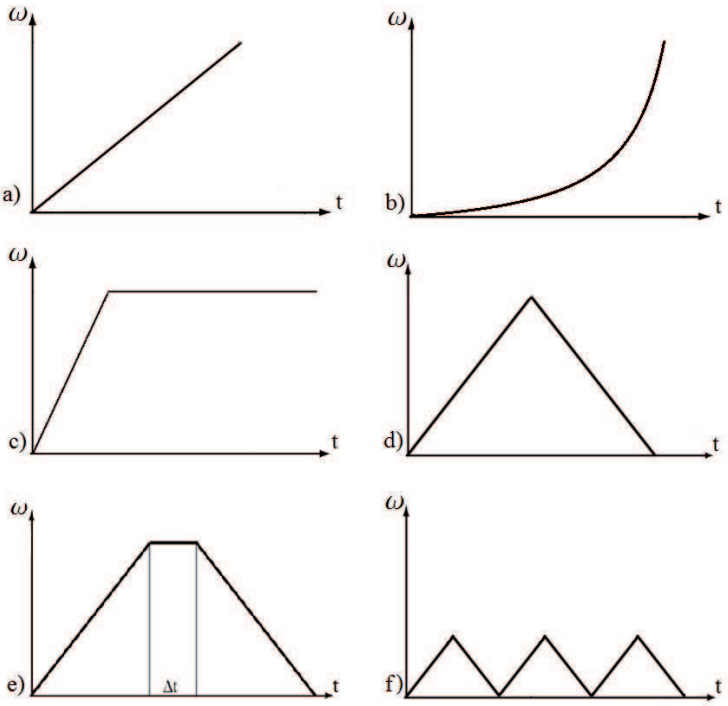

Figure 8.1: Speed profiles

Typical acquired torque characteristics, corresponding to the input speed profiles, are shown in Fig. 8.2. The plots show how the transmitted torque is not only function of the relative speed ω but it depends also on other factors.

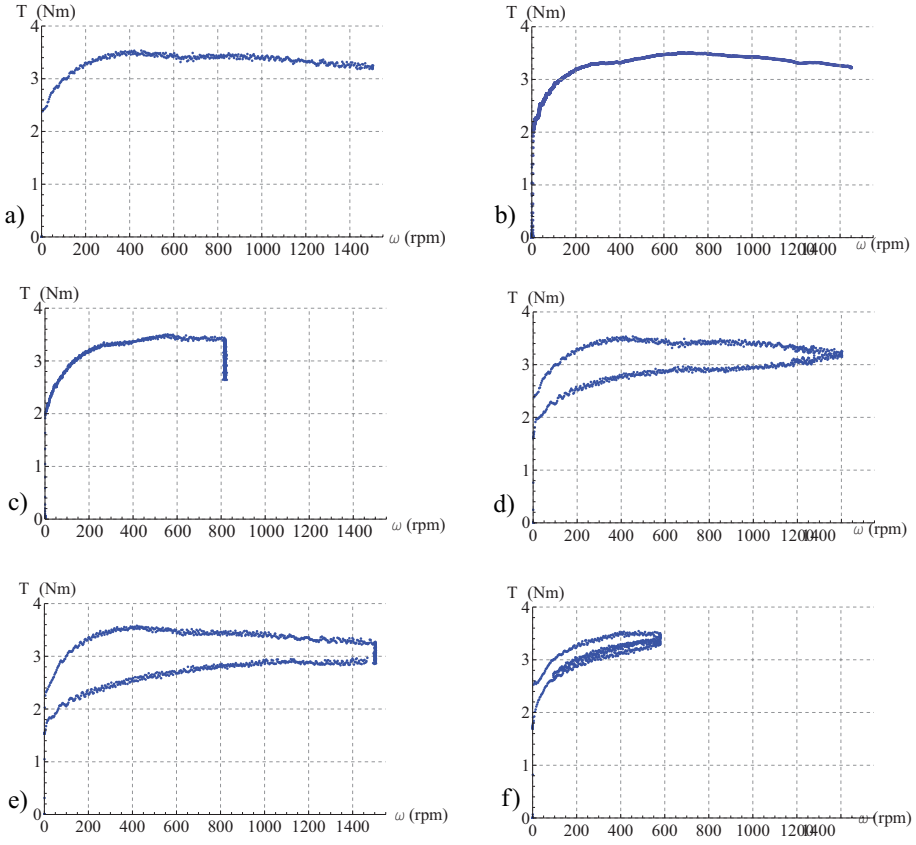

Figure 8.2: Torque profiles

In particular, with reference to each of the above described speed profiles, it results that:

a) the torque presents a yield value of about 2 Nm and then increases up to an almost constant value beyond 500 rpm;

b) the torque profile is similar to the previous one but a lower torque at low speed was measured;

c) keeping the clutch rotating at constant speed produces clutch heating and reduction of the transmitted torque;

d) the torque measured during the decreasing speed phase is not

overlaying the one acquired during the increasing one and a sort of hysteresis is observed;

e) if the speed profile is a combination of the c) and d) speed profiles, the torque presents either a decrease at constant speed or a different path between the increasing and decreasing speed paths.

f) the torque measured during consecutive cycles decreases mostly during the first decreasing phase and then does not vary much.

In addition, a dependence on the rest-time was found, resulting in an increase of torque at low speed for longer rest time.

An analytical model able to describe the torque characteristic was too difficult to implement, due to the many parameters and to the different speed profiles adopted. For this reason a neural network appeared an easier and convenient way to model the clutch characteristic.

8.2 Neural network analysis

A feedforward neural network with a hidden layer [97] was chosen to model the acquired data (Fig. 8.3). The whole data set included 23 output files obtained from as many different tests. In particular, 2 tests were carried out following the constant rate profile of Fig. 8.1a, 2 following the power-law profile of Fig. 8.1b, 7 tests following the profile of Fig. 8.1c, 2 tests following the profile of Fig. 8.1d, 5 tests following the profile of Fig. 8.1e and 5 tests following the procedure of Fig. 8.1f. The test data were acquired at 20 Hz and a total set of about 38000 samples was considered.

On the basis of the different torque characteristics (Fig. 8.2), for each sample (i), in addition to the acquired data (t_i, ω_i and T_i), three more parameters were considered:

1. r_i, the rest time between two consecutive tests was recorded; this parameter is the same for all the samples belonging to the same test;

2. W_i, the energy dissipated due to clutch slip, computed as follows

$$W_i = \sum_{0}^{t_i} T_i \, \omega_i \, \Delta t \quad ; \tag{8.1}$$

the energy dissipated is related to the device temperature and, in a real application, it is easier to be measured than the temperature of the MR fluid. The energy values computed for the data set do not exceed 15 kJ for the tests conducted following profiles a), b), d), e) and f) and 30 kJ for the ones conducted following speed profile c);

3. $\dot{\omega}_i$, the time derivative of the primary speed computed as follows

$$\dot{\omega}_i = \frac{\omega_{i+1} - \omega_i}{\Delta t} \quad . \tag{8.2}$$

which is in the range 0 to 100 rpm/s.

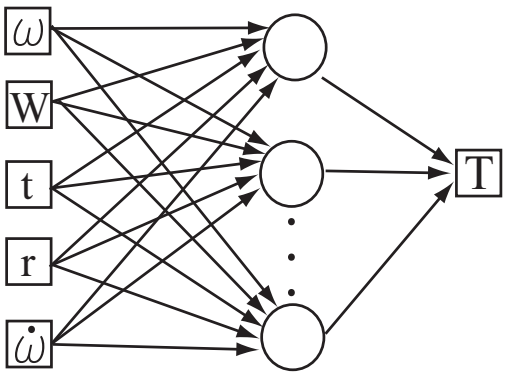

Figure 8.3: Neural network

In order to obtain a model of the MR clutch, the parameters ω, W, t, r and $\dot{\omega}$ were considered as inputs whereas the torque T was the output (Eq. 8.3)

$$T = T(\Delta\omega, t, r, W, \Delta\dot{\omega}) \tag{8.3}$$

The *MatLab Neural Network Toolbox* was used to generate the neural network. Four different hidden layer architectures were considered, having from 3 to 6 neurons in the hidden layer. The data set was automatically separated in training, validation and test sets. The best architecture proved to be the one having 4 neurons in the hidden layer, according to the empirical law which gives the number of neurons in the hidden layer (n_H) starting from the number of inputs (n_I) and outputs (n_O).

$$n_H = \frac{2}{3}(n_I + n_O) = 4 \tag{8.4}$$

The regression analysis, which compares the target output results with the one obtained by the neural network, confirmed the goodness of the chosen architecture; in particular the index of the goodness of fit, R, resulted higher than 0.99 for the training, validation and test sets (Fig. 8.4).

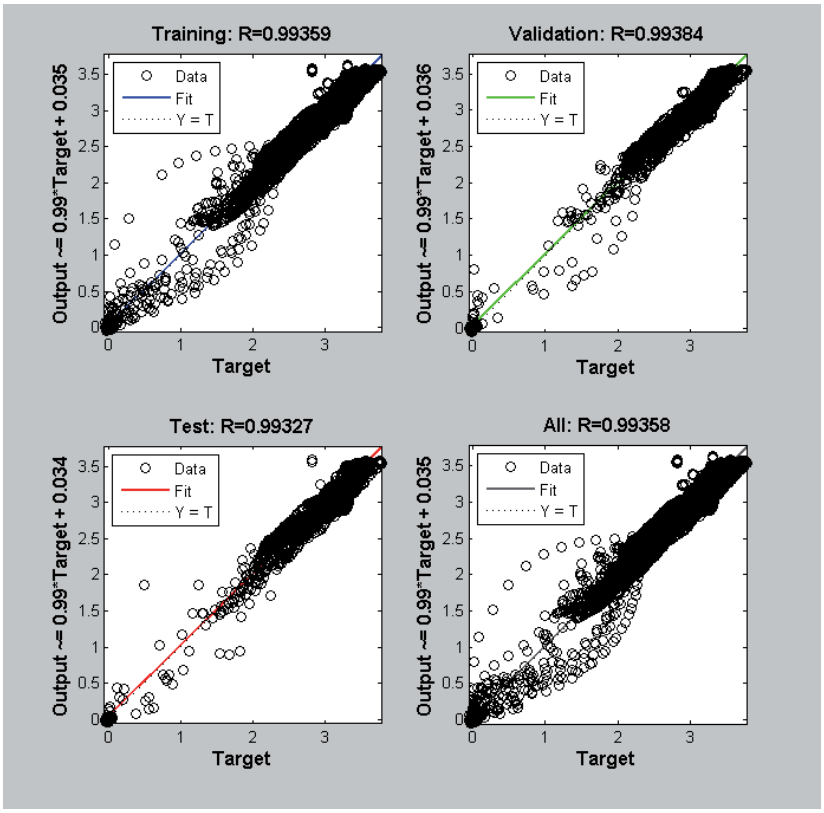

Figure 8.4: Regression analysis

Results

In order to validate the obtained neural network, the results acquired during some experimental tests were compared to the ones obtained by the neural network in Fig. 8.5–8.8. The neural network inputs were chosen within the whole test data set, picking four sample test histories obtained following different speed profiles. At each time step the acquired values t_i, ω_i, r_i and the resulting values W_i and $\dot{\omega}_i$, computed on the basis of Eq. 8.1 and Eq. 8.2, were supplied to the network, which calculated the corresponding output torque T_i.

The rising part of the speed ramp was rightly predicted by the neural network, as well as the torque loss at constant speed which occurs either for speed profile c) or e). Also the decreasing part of the ramp was well followed by the neural network, either if the inversion of the speed slope was instantaneous (profile d)) or if it occurred after a constant speed phase (profile e)).

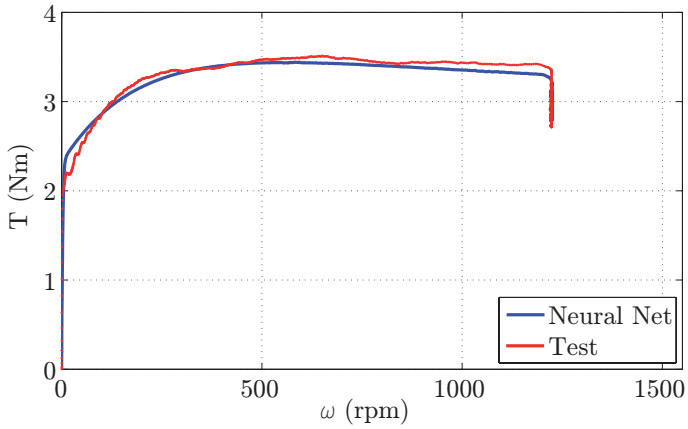

Figure 8.5: Torque results - Speed profile c)

On the contrary the agreement between the experimental and the neural network data results less accurate if speed profile f) is considered. In particular, the first rising and decreasing part were fairly estimated, whereas less agreement was found during the following cycles.

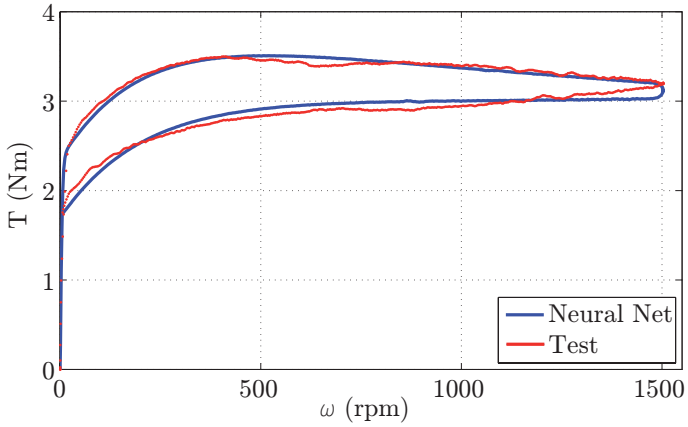

Figure 8.6: Torque results - Speed profile d)

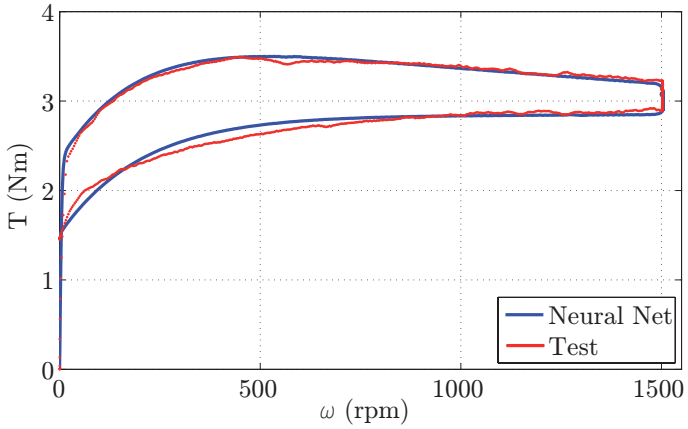

Figure 8.7: Torque results - Speed profile e)

Sensitivity analysis

Besides the validation process, the neural network can be used in order to predict the clutch behavior for quite different working cycles from the ones imposed during the network training. As a preliminary application, in order to highlight the influence of the various parameters, a sensitivity analysis of the torque vs speed characteristic was performed, modifying the parameters one at time (i.e. dissipated energy, rest time, speed slope)

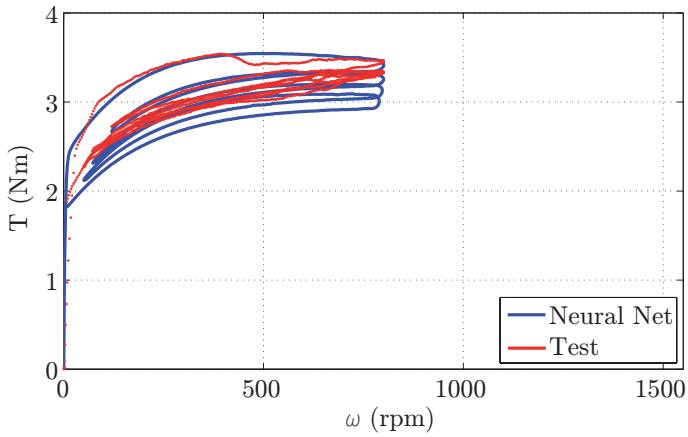

Figure 8.8: Torque results - Speed profile f)

within ranges explored in previous test campaigns.

In order to evaluate the influence of the dissipated energy, four different input sets I_j^W were built corresponding to four different energy values W_j in the range 0 to 15000 J. For each set j, an input matrix was built, whose rows, at each step i, were composed by the following elements:

$$I_{j,i}^W = [\omega_i \quad t_i \quad r \quad W_j \quad \dot{\omega}_i] \tag{8.5}$$

where ω_i, t_i and $\dot{\omega}_i$ were computed at each step so as to describe a constant slope speed profile. The rest time r was assumed to be 20 minutes for all sets. Figure 8.9 shows the torque characteristic corresponding to the different energy values.

The energy turned out to be the most important factor in determining changes in the torque vs slip characteristic. In particular as the dissipated energy rises, the transmitted torque decreases at either low or high speed values. This dependence explains the loss in torque which occurred at constant speed following speed profile c) and the lower values of the torque in the decreasing phase of speed profiles d) and e). It has to be considered that the energy dissipation leads to the increase of the device temperature, which can not be measured in the real application, which does not envisage any temperature sensor. In Chapter 7 the influence of temperature was investigated by a temperature measurement system finding a loss of torque as the temperature rises.

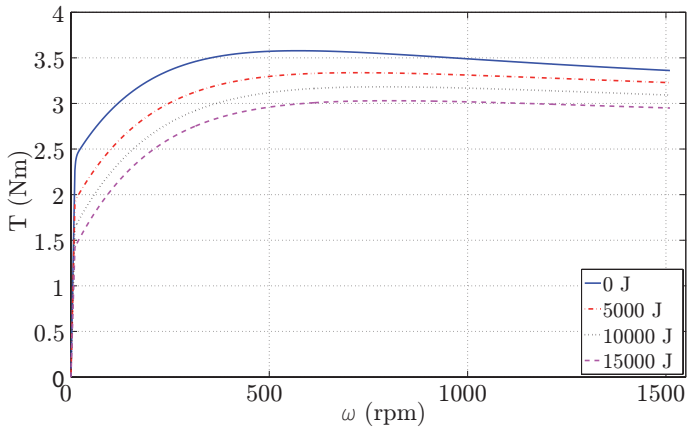

Figure 8.9: Torque results for different dissipated energy values

Similarly, the influence of rest time was considered imposing four different input sets I_j^r, whose rows are composed of

$$I_{j,i}^r = [\omega_i \quad t_i \quad r_j \quad W_i \quad \dot{\omega}_i] \tag{8.6}$$

where ω_i, t_i and $\dot{\omega}_i$ were computed so as to describe a constant slope speed profile, four different values of the rest time were considered in the range 0 to 60 minutes and the dissipated energy W_i was computed iteratively as

$$W_i = W_{i-1} + \omega_{i-1} T_{i-1} \Delta t \tag{8.7}$$

where the time interval Δt is known on the basis of the assigned speed profile. Figure 8.10 shows the torque characteristic corresponding to the different rest time values.

The rest time proved to affect the torque characteristic for low speed values (about 500 rpm), highlighting an increase of torque for increasing rest times. On the contrary, on the basis of neural network results, the rest time does not affect the torque characteristic at yield and at high speed values.

Finally, the influence of the speed ramp was considered, computing four different input sets $I_j^{\dot{\omega}}$, whose rows are composed of

$$I_{j,i}^{\dot{\omega}} = [\omega_{j,i} \quad t_{j,i} \quad r_i \quad W_i \quad \dot{\omega}_j] \tag{8.8}$$

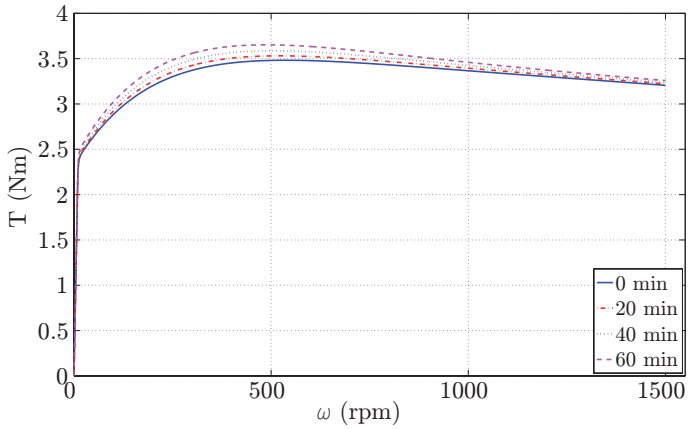

Figure 8.10: Torque results for different rest time values

where four different constant slope speed profiles were computed considering rates $\dot{\omega}_j$ in the range 0 to 75 rpm/s. Figure 8.11 shows the torque characteristic corresponding to the different speed rates. The speed slope, as well as the rest time, affects the torque characteristic to a lesser extent, highlighting a torque increase as the speed slope rises.

Neural network model application: simulation of clutch engagement

In order to simulate the clutch-system behavior, the vacuum pump reference torque characteristic shown in Fig. 8.12 was considered, which refers to the power-brake vacuum chamber emptying, starting from atmospheric pressure down to 0.2 bar. The torque characteristic is function of both the elapsed time and the vacuum pump shaft speed, which corresponds to the speed of the clutch secondary shaft ω^{II}.

The clutch engagement was simulated considering an initial cam-shaft speed, corresponding to the speed of the primary shaft of the clutch ω^{I}, of 1500 rpm and the vacuum pump fixed. The system dynamics equilibrium during engagement was numerically solved according to Eq. 8.9

$$\omega^{II}(i+1) = \omega^{II}(i) + \frac{\Delta t}{J}\left(T(i) - T_d(\omega^{II}(i), t(i))\right) \tag{8.9}$$

where $T(i)$ was computed by the neural network on the basis of Eq. 8.3,

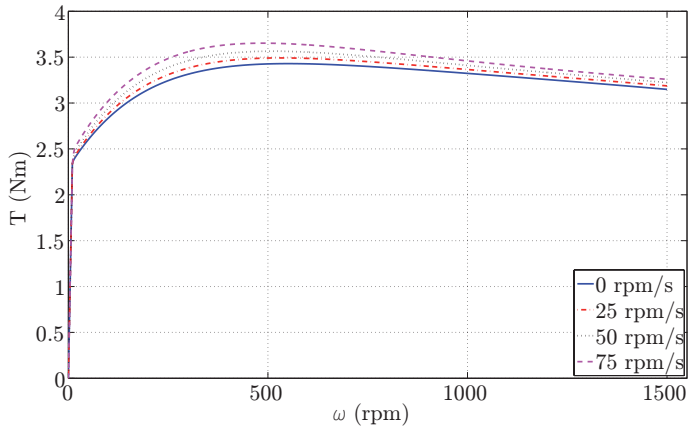

Figure 8.11: Torque results for different speed slope values

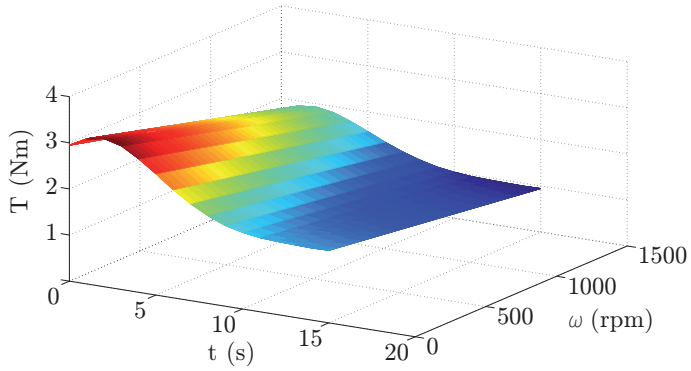

Figure 8.12: Vacuum pump torque characteristic during the emptying phase

assuming $\omega = \omega^I - \omega^{II}$, the rest time was set to 0 minutes and the other parameters computed as stated in Eq. 8.1 and 8.2. The vacuum pump torque $T_d(\omega^{II}(i), t(i))$ was defined on the basis of the diagram shown in Fig. 8.12. The time step Δt was 0.001 s and the moment of inertia of the pump and of the secondary clutch shaft 2×10^{-4} kgm^2.

Figures 8.13 and 8.14 show the results of the simulation. The clutch slips for about 0.04 s and then engages fixedly. The torque of the clutch results higher than the vacuum pump torque during the whole slipping

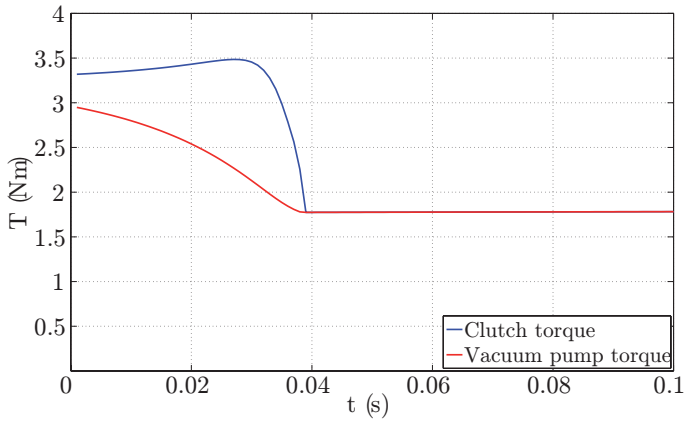

Figure 8.13: Clutch and vacuum pump torque profiles

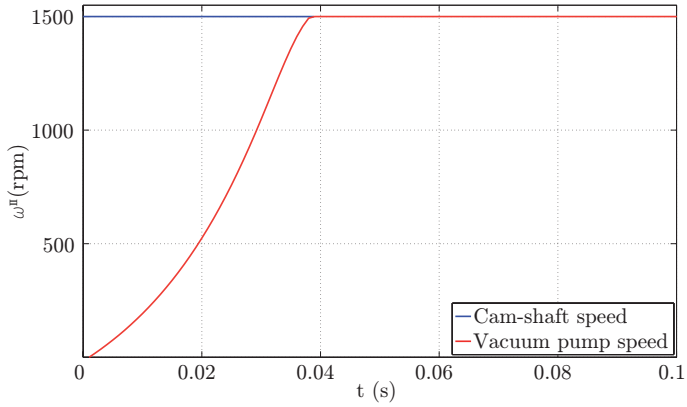

Figure 8.14: Clutch and vacuum pump speed profiles

phase, guaranteeing the clutch engagement. Once the vacuum pump absorbed torque is less than the clutch yield torque, synchronous operation starts without slip and energy loss.

The simulation showed the capability of the neural network of modeling the clutch torque characteristic and confirmed the feasibility of the MR clutch-vacuum pump system both with regard to the reference emptying phase, during which slip occurs, and to the steady phase, during which the system runs synchronously.

The so developed neural network will also be useful in subsequent analyses, in which other transients and heavy duty cycles will be considered (e.g. starting after the accumulation of oil in the vacuum pump, which may cause long-lasting slip).

Chapter 9

The SMA-MR mechanical coupling

The activity described in this final chapter was carried out mainly during the PhD research period abroad which was spent at the *Dynamic and Smart Systems Laboratory* of the University of Toledo, OH (USA), supervised by prof. M. Elahinia.

The activity carried out during the visiting period was aimed at learning the fundamental properties of the most used smart materials, the shape memory alloys (SMA). In particular, in agreement with the laboratory director, it was planned to design and test a simple device, based on SMA, which could be coupled with the already developed MR clutch.

9.1 Background of the activity

Shape memory alloys present unique properties in terms of their stress-strain characteristic, allowing large deformations and shape recovery [98]. In particular, SMAs present two different phases, austenite (parent) and martensite, and the transformation occurs near the room temperature. The transformation between the two phases does not occur due to diffusion but rather by lattice distortion under the effect of shear stress. In addition, the martensite phase has two variants: twinned and detwinned. Starting from twinned martensite, by increasing the deviatoric stress, it is possible to get permanent, even non-plastic, deformation (maximum recoverable deformation about 5%), which can be recovered by heating the part until

the alloy temperature is above the austenite finish temperature. Once the transformation is completed, the initial shape is recovered (shape memory effect, SME) and, by cooling, the direct transformation from austenite to martensite occurs. An additional property of SMA, which was not of interest in this work, is the superelastic effect which is commonly exploited in biomedical applications.

As previously discussed, considering the first clutch prototype described in Chapter 3, in particular operating conditions, e.g. at low environmental temperature, the torque required to start-up the device may be greater than the maximum torque that can be transmitted by the clutch. For this reason, in order not to oversize the clutch and not to increase the power loss due to viscosity, the feasibility of an external device, assembled to the clutch, was conceived to be engaged in response to ambient temperature below 20°C.

The device proposed in this chapter is a sliding spline sleeve actuated by two SMA springs, counteracting two traditional springs. When the temperature nearby the vehicle engine is below 20°C, namely at each engine start-up, the SMA springs are in the martensite phase and the counteracting traditional springs push the sleeve in the engaged position. Once the start-up is completed, in few minutes, the SMA springs warm-up and turn to the austenite phase and recover the parent shape, disengaging the sliding spline sleeve, allowing the clutch to be engaged and disengaged on the basis of the magnet position.

In the literature, SMA springs are used as actuators [99, 100] due to their capability of recovering large, non plastic deformation. On the contrary, few papers have been presented until now which combine the use of MRF and SMA in the same device [101, 102, 103, 104, 105]. In this thesis the sizing and modeling of the SMA springs are presented, considering the modified Brinson model [106, 107]. Simulations were performed considering also the effect of the counteracting springs and a mock-up of the sliding spline sleeve device was developed, to experimentally measure the sleeve displacement due to temperature change.

9.2 The MR-SMA clutch device

9.2.1 The SMA actuation concept

In order to be able to transmit a higher torque by-passing the magnetorheological characteristic, a sliding spline sleeve (no. 6, Fig. 9.1) was

conceived to be assembled coaxially with the clutch secondary group, which can engage the spline shaft (no.5, Fig. 9.1) which is fixed to the clutch primary shaft. The engagement actuation is provided by two pairs of counteracting springs: two traditional compression springs and two SMA tension springs.

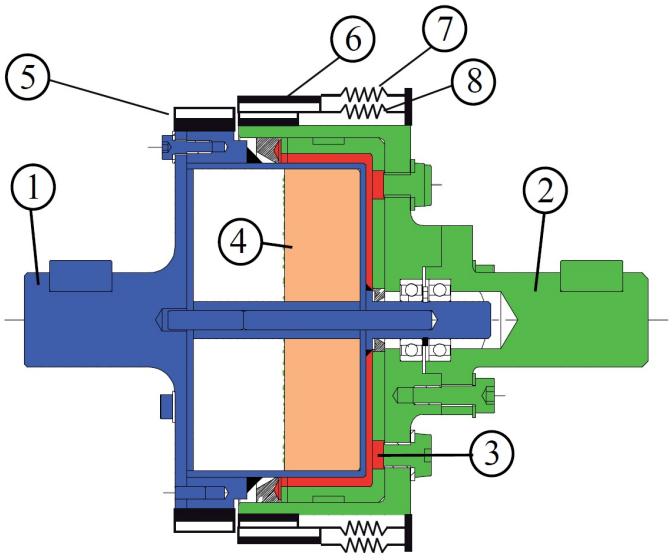

Figure 9.1: System design and MR clutch prototype

The system behavior, as a function of temperature, can be understood considering the SMA phase diagram, proposed by Chung, [107] shown in Fig. 9.2, which represents the phase state in terms of equivalent tension σ and temperature T. The values of M_s, M_f, A_s and A_f represent the martensite and austenite start and finish temperatures, when the material is not subjected to any stress. These values are obtained from literature as reference values for shape memory effect NiTiNol. The solid lines in Fig. 9.2 show the variation of the transformation temperatures under the effect of the applied stress. Finally, the values of detwinning martensite start and finish tension, σ_s and σ_f, were determined by tensile test on the SMA wire.

When the temperature is below the M_f value, the SMA is in the detwinned martensite phase (point A, region 0), under the load of the bias springs, and the SMA spring will be elongated (Fig. 9.3a), engaging the system. The spring will maintain its shape until the austenite start

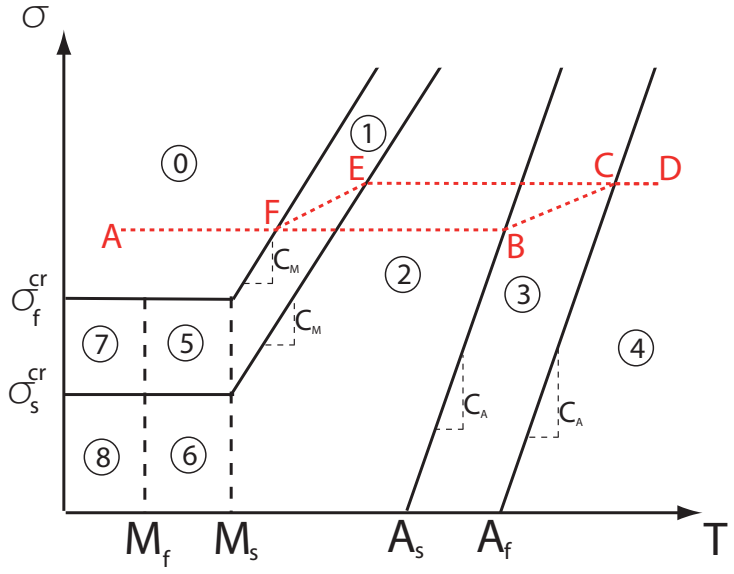

Figure 9.2: SMA phase diagram.

boundary is reached (point B, region 2). If the temperature further increases, the inverse transformation (martensite to austenite) occurs (point B to point C, region 3) and the spring goes back to the parent phase (point D, region 4), compressing the traditional spring (Fig. 9.3b), and increasing the value of the equivalent tension in the wire. Once the inverse transformation is complete, the sliding spline sleeve is disengaged. If the temperature decreases, the direct transformation (austenite to martensite) occurs (point E to point F, region 1), the SMA spring will elongate under the effect of the bias spring load, and the initial sliding spline sleeve will be re-engaged.

The total displacement Δ of the sleeve is the difference between the spring elongation in the martensite and austenite phases.

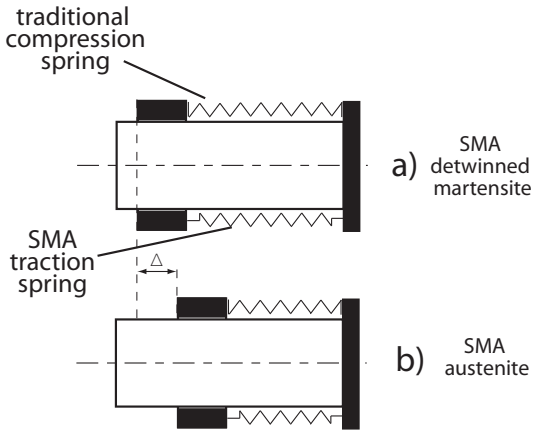

Figure 9.3: Spring elongation in austenite and martensite phases.

9.3 SMA actuation model

9.3.1 SMA constitutive model

To simulate the response of the system, the Brinson model, [106] subsequently modified by Chung, was assumed to determine the martensite volume fraction ζ, considering it as the sum of the stress induced martensite (or detwinned martensite), volume fraction ζ_S and the temperature induced martensite (or twinned martensite) volume fraction ζ_T. A thorough analysis of several SMA models was presented in previous papers, [108, 109] which points out the models limitations and proposes an enhanced model to be used when both stress and temperature vary simultaneously.

With reference to Fig. 9.2, ζ_S and ζ_T can be computed on the basis of the values of σ and T, which determine the material state and the region it belongs to. The transition from one region to another is computed if the volume fractions ζ_{S0} and ζ_{T0} are known.

Region 0 : Pure stress induced martensite

$$\zeta_S = 1 \tag{9.1}$$

$$\zeta_T = 0 \tag{9.2}$$

Region 1 : Transformation from austenite or twinned martensite to detwinned martensite

$$\zeta_S = \frac{1-\zeta_{S0}}{2}\cos\left[\frac{\pi}{\sigma_s^{cr}-\sigma_f^{cr}}\left(\sigma-\sigma_f^{cr}-C_M(T-M_s)\right)\right]+\frac{1+\zeta_{S0}}{2} \tag{9.3}$$

$$\zeta_T = \zeta_{T0}-\frac{\zeta_{T0}}{1-\zeta_{S0}}\left(\zeta_S-\zeta_{S0}\right) \tag{9.4}$$

Region 2 : Mixture of twinned and detwinned martensite and austenite, depending on the loading/temperature history; no transformation occurs in this area

$$\zeta_S = \zeta_{S0} \tag{9.5}$$

$$\zeta_T = \zeta_{T0} \tag{9.6}$$

Region 3 : Transformation from martensite to austenite

$$\zeta = \frac{\zeta_0}{2}\left[\cos\left(a_A\left(T-A_s-\frac{\sigma}{C_A}\right)\right)+1\right] \tag{9.7}$$

$$\zeta_S = \zeta_S 0-\frac{\zeta_{S0}}{\zeta_0}\left(\zeta_0-\zeta\right) \tag{9.8}$$

$$\zeta_T = \zeta_T 0-\frac{\zeta_{T0}}{\zeta_0}\left(\zeta_0-\zeta\right) \tag{9.9}$$

Region 4 : Pure austenite, no transformation

$$\zeta_S = 0 \tag{9.10}$$

$$\zeta_T = 0 \tag{9.11}$$

Region 5 : Transformation from austenite or twinned martensite to detwinned martensite; transformation from austenite to twinned martensite

$$\zeta_S = \frac{1-\zeta_{S0}}{2}\cos\left[\frac{\pi}{\sigma_s^{cr}-\sigma_f^{cr}}\left(\sigma-\sigma_f^{cr}\right)\right]+\frac{1+\zeta_{S0}}{2} \tag{9.12}$$

$$\zeta_T = \Delta_{T\zeta}-\frac{\Delta_{T\zeta}}{1-\zeta_{S0}}(\zeta_S-\zeta_{S0}) \tag{9.13}$$

where, if $T < T_0$

$$\Delta_{T\zeta} = \frac{1-\zeta_{S0}-\zeta_{T0}}{2}\cos\left[\frac{\pi}{M_s - M_f}(T - M_f)\right] + \frac{1-\zeta_{S0}+\zeta_{T0}}{2} \tag{9.14}$$

otherwise

$$\Delta_{T\zeta} = \zeta_{T0} \tag{9.15}$$

Region 6 : Transformation from austenite to twinned martensite

$$\zeta_S = \zeta_{S0} \tag{9.16}$$

$$\zeta_T = \frac{1-\zeta_0}{2}\cos\left[a_M\left(T - M_f\right)\right] + \frac{1+\zeta_0}{2} - \zeta_{S0} \tag{9.17}$$

Region 7 : Transformation from twinned martensite to detwinned martensite

$$\zeta_S = \frac{1-\zeta_{S0}}{2}\cos\left[\frac{\pi}{\sigma_s^{cr} - \sigma_f^{cr}}\left(\sigma - \sigma_f^{cr}\right)\right] + \frac{1+\zeta_{S0}}{2} \tag{9.18}$$

$$\zeta_T = \zeta_{T0} - \frac{\zeta_{T0}}{1-\zeta_{S0}}(\zeta_S - \zeta_{S0}) \tag{9.19}$$

Region 8 : Twinned and detwinned martensite are present, depending on the loading-temperature history; no transformation occurs.

$$\zeta_S = \zeta_{S0} \tag{9.20}$$

$$\zeta_T = \zeta_{T0} \tag{9.21}$$

Once the volume fractions are known, the equivalent deformation ε can be computed, neglecting the thermal deformation, considering the SMA constitutive equation

$$\varepsilon = \frac{\sigma - \Omega_S\left(\zeta_S - \zeta_{S0}\right)}{E} \tag{9.22}$$

where E is the Young's modulus and Ω_S is a function of E and of the maximum detwinning strain ε_L

$$\Omega_S = -E\varepsilon_L \tag{9.23}$$

The Young's modulus is defined starting from the martensite E_M and austenite E_A Young's moduli and the martensite fraction ζ as follows

$$E = E_A + (E_A - E_M)\zeta \tag{9.24}$$

9.3.2 Actuation dynamics and evaluation of the SMA spring force

The dynamic equation of the sliding spline sleeve is obtained considering the longitudinal motion of the sleeve, subjected to the forces shown in Fig. 9.4 where F_S is the compression spring force, F_{SMA} is the force

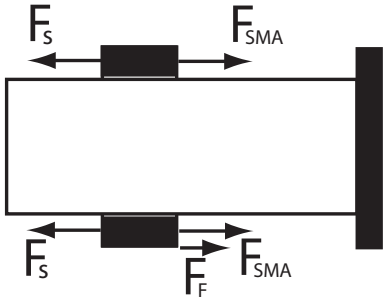

Figure 9.4: Longitudinal force diagram of the sliding spline sleeve.

exerted by the SMA spring and F_F is the friction force. The dynamic equation is

$$m\ddot{\delta} = 2F_S(\delta) - 2F_{SMA}(\delta, \zeta) - F_F(\dot{\delta}) \tag{9.25}$$

in which m is the sleeve mass and ζ is the martensite volume fraction, related to temperature and stress, according to the SMA constitutive model. In case of biaxial or multi-axial stress state the von Mises equivalent stress can be used in the constitutive model in place of the normal stress component [110].

The spring force F_S is due to the elastic deformation of the conventional spring, given by

$$F_S = -k_S(\delta_S - \delta_{S,0}) \tag{9.26}$$

where $\delta_{S,0}$ is the free-load spring length, δ_S is the actual spring length and k_S is the spring stiffness which can be computed as follows

$$k_S = \frac{Gd^4}{8D^3N} \tag{9.27}$$

The SMA spring force is computed assuming the spring wire to be subjected only to torsion, neglecting curvature and pitch effect. The

shear wire deformation is assumed linear (Fig. 9.5), according to the rigid in-plane rotation of the wire cross-sections, and its maximum value γ_M can be related to the elongation δ_{SMA} by

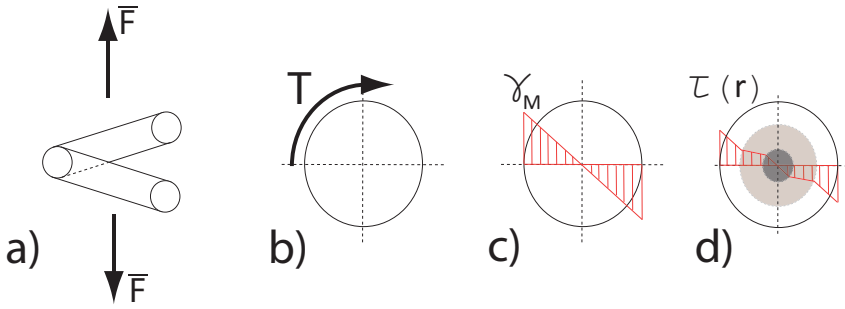

Figure 9.5: SMA spring. a) spring loading diagram; b) wire cross section loading; c) wire deformation; d) example of stress distribution

$$\gamma_M = (\delta_{SMA} - \delta_{SMA,0}) \frac{d_{SMA}}{\pi N_{SMA} D_{SMA}^2} \tag{9.28}$$

where $\delta_{SMA,0}$ is the free-load SMA spring length, δ_{SMA} is the actual SMA spring length, whereas d_{SMA}, D_{SMA} and N_{SMA} are the wire diameter, the average spring diameter and the number of active coils respectively.

According to the SMA constitutive model, the stress distribution is piecewise linear, with different slopes for different states, e.g. Fig. 9.5d. In the internal area only twinned martensite is present and the shear stress is linear. In the middle area, both twinned and detwinned martensite appear, and the shear stress distribution is almost constant, due the SMA capability of absorbing shear deformation through lattice distortion (detwinning effect). In the external area, only the detwinned martensite is present and the shear stress is linear.

The Eq. 9.22 can be written also with reference to shear stress and shear deformation as [111]

$$\tau(r) = G\alpha r + \sqrt{3}\varepsilon_L (\zeta_S - \zeta_{S0}) \tag{9.29}$$

where α is the rate of shear deformation along the wire radius, which can be related to the spring deformation through Eq. 9.28, and the shear

modulus G depends on the volume fraction ζ as given by the following:

$$G = G_A + (G_A - G_M)\zeta = \frac{1}{2(1+\nu)}(E_A + (E_A - E_M)\zeta) \tag{9.30}$$

Considering that the volume fraction is a function of temperature and stress, it follows that previous Eq. 9.29 is an implicit equation, which can be solved by an iterative procedure to obtain the shear stress distribution in the wire cross section.

A piecewise constant distribution was assumed considering k annular regions to compute the shear stress profile.

The force F_{SMA} exploited by the spring can be computed follows

$$F_{SMA} = \sum_{i=1}^{k} \frac{4\pi\tau(r_k^3 - r_{k-1}^3)}{3D_{SMA}} \tag{9.31}$$

For the dynamic analysis the following procedure was then developed: starting from the dynamic equilibrium the deformation of the spring is obtained at each time-step; on the basis of the spring deformation, a linear shear deformation of the spring wire is determined on the basis of Eq. 9.28; the shear stress distribution is obtained, solving the Eq. 9.29; the SMA spring force is then computed (Eq. 9.31) and used for the equilibrium equation in the next time-step.

9.4 Material characterization

A thermally straightened, oxide free, 1 mm diameter NiTiNol wire, supplied by Memry - SAES Group, was used to manufacture the SMA springs.

In order to get the martensite start and finish tension values, a tensile test was performed at room temperature. Starting from the raw supplied wire, a straight clip of about 60 mm length was heat treated at 410°C for 15 minutes and then quenched in water, as described in the paper [112]. Subsequently, the wire was tested with an electric tensile machine (Fig. 9.6), controlling the displacement by imposing a constant speed of 0.008 mm/s. The wire was grasped by two grips to prevent wire slippage. The upper grip was fixed to the moving plate by a spherical washer; the lower one was fixed in the same way to a load cell which measured the force. The displacement ΔL was acquired by the tensile machine.

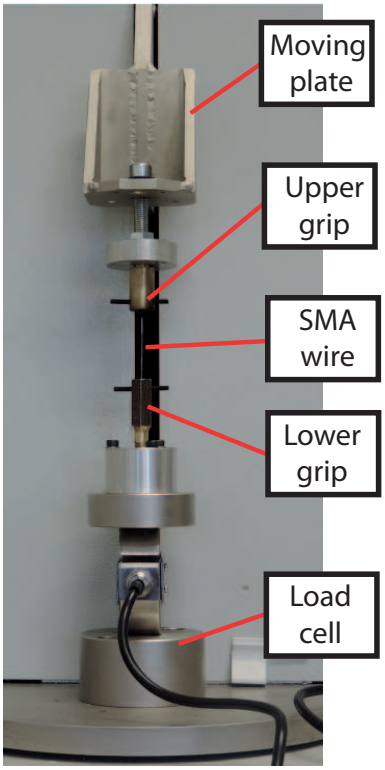

Figure 9.6: Tensile test rig

The rig was calibrated to adjust the measured displacement, removing the effect of the deformation of the rig parts, in order to acquire the net wire elongation ΔL. The wire deformation ε was computed as the ratio between the net wire elongation and the initial length of the wire. In Fig. 9.7 the stress vs strain acquired profile is shown, by which it is possible to get the following material characteristics:

σ_S : tensile stress at which the martensite detwinning starts

σ_F : tensile stress at which the martensite detwinning finishes

E_M : martensite Young's modulus

The values of the parameters obtained from the tensile test are listed in

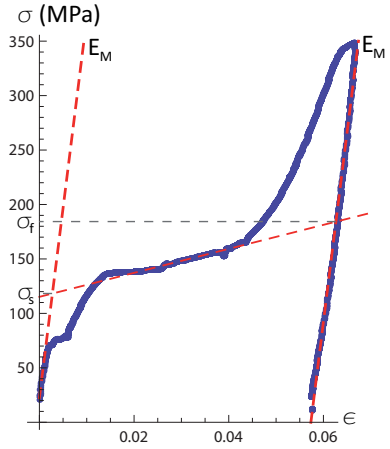

Figure 9.7: Stress-strain characteristic

Tab. 9.1, together with the transformation temperature usually considered for the shape memory effect NiTiNol.

E_A	70 GPa	M_s	55 °C
E_M	35 GPa	M_f	15 °C
ε_L	0.06	A_s	70 °C
ν	0.3	A_f	79 °C
σ_s	118 MPa	C_M	6 MPa/°C
σ_f	184 MPa	C_A	6 MPa/°C

Table 9.1: Material constants of the NiTiNol wire.

9.5 Simulation and experimental test

In order to validate the model, in terms of sleeve position as a function of the environmental temperature, two SMA springs were manufactured and a dummy plain sleeve prototype was built, without any spline sleeve.

9.5.1 Spring manufacturing and experimental rig

The SMA springs were manufactured manually, starting from the straight wire, and then heat treated. A dedicated mandrel (Fig. 9.8) was built starting from a steel rod. Along the rod, a longitudinal slot was machined, to fit the straight spring tips, coaxially to the rod. A fixed spacer was used to bend the first spring coil and a moving one to bend the last spring coil. By means of the moving spacer, the space available for the coils can vary. The moving spacer has a radial groove, to let the wire pass and fit it along the rod lot, below the nut. The wire was wrapped fixing the rod

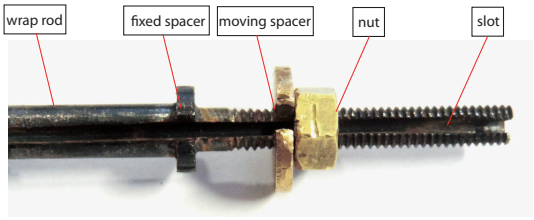

Figure 9.8: Wrapping rig

in the lathe spindle and keeping the wire in tension on the lathe carriage, which moves forward 1 mm for each spindle turn (Fig. 9.9). Once the spring wrapping process was done, the whole system was subjected to a heat treatment at 410°C for 15 minutes and then quenched in water. The spring was then removed axially from the wrapper after untightening the nut and the spacer. The final result is shown in Fig. 9.10. The sliding system, schematically depicted in Fig. 9.3, was built as shown in Fig. 9.11.

Two diametrically opposed SMA springs and two diametrically opposed traditional springs were connected to a fixed base and to a sleeve, which can move coaxially with a cylindrical rail. The device was put into a caulk oven, where the environmental temperature can be controlled by a temperature control unit (TCU) which acquires the temperature measured by a thermocouple and regulates the power supply to the oven. The displacement of the sliding sleeve was measured by a potentiometer.

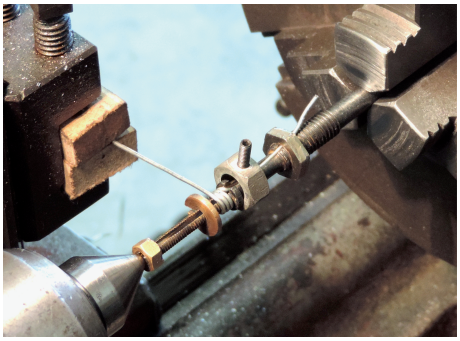

Figure 9.9: Wrapping procedure

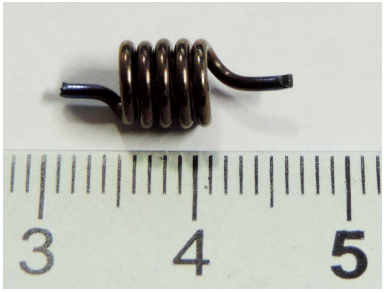

Figure 9.10: SMA spring

9.5.2 Simulation and experimental results

The dynamic model of the sleeve was implemented in MatLab Simulink and Eq. 9.25 was solved numerically. The initial configuration of the sliding sleeve is shown in Fig. 9.13, where the SMA and conventional springs measures respectively $\delta_{SMA,i}$ and $\delta_{S,i}$ (Tab. 9.2) and the sliding sleeve is in contact with the base. The sleeve displacement δ is related to the SMA and conventional spring lengths by the following equations

$$\delta_S = \delta + \delta_{S,i} \tag{9.32}$$

$$\delta_{SMA} = \delta + \delta_{SMA,i} \tag{9.33}$$

The springs parameters are listed in Tab. 9.2 and the SMA material

Figure 9.11: Sliding sleeve dummy system

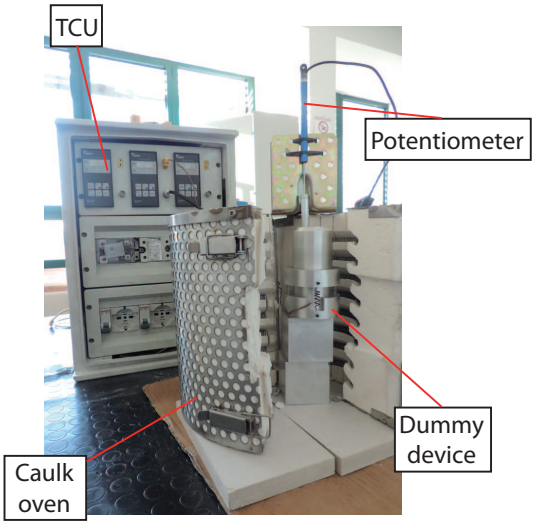

Figure 9.12: Experimental test bench

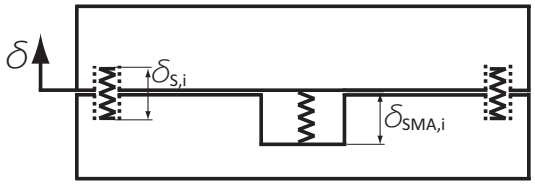

Figure 9.13: Initial configuration of the simulated device

properties in Tab. 9.1.

Traditional spring		**SMA spring**	
d	0.75 mm	d_{SMA}	1 mm
D	5.35 mm	D_{SMA}	5 mm
N	16	N_{SMA}	5 mm
k_s	1.28 N/mm		
$\delta_{S,0}$	39 mm	$\delta_{SMA,0}$	15 mm
$\delta_{S,i}$	23 mm	$\delta_{SMA,i}$	15 mm

Table 9.2: Springs characteristics.

The temperature profile was imposed as user input: starting from 120°C the temperature was decreased down to 0°C at a constant rate of 5°C/s, and then increased again up to 140°C with the same rate.

The sleeve displacement resulting from the simulation is shown in Fig. 9.14 as a function of the temperature.

Figure 9.15 presents the plots of shear stress as function of the radius r in the cross section of the wire at two different temperatures, obtained by simulation. At 120°C only austenite is present and the stress distribution is linear. At 20°C, two different states (i.e. twinned martensite, twinned and detwinned martensite) are present, as shown in Fig. 9.16 and reflected by the two different slopes of the stress function, with a prevalence of the second state and a quite lower slope of the stress function.

The sliding sleeve dummy system shown in Fig. 9.11 was tested in two different configurations, at 120°C and 20°C respectively. The sleeve position for both the temperature values is shown in Fig. 9.17.

The total sleeve displacement between the two configurations is about 8 mm, which is very close to the one predicted by simulation.

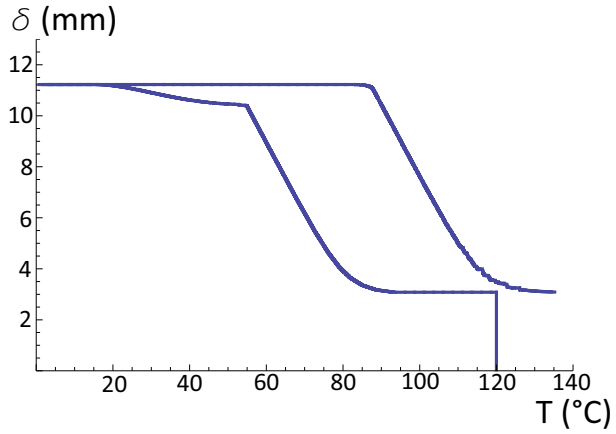

Figure 9.14: Sleeve displacement versus temperature

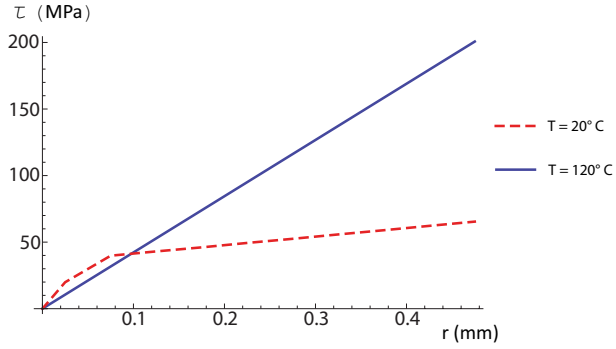

Figure 9.15: Shear stress distribution in the cross section of the wire at different temperatures

9.6 Conclusions on the SMA-MR device

In this activity unique properties of shape memory alloys and magnetorheological fluids were combined. A mechanical coupling, actuated by SMA, was conceived and developed considering an MR clutch which was previously developed by the authors as a possible application. The coupling is engaged by two different pairs of springs, i.e. two conventional

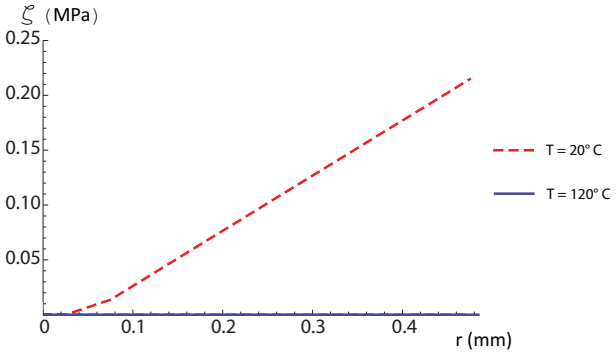

Figure 9.16: Stress induced martensite distribution in the cross section of the wire at different temperatures

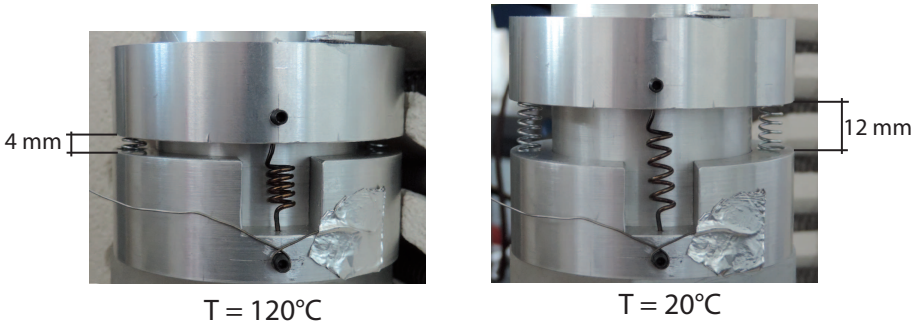

Figure 9.17: Sliding sleeve position for different temperature values

and two SMA springs, which were dimensioned considering the clutch geometry, the displacement requirements and the constitutive properties of the SMA.

A prototype of the actuated coupling was then built and tested in the temperature range 20–120°C. The comparison between the model and the experimentally obtained positions of the sleeve at the extreme temperatures appeared in fairly good agreement.

The tests performed on the dummy system proved the feasibility of the employment of SMA to extend the operating range of a passive MRF

clutch. The resulting system magnet-thermo-mechanical is a passive clutch. The engagement/disengagement mechanism responds to both variation of environment temperature as well as variation of magnetic field strength. Magnetic field strength changes according to the axial position of the permanent magnet. This clutch provides two main functions without the need for a source of power or electronics. The clutch provides timely engagement for auxiliary units to an internal combustion engine. In cold start up temperatures the device is engaged by SMA actuators, as the engine warms up this mode of actuation ends and the second mode starts. In the second mode only the magnetic actuation takes place in response to the requirements of the auxiliary unit.

Chapter 10

Conclusions

During the PhD course, the research focused mainly on the modeling, design and experimentation of smart devices for the enhancement of vehicles efficiency. The activities can be ideally split in three branches:

- MR clutch development in the framework of the funded project;
- further research activity on the MR clutch prototype;
- research on SMA based device.

MR clutch development in the framework of the funded project. In the first phase several prototypes of MR clutch were designed and manufactured, in the framework of a funded project which involved the Department of Civil and Industrial Engineering (DICI), the Department of Energy and Systems Engineering (DESTEC) of the University of Pisa and Pierburg Pump Technology. The clutch prototypes were aimed at disengaging engine auxiliaries (i.e. vacuum pump) when their operation is not needed.

Starting from simple geometries inspired by an extensive literature review, the first prototype was conceived by a multidisciplinary team, whose capabilities included both mechanical and magnetic design. The author of this dissertation mainly dealt with the definition of the concept geometries, the feasibility studies, the mechanical design, including the simulation of the rheological behavior of the fluid, and drove the whole experimental campaign and results analysis. Mechanical and magnetic finite element simulation were carried out and a feasibility analysis led to the final design and realization of the first prototype (Chapter 3). An

experimental test bench was developed and the prototype was preliminary characterized (Chapter 4). Then two additional prototypes, based on the first prototype geometry but with different dimensions were built and tested, giving rise to experimental comparison (Chapter 5) which led to the definition of two new performance indices which can be used to compare different MR clutches.

In order to fulfill the project final specification and to settle some drawbacks found in the experimentation of the first prototype series, a new prototype, which was able to satisfy all the design specifications and to accomplish the project goals, was designed and built.

The funded activity gave rise to four European patents and one world patents.

Together with Pierburg Pump Technology - Stabilimento di Livorno, an assessment of the reduction of power consumption due to vacuum pump actuation was performed [8] on the basis of the NEDC cycle (see Chapter 1). In Fig. 10.1 the comparison between the power absorbed during the urban and extra-urban phases of the NEDC cycle are shown for the current production vacuum pump and the innovative vacuum pump coupled with the use of MR clutch, both developed during the funded project. The filled area highlights when the MR clutch can be disengaged.

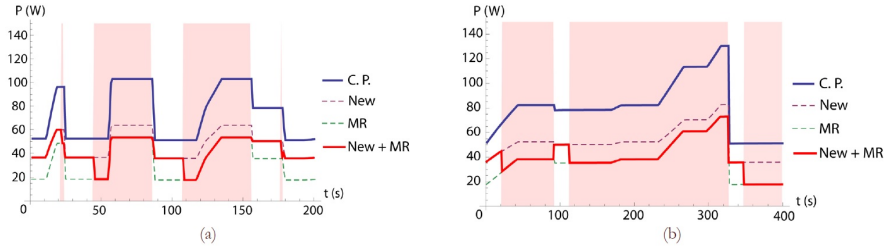

Figure 10.1: Power absorption comparison during the NEDC driving cycle - a) urban b) extra-urban

In Tab. 10.1 and Tab. 10.2 the energy consumption comparison of different vacuum pumps, eventually equipped with the MR clutch, is proposed.

As expected, the innovative vacuum pump benefits are evident especially during the urban cycle, where the vacuum pump is often engaged,

System	Urban (kJ)	Extra-urban (kJ)	Total (kJ)
Current production VP	14.6	32.5	90.9
Innovative VP	9.5	20.9	58.9
Current production VP + MR clutch	10.4	17.5	59.1
Innovative VP + MR clutch	8.2	16.2	49.0

Table 10.1: Energy absorption during the NEDC driving cycle

System	Urban (%)	Extra-urban (%)	Total (%)
Innovative VP	35.0	35.7	35.3
Current production VP + MR clutch	28.8	46.1	35.1
Innovative VP + MR clutch	43.7	50.3	46.0

Table 10.2: Energy absorption comparison during the NEDC driving cycle

whereas the MR clutch benefits come out especially during the extra-urban cycle when braking maneuvers are infrequent and the vacuum pump can be disengaged for long periods.

Further research activities on the MR clutch prototype. Once the research aimed at fulfilling the project goals was done, some additional analyses were carried out on the first prototype, which was used as a testing device. In particular, the effect of temperature was satisfactorily assessed, starting from experimental measurements, by the use of a model which took into account both the MR and the temperature effect and allowed to obtain the torque characteristic of the prototype as a surface $T(\Theta, \Delta\omega)$.

Finally, the torque characteristic of the first prototype was modeled by means of neural networks, taking into account the effect of several parameters. In particular, the dependence of the torque on the dissipated energy, which is related to the clutch self-heating came out strongly. Also the effect of the rest time between the clutch operation, due to the thixotropic effect of the MR fluid proved to be not negligible.

Research on SMA carried out during the PhD period abroad. Three months of the PhD were spent at the *Dynamic and Smart Systems Laboratory* of the University of Toledo, OH (USA), supervised by prof. M. Elahinia.

During this period an enhancement of the MR clutch was proposed, making use of SMA springs. In particular, a SMA actuated sliding spline

sleeve was designed, modeled and tested under the effect of temperature and spring loads.

The comparison between the mathematical model and the experimental results was good, confirming the feasibility of the device and the accuracy of the model.

Appendix

MRF-122EG Magneto-Rheological Fluid

Description

LORD MRF-122EG fluid is a hydrocarbon-based magneto-rheological (MR) fluid formulated for general use in controllable, energy-dissipating applications such as shocks, dampers and brakes.

MRF-122EG fluid is a suspension of micron-sized, magnetizable particles in a carrier fluid. When exposed to a magnetic field, the rheology of MRF-122EG fluid reversibly and instantaneously changes from a free-flowing liquid to a semi-solid with controllable yield strength. Altering the strength of the applied magnetic field precisely and proportionally controls the consistency or yield strength of the fluid.

MRF-122EG fluid can be used in *valve mode* (fluid flowing through an orifice) or in *shear mode* (fluid shearing between two surfaces). In the absence of a magnetic field, MRF-122EG fluid flows freely or allows free movement. Upon application of a magnetic field, the fluid's particles align with the direction of the field in chain-like fashion, thereby restricting the fluid's movement within the gap in proportion to the strength of the magnetic field.

Features and Benefits

Fast Response Time – responds instantly and reversibly to changes in a magnetic field.

Dynamic Yield Strength – provides high yield strength in the presence of a magnetic field and very low yield strength in the absence of a magnetic field; allows for a wide range of controllability.

Temperature Resistant – performs consistently throughout a broad temperature range, meeting the requirements of demanding applications such as automotive shock absorbers.

Hard Settling Resistant – provides high resistance to hard settling; easily redispersed.

Non-Abrasive – formulated to not abrade the devices in which the MR fluid is used.

Application

For more information on MR technology, refer to the MR Design Guides located on www.lord.com/mr.

Mixing – Under common flow conditions, no separation is observed between particles and the carrier fluid. However, a degree of separation may eventually occur under static conditions. If needed, use a paint shaker to redisperse the particles into a homogeneous state prior to use.

Storage

Keep container tightly closed when not in use.

Typical Properties*

Appearance	Dark Gray Liquid
Viscosity, Pa-s @ 40°C (104°F) Calculated as slope 500-800 sec^{-1}	0.042 ± 0.020
Density	
g/cm^3	2.28-2.48
(lb/gal)	(19.0-20.7)
Solids Content by Weight, %	72
Flash Point, °C (°F)	>150 (>302)
Operating Temperature, °C (°F)	-40 to +130 (-40 to +266)

*Data is typical and not to be used for specification purposes.

LORD
AskUsHow™

Cautionary Information

Before using this or any LORD product, refer to the Material Safety Data Sheet (MSDS) and label for safe use and handling instructions.

For industrial/commercial use only. Not to be used in household applications. Not for consumer use.

Yield Stress vs. Magnetic Field Strength

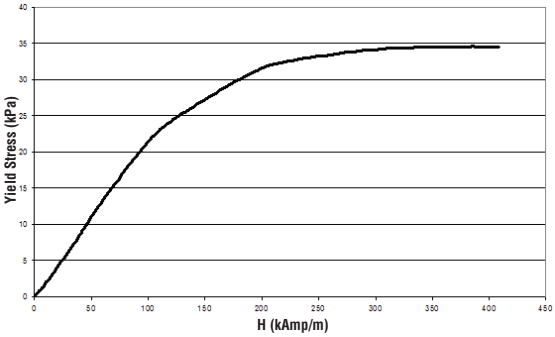

Shear Stress as a function of Shear Rate with no Magnetic Field applied at 40°C (104°F)

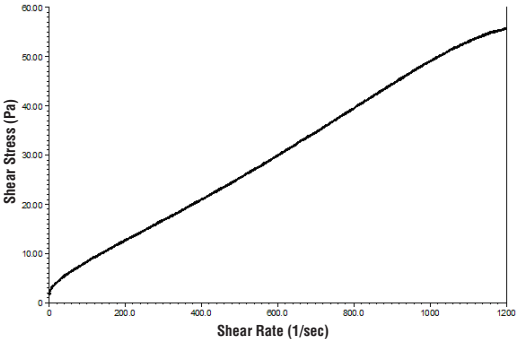

Typical Magnetic Properties

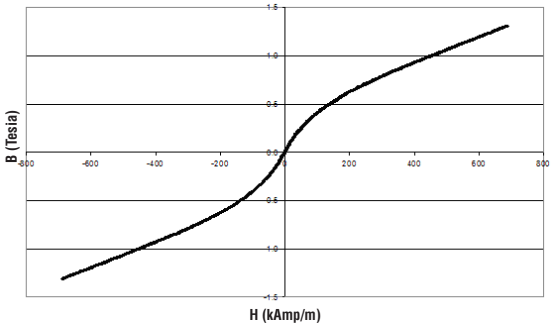

Values stated in this technical data sheet represent typical values as not all tests are run on each lot of material produced. For formalized product specifications for specific product end uses, contact the Customer Support Center.

Information provided herein is based upon tests believed to be reliable. In as much as LORD Corporation has no control over the manner in which others may use this information, it does not guarantee the results to be obtained. In addition, LORD Corporation does not guarantee the performance of the product or the results obtained from the use of the product or this information where the product has been repackaged by any third party, including but not limited to any product end-user. Nor does the company make any express or implied warranty of merchantability or fitness for a particular purpose concerning the effects or results of such use.

LORD provides valuable expertise in adhesives and coatings, vibration and motion control, and magnetically responsive technologies. Our people work in collaboration with our customers to help them increase the value of their products. Innovative and responsive in an ever-changing marketplace, we are focused on providing solutions for our customers worldwide . . . Ask Us How.

LORD Corporation
World Headquarters
111 Lord Drive
Cary, NC 27511-7923
USA

Customer Support Center (in United States & Canada)
+1 877 ASK LORD (275 5673)

www.lord.com

LORD Ask Us How™

MRF-132DG Magneto-Rheological Fluid

Description

LORD MRF-132DG fluid is a hydrocarbon-based magneto-rheological (MR) fluid formulated for general use in controllable, energy-dissipating applications such as shocks, dampers and brakes.

MRF-132DG fluid is a suspension of micron-sized, magnetizable particles in a carrier fluid. When exposed to a magnetic field, the rheology of MRF-132DG fluid reversibly and instantaneously changes from a free-flowing liquid to a semi-solid with controllable yield strength. Altering the strength of the applied magnetic field precisely and proportionally controls the consistency or yield strength of the fluid.

MRF-132DG fluid can be used in *valve mode* (fluid flowing through an orifice) or in *shear mode* (fluid shearing between two surfaces). In the absence of a magnetic field, MRF-132DG fluid flows freely or allows free movement. Upon application of a magnetic field, the fluid's particles align with the direction of the field in chain-like fashion, thereby restricting the fluid's movement within the gap in proportion to the strength of the magnetic field.

Features and Benefits

Fast Response Time – responds instantly and reversibly to changes in a magnetic field.

Dynamic Yield Strength – provides high yield strength in the presence of a magnetic field and very low yield strength in the absence of a magnetic field; allows for a wide range of controllability.

Temperature Resistant – performs consistently throughout a broad temperature range, meeting the requirements of demanding applications such as automotive shock absorbers.

Hard Settling Resistant – provides high resistance to hard settling; easily redispersed.

Non-Abrasive – formulated to not abrade the devices in which the MR fluid is used.

Application

Mixing – Under common flow conditions, no separation is observed between particles and the carrier fluid. However, a degree of separation may eventually occur under static conditions. If needed, use a paint shaker to redisperse the particles into a homogeneous state prior to use.

Storage

Keep container tightly closed when not in use.

Typical Properties*

Appearance	Dark Gray Liquid
Viscosity, Pa-s @ 40°C (104°F) Calculated as slope 800-1200 sec^{-1}	0.112 ± 0.02
Density	
g/cm^3	2.95-3.15
(lb/gal)	(24.6-26.3)
Solids Content by Weight, %	80.98
Flash Point, °C (°F)	>150 (>302)
Operating Temperature, °C (°F)	-40 to +130 (-40 to +266)

*Data is typical and not to be used for specification purposes.

LORD
AskUsHow™

Cautionary Information

Before using this or any LORD product, refer to the Material Safety Data Sheet (MSDS) and label for safe use and handling instructions.

For industrial/commercial use only. Not to be used in household applications. Not for consumer use.

Shear Stress as a function of Shear Rate with no Magnetic Field applied at 40°C (104°F)

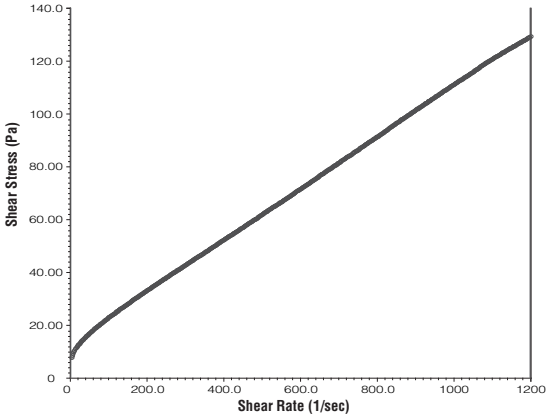

Yield Stress vs. Magnetic Field Strength

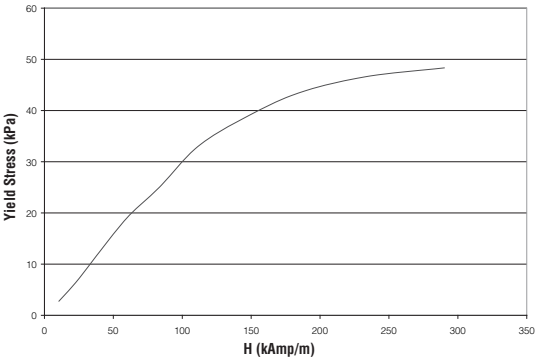

Typical Magnetic Properties

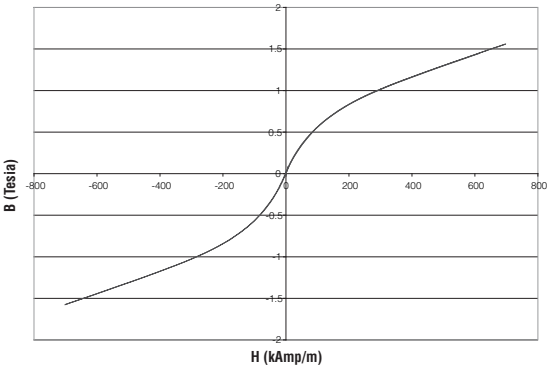

Values stated in this technical data sheet represent typical values as not all tests are run on each lot of material produced. For formalized product specifications for specific product end uses, contact the Customer Support Center.

Information provided herein is based upon tests believed to be reliable. In as much as LORD Corporation has no control over the manner in which others may use this information, it does not guarantee the results to be obtained. In addition, LORD Corporation does not guarantee the performance of the product or the results obtained from the use of the product or this information where the product has been repackaged by any third party, including but not limited to any product end-user. Nor does the company make any express or implied warranty of merchantability or fitness for a particular purpose concerning the effects or results of such use.

LORD provides valuable expertise in adhesives and coatings, vibration and motion control, and magnetically responsive technologies. Our people work in collaboration with our customers to help them increase the value of their products. Innovative and responsive in an ever-changing marketplace, we are focused on providing solutions for our customers worldwide ... Ask Us How.

LORD Corporation
World Headquarters
111 Lord Drive
Cary, NC 27511-7923
USA

Customer Support Center (in United States & Canada)
+1 877 ASK LORD (275 5673)

www.lord.com

For a listing of our worldwide locations, visit LORD.com.

LORD
AskUsHow™

MRF-140CG Magneto-Rheological Fluid

Description

LORD MRF-140CG fluid is a hydrocarbon-based magneto-rheological (MR) fluid formulated for general use in controllable, energy-dissipating applications such as shocks, dampers and brakes.

MRF-140CG fluid is a suspension of micron-sized, magnetizable particles in a carrier fluid. When exposed to a magnetic field, the rheology of MRF-140CG fluid reversibly and instantaneously changes from a free-flowing liquid to a semi-solid with controllable yield strength. Altering the strength of the applied magnetic field precisely and proportionally controls the consistency or yield strength of the fluid.

MRF-140CG fluid can be used in *valve mode* (fluid flowing through an orifice) or in *shear mode* (fluid shearing between two surfaces). In the absence of a magnetic field, MRF-140CG fluid flows freely or allows free movement. Upon application of a magnetic field, the fluid's particles align with the direction of the field in chain-like fashion, thereby restricting the fluid's movement within the gap in proportion to the strength of the magnetic field.

Features and Benefits

Fast Response Time – responds instantly and reversibly to changes in a magnetic field.

Dynamic Yield Strength – provides high yield strength in the presence of a magnetic field and very low yield strength in the absence of a magnetic field; allows for a wide range of controllability.

Temperature Resistant – performs consistently throughout a broad temperature range, meeting the requirements of demanding applications such as automotive shock absorbers.

Hard Settling Resistant – provides high resistance to hard settling; easily redispersed.

Non-Abrasive – formulated to not abrade the devices in which the MR fluid is used.

Application

For more information on MR technology, refer to the MR Design Guides located on www.lord.com/mr.

Mixing – Under common flow conditions, no separation is observed between particles and the carrier fluid. However, a degree of separation may eventually occur under static conditions. If needed, use a paint shaker to redisperse the particles into a homogeneous state prior to use.

Storage

Keep container tightly closed when not in use.

Typical Properties*

Appearance	Dark Gray Liquid
Viscosity, Pa-s @ 40°C (104°F) Calculated as slope 800-1200 sec^{-1}	0.280 ± 0.070
Density	
g/cm^3	3.54-3.74
(lb/gal)	(29.5-31.2)
Solids Content by Weight, %	85.44
Flash Point, °C (°F)	>150 (>302)
Operating Temperature, °C (°F)	-40 to +130 (-40 to +266)

*Data is typical and not to be used for specification purposes.

LORD
AskUsHow™

Cautionary Information

Before using this or any LORD product, refer to the Material Safety Data Sheet (MSDS) and label for safe use and handling instructions.

For industrial/commercial use only. Not to be used in household applications. Not for consumer use.

Shear Stress as a function of Shear Rate with no Magentic Field applied at 40°C (104°F)

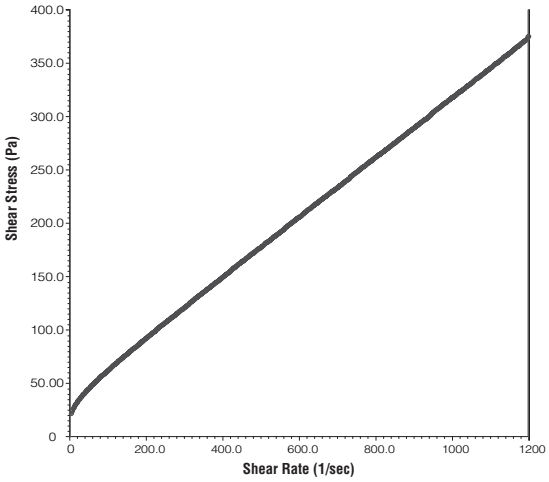

Yield Stress vs. Magnetic Field Strength

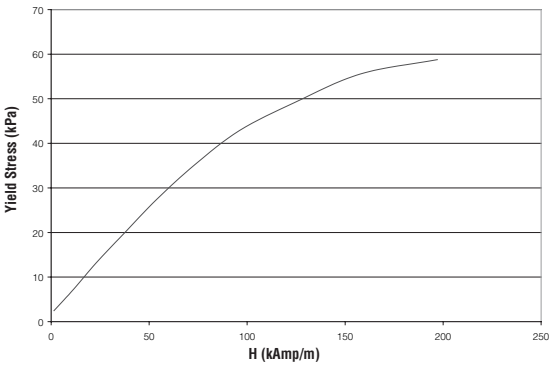

Typical Magnetic Properties

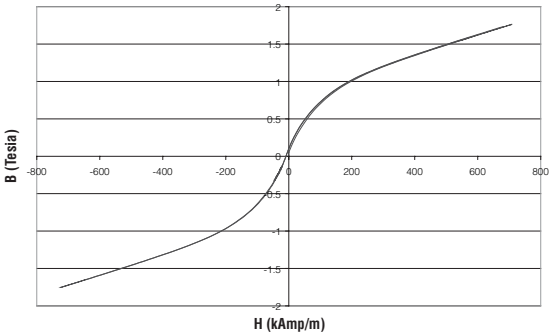

Values stated in this technical data sheet represent typical values as not all tests are run on each lot of material produced. For formalized product specifications for specific product end uses, contact the Customer Support Center.

Information provided herein is based upon tests believed to be reliable. In as much as LORD Corporation has no control over the manner in which others may use this information, it does not guarantee the results to be obtained. In addition, LORD Corporation does not guarantee the performance of the product or the results obtained from the use of the product or this information where the product has been repackaged by any third party, including but not limited to any product end-user. Nor does the company make any express or implied warranty of merchantability or fitness for a particular purpose concerning the effects or results of such use.

LORD provides valuable expertise in adhesives and coatings, vibration and motion control, and magnetically responsive technologies. Our people work in collaboration with our customers to help them increase the value of their products. Innovative and responsive in an ever-changing marketplace, we are focused on providing solutions for our customers worldwide . . . Ask Us How.

LORD Corporation
World Headquarters
111 Lord Drive
Cary, NC 27511-7923
USA

Customer Support Center (in United States & Canada)
+1 877 ASK LORD (275 5673)

www.lord.com

LORD
AskUsHow™

References

[1] F. Bucchi, P. Forte, and F. Frendo. A fail-safe magnetorheological clutch excited by permanent magnets for the disengagement of automotive auxiliaries. *Journal of Intelligent Material Systems and Structures*, 13:1045389X13517313, 2014.

[2] F. Bucchi, P. Forte, and F. Frendo. Experimental characterization of a permanent magnet magnetorheological clutch. In *11th Biennal Conference on Enginnering Systems Design and Analysis*, Nantes, France, 2012.

[3] R. Rizzo, A. Musolino, F. Bucchi, P. Forte, and F. Frendo. Magnetic FEM design and experimental validation of an innovative fail-safe magnetorheological clutch excited by permanent magnets. *IEEE Transactions on Energy Conversion*, in review, 2014.

[4] F. Bucchi, P. Forte, A. Franceschini, and F. Frendo. Analysis of differently sized prototypes of a MR clutch by performance indices. *Smart Materials and Structures*, 22(10):105009, 2013.

[5] F. Bucchi, P. Forte, and F. Frendo. Temperature effect on the torque characteristics of a magnetorheological clutch. *Mechanics of Advanced Materials and Structures*, in press, 2014.

[6] F. Bucchi, P. Forte, and F. Frendo. Analysis of the experimental torque characteristic of a magnetorheological clutch using neural networks. In ASME 2013, editor, *Conference on Smart Materials, Adaptive Structures and Intelligent Systems, SMASIS2013*, Snowbird, Utah, USA, 2013.

[7] F. Bucchi, P. Forte, F. Frendo, and M. Elahinia. A passive magneto-thermo-mechanical coupling actuated by SMA springs and MR

fluid. *International Journal of Structural Stability and Dynamics*, in review, 2014.

[8] F. Bucchi, P. Forte, F. Frendo, and R. Squarcini. A magnetorheological clutch for efficient automotive auxiliary device actuation. *Frattura e Integrita Strutturale*, 23:62–74, 2013.

[9] European vehicle market statistics - pocketbook 2013. Report, 2013.

[10] F. An. Global overview on vehicle fuel economy and emission standards. In *United Nations Headquarters*, New York, 2009.

[11] Global comparison of light-duty vehicle fuel economy/GHG emissions standards. Report, 2013.

[12] KPMG's global automotive executive survey. Report, 2013.

[13] S. B. Choi and Y. M. Han. *Magnetorheological fluid technology - Applications in vehicle systems*. CRC Press, 2013.

[14] J. D. Carlson, D. M. Catanzarite, and K. A. St. Clair. Commercial magneto-rheological fluid devices. *International Journal of Modern Physics B*, 10(23n24):2857–2865, 1996.

[15] D. H. Wang and W. H. Liao. Magnetorheological fluid dampers: a review of parametric modelling. *Smart Materials and Structures*, 20(2):023001, 2011.

[16] Quoc-Hung Nguyen and Seung-Bok Choi. Optimal design of a vehicle magnetorheological damper considering the damping force and dynamic range. *Smart Materials and Structures*, 18(1):015013, 2009.

[17] Q. H. Nguyen and S. B. Choi. Selection of magnetorheological brake types via optimal design considering maximum torque and constrained volume. *Smart Materials and Structures*, 21(1):015012, 2012.

[18] H. J. Song, S. B. Choi, J. H. Kim, and K. S. Kim. Performance evaluation of ER shock damper subjected to impulse excitation. *Journal of Intelligent Material Systems and Structures*, 13(10):625–628, 2002.

[19] G. Marannano, G. Virzì Mariotti, and S. Sagona. Ottimizzazione di un freno a fluido magnetoreologico per uso automobilistico. In *XXXVIII Convegno Nazionale AIAS*, Torino, 2009.

[20] Q. H. Nguyen and S. B. Choi. Optimal design of an automotive magnetorheological brake considering geometric dimensions and zero-field friction heat. *Smart Materials and Structures*, 19(11):115024, 2010.

[21] E. J. Park, D. Stoikov, L. Falcao da Luz, and A. Suleman. A performance evaluation of an automotive magnetorheological brake design with a sliding mode controller. *Mechatronics*, 16(7):405–416, 2006.

[22] K. Karakoc, E. J. Park, and A. Suleman. Design considerations for an automotive magnetorheological brake. *Mechatronics*, 18(8):434–447, 2008.

[23] V. A. Neelakantan. Modeling and reduction of centrifuging in magnetorheological (MR) transmission clutches for automotive applications. *Journal of Intelligent Material Systems and Structures*, 16(9):703–711, 2005.

[24] B. Kavlicoglu, F. Gordaninejad, C. A. Evrensel, A. Fuchs, and G. Korol. A semi-active, high-torque, magnetorheological fluid limited slip differential clutch. *Journal of Vibration and Acoustics*, 128(5):604, 2006.

[25] E. S. Kim, S. B. Choi, Y. G. Park, and S. Lee. Temperature control of an automotive engine cooling system utilizing a magneto-rheological fan clutch. *Smart Materials and Structures*, 19(10):107001, 2010.

[26] J. Rabinow. The magnetic fluid clutch. *AIEE Transactions*, pages 1308–1315, 1948.

[27] J. Rabinow. Magnetic fluid torque and force transmitting device. *US Patent*, 2575360, 1951.

[28] M. R. Jolly, J. W. Bender, and J. D. Carlson. Properties and applications of commercial magnetorheological fluids. In *5th Annual International Symposium on Smart Structures and Materials*, 1998.

[29] N. M. Wereley. *Magnetorheology - Advances and Applications.* RSCPublishing, 2013.

[30] L. R. Rudnick. *Synthetics, mineral oils, and bio-based lubricants: chemistry and technology.* CRC press, 2013.

[31] R. T. Foister. Magnetorheological fluids. *US Patent*, US 005667715A, 1997.

[32] Seval Genc and Pradeep P Phulé. Rheological properties of magnetorheological fluids. *Smart Materials and Structures*, 11(1):140, 2002.

[33] V. R. Iyengar and R. T. Foister. Magnetorheological compositions for use in magnetorheological fluids and method of preparing same. *US Patent*, US006811717 B2, 2004.

[34] H. Shahnazian and S. Odenbach. Yield stress in ferrofluids? *International Journal of Modern Physics B*, 21(28n29):4806–4812, 2007.

[35] J. R. Stokes and J. H. Telford. Measuring the yield behaviour of structured fluids. *Journal of Non-Newtonian Fluid Mechanics*, 124(1-3):137–146, 2004.

[36] P. C. F. Moller, J. Mewis, and D. Bonn. Yield stress and thixotropy: on the difficulty of measuring yield stresses in practice. *Soft Matter*, 2(4):274, 2006.

[37] R. Tao. Super-strong magnetorheological fluids. *Journal of Physics: Condensed Matter*, 13(50):R979, 2001.

[38] A. Spaggiari and E. Dragoni. Effect of pressure on the physical properties of magnetorheological fluids. *Frattura ed Intgrità Strutturale*, 23:75–86, 2013.

[39] X. Wang and F. Gordaninejad. Study of magnetorheological fluids at high shear rates. *Rheologica Acta*, 45(6):899–908, 2006.

[40] Lord Corporation Ltd. http://www.lord.com/products-and-solutions/magneto-rheological-(mr)/mr-products.xml.

[41] BASF. http://www.basf.com.

[42] Liquid Research. http://liquidsresearch.co.uk.

[43] A. G. Olabi and A. Grunwald. Design and application of magneto-rheological fluid. *Materials & Design*, 28(10):2658–2664, 2007.

[44] X. Z. Zhang, X. L. Gong, P. Q. Zhang, and Q. M. Wang. Study on the mechanism of the squeeze-strengthen effect in magnetorheological fluids. *Journal of Applied Physics*, 96(4):2359, 2004.

[45] R. P. Chhabra. *Non-Newtonian fluids: an introduction*, pages 3–34. Springer, 2010.

[46] B. R. Munson, D. F. Young, and T. H. Okiishi. *Fundamentals of Fluid Mechanics*. 2002.

[47] Eugene Cook Bingham. *An investigation of the laws of plastic flow*, volume 13 of *Bulletin of the Bureau of Standards*. Govt. Print. Off., 1917.

[48] Eugene Cook Bingham. *Fluidity and plasticity*, volume 1. McGraw-Hill New York, 1922.

[49] Winslow H Herschel and Ronald Bulkley. Konsistenzmessungen von gummi-benzollosungen. *Kolloid-Zeitschrift*, 39(4):291–300, 1926.

[50] M. Ismail, F. Ikhouane, and J. Rodellar. The hysteresis bouc-wen model, a survey. *Archives of Computational Methods in Engineering*, 16(2):161–188, 2009.

[51] P. Saramito. A new elastoviscoplastic model based on the herschel-bulkley viscoplastic model. *Journal of Non-Newtonian Fluid Mechanics*, 158(1-3):154–161, 2009.

[52] J. D. Carlson. MR fluids and devices in the real world. *International Journal of Modern Physics B*, 19(07n09):1463–1470, 2005.

[53] X. Tang and H. Conrad. An analytical model for magnetorheological fluids. *Journal of Physics D: Applied Physics*, 33(23):3026, 2000.

[54] M. R. Jolly, J. D. Carlson, and B. C. Munoz. A model of the behaviour of magnetorheological materials. *Smart Materials and Structures*, 5:607–614, 1996.

[55] K. I. Jang, J. Seok, B. K . Min, and S. J. Lee. Behavioral model for magnetorheological fluid under a magnetic field using lekner summation method. *Journal of Magnetism and Magnetic Materials*, 321(9):1167–1176, 2009.

[56] K. I. Jang, B. K. Min, and J. Seok. A behavior model of a magnetorheological fluid in direct shear mode. *Journal of Magnetism and Magnetic Materials*, 323(10):1324–1329, 2011.

[57] J. D. Carlson and M. J. C. Raleigh. Magnetorheological fluid dampers. *US Patent*, US5277281, 1994.

[58] H. G. Jung, B. F. Jr. Spencer, Ni Y. Q., and Lee I. W. State-of-the-art of semiactive control systems using MR dampers in civil engineering applications. *Structural Engineering and Mechanics*, 17:493–526, 2004.

[59] S. J. Dyke, B. F. Jr. Spencer, M. K. Sain, and J. D. Carlson. Modeling and control of magnetorheological dampers for seismic response reduction. *Smart Materials and Structures*, 5:565–575, 1996.

[60] N. M. Wereley, J. U. Cho, Y. T. Choi, and S. B. Choi. Magnetorheological dampers in shear mode. *Smart Materials and Structures*, 17(1):015022, 2008.

[61] J. Zapomel, P. Ferfecki, and P. Forte. A computational investigation of the transient response of an unbalanced rigid rotor flexibly supported and damped by short magnetorheological squeeze film dampers. *Smart Materials and Structures*, 21(10):105011, 2012.

[62] B. M. Kavlicoglu, F. Gordaninejad, C. A. Evrensel, N. Cobanoglu, Y. Liu, A. Fuchs, and G. Korol. High-torque magnetorheological fluid clutch. In *SPIE's 9th Annual International Symposium on Smart Structures and Materials*, pages 393–400. International Society for Optics and Photonics, 2002.

[63] W. H. Li and H. Du. Design and experimental evaluation of a magnetorheological brake. *International Journal of Advanced Manufacturing Technology*, 21:508–515, 2003.

[64] S. Gopalswamy, S. M. Linzell, and G. L. Jones. Magnetorheological fluid clutch with minimized reluctance. *US Patent*, US005845752A, 1998.

[65] P. B. Usoro, A. L. Smith, C. K. Kao, M. George, and G. Sommer. Magnetorheological fluid clutch. *US Patent*, US 6318531 B1, 2001.

[66] T. Kikuchi and K. Kobayashi. Development of cylindrical magnetorheological fluid brake for virtual cycling system. In *International conference on robotics and biomimetics*, pages 2547–2552, Phuket, Thailand, 2011.

[67] T. Kikuchi, K. Oda, S. Yamaguchi, and J. Furusho. Leg-robot with MR clutch to realize virtual spastic movements. 21(15):1523, 2010.

[68] Q. H. Nguyen and S. B. Choi. Optimal design of a magnetorheological brake absorber for torsional vibration control. *Smart Materials and Structures*, 21(2):025001, 2012.

[69] Q. H. Nguyen and S. B. Choi. Optimal design of a novel hybrid MR brake for motorcycles considering axial and radial magnetic flux. *Smart Materials and Structures*, 21(5):055003, 2012.

[70] M. Jackel, J. Kloepfer, M. Matthias, and B. Seipel. The novel MRF-ball-clutch design – a MRF-safety-clutch for high torque applications. *Journal of Physics: Conference Series*, 412:012051, 2013.

[71] H. T. Guo and W. H. Liao. A novel multifunctional rotary actuator with magnetorheological fluid. *Smart Materials and Structures*, 21(6):065012, 2012.

[72] D. Wang, Z. Tian, Q. Meng, and Y. Hou. Development of a novel two-layer multiplate magnetorheological clutch for high-power applications. *Smart Materials and Structures*, 22(8):085018, 2013.

[73] G. L. Johnston, W. C. Kruckemeyer, and R. E. Longhouse. Passive magnetorheological clutch. *US Patent*, US005848678A, 1998.

[74] H. Steinwender. Magnetorheological clutch. *US Patent*, US007870939 B2, 2011.

[75] T. Saito and H. Ikeda. Development of normally closed type of magnetorheological clutch and its application to safe torque control system of human-collaborative robot. *Journal of Intelligent Material Systems and Structures*, 18(12):1181–1185, 2007.

[76] H. Bose, T. Gerlach, and J. Ehrlich. Magnetorheological torque transmission devices with permanent magnets. *Journal of Physics: Conference Series*, 412:012050, 2013.

[77] G. Genta and L. Morello. *The Automotive Chassis - vol. 1: Components Design*. Mechanical Engineering Series. Springer, 2009.

[78] E. A. Bansbach. Torque transfer apparatus using magnetorheological fluids. *US Patent*, 5,779,013, 1998.

[79] N. C. Kavlicoglu, B. Kavlicoglu, B. M. Liu, C. A. Evrensel, A. Fuchs, G. Korol, and F. Gordaninejad. Response time and performance of a high-torque magnetorheological fluid limited slip differential clutch. 16:149–159, 2007.

[80] U. Lee, D. Kim, N. Hur, and D. Jeon. Design analysis and experimental evaluation of an MR fluid clutch. *Journal of Intelligent Material Systems and Structures*, 10:701–707, 2000.

[81] J. D. Carlson. Magnetorheological brake with integrated flywheel. *US Patent*, 6,186,290, 2001.

[82] G. Armenio, E. Bartalesi, F. Bucchi, A. Ferri, F. Frendo, P. Forte, R. Rizzo, and R. Squarcini. Mechanical combustion engine driven fluid pump. *EPO Patent*, EP2543903 A1, 2013.

[83] EFFE. Effe v2.00, user manual. *Bathwick Electrical Design ltd*, 2009.

[84] E. Bartalesi, F. Bucchi, and R. Squarcini. Pneumatic brake assistance arrangement. *EPO Patent Pending*, 2014.

[85] P. B. Usoro, A. L. Smith, C. Kao, G. Moser, and G. Sommer. Mathematical model of drum-type MR brakes using herschel-bulkley shear model. *Journal of Intelligent Material Systems and Structures*, 19:565–572, 2008.

[86] A. Chaudhuri. Rheological parameter estimation for a ferrous nanoparticle-based magnetorheological fluid using genetic algorithms. *Journal of Intelligent Material Systems and Structures*, 17(3):261–269, 2006.

[87] S. Genc. Synthesis and properties of magnetorheological (MR) fluids. *University of Pittsburgh, PhD Thesis*, 2002.

[88] F. Zschunke, R. Rivas, and P. O. Brunn. Temperature behavior of magnetorheological fluids. *Applied Rheology*, 15:116–121, 2005.

[89] C. Guerrero-Sanchez, A. Ortiz-Alvarado, and U. S. Schubert. Temperature effect on the magneto-rheological behavior of magnetite particles dispersed in an ionic liquid. *Journal of Physics: Conference Series*, 149:012052, 2009.

[90] C. W. Macosko and R. G. Larson. *Rheology: principles, measurements, and applications*. Wiley-VCH, 1994.

[91] W. Zhang, X. Gong, S. Xuan, and W. Jiang. Temperature-dependent mechanical properties and model of magnetorheological elastomers. *Industrial & Engineering Chemistry Research*, 50(11):6704–6712, 2011.

[92] H. Sahin, X. Wang, and F. Gordaninejad. A new model for yield stress of magneto-rheological greases/gels under combined effects of magnetic field and temperature. In *Proceedings of SPIE*, volume 7288, pages 72881E–72881E–9, 2009.

[93] C. Chang, M. Asce, and L. Zhou. Neural network emulation of inverse dynamics for a magnetorheological damper. *Journal of Structural Engineering*, 128:231–239, 2002.

[94] D. H. Wang and W. H. Liao. Modeling and control of magnetorheological fluid dampers using neural networks. *Smart Materials and Structures*, 14:111–126, 2005.

[95] Z. Xu and Y. Q. Guo. Neuro-fuzzy control strategy for earthquake-excited nonlinear magnetorheological structures. *Soil Dynamics and Earthquake Engineering*, 28:717–727, 2008.

[96] R. Mitchell, Y. Kim, and T. El-Korchi. System identification of smart structures using a wavelet neuro-fuzzy model. *Smart Materials and Structures*, 12, 2012.

[97] K. Gurney. *1997*. CRC Press, An introduction to neural network.

[98] D. C. Lagoudas. *Shape memory alloys: modeling and engineering applications*. Springer, 2008.

[99] I. Spinella, E. Dragoni, and F. Stortiero. Modeling, prototyping, and testing of helical shape memory compression springs with hollow cross section. *Journal of Mechanical Design*, 132:061008, 2010.

[100] S. M. N. An, J. Ryu, M. Cho, and K. J. Cho. Engineering design framework for a shape memory alloy coil spring actuator using a static two-state model. *Smart Materials and Structures*, 21:055009, 2012.

[101] D. A. Shook, P. N. Roschke, and O. E. Ozbulut. Superelastic semi-active damping of a base-isolated structure. *Structural Control and Health Monitoring*, 15:746–768, 2008.

[102] C. Song, J. Kailin, and P. Xianghe. Cylindrical magnetorheological fluid variable transmission controlled by shape-memory alloy. *Science and Technology of Nuclear Installations*, 2012.

[103] J. Ma, H. Shu, and J. Huang. MR continuously variable transmission driven by SMA for centrifugal fan in nuclear power plant. *Science and Technology of Nuclear Installations*, 2012.

[104] J. Huang, X. Chen, and L. Zhong. Analysis and testing of MR shear transmission driven by SMA spring. *Advances in Materials Science and Engineering*, 307207, 2013.

[105] T. S. Aravindhan and K. Gupta. Multiple smart material applications using SMA and MR fluid damper for rotor vibration control. In *ASME Turbo Expo 2010: Power for Land, Sea, and Air*, Glasgow, UK, 2010.

[106] L. C. Brinson. One-dimensional constitutive behavior of shape memory alloys: thermomechanical derivation with non-constant material function and redefined martensite internal variable. *Journal of Intelligent Material Systems and Structures*, 4:229–242, 1993.

[107] J. H. Chung, J. S. Heo, and J. J. Lee. Implementation strategy for the dual transformation region in the brinson SMA constitutive model. *Smart Materials and Structures*, 16:N1–N5, 2007.

[108] M. Elahinia and M. Ahmadian. An enhanced SMA phenomenological model: I. the shortcomings of the existing models. *Smart Materials and Structures*, 14:1297, 2005.

[109] M. Elahinia and M. Ahmadian. An enhanced SMA phenomenological model: II. the experimental study. *Smart Materials and Structures*, 14:1309, 2005.

[110] J. H. Chung, J. S. Heo, and J. J. Lee. Modeling and numerical simulation of the pseudoelastic behavior of shape memory alloy circular rods under tension–torsion combined loading. *Smart Materials and Structures*, 15:1651, 2006.

[111] Y. Toi, J. B. Lee, and M. Taya. Finite element analysis of superelastic, large deformation behavior of shape memory alloy helical springs. *Computers & structures*, 82:1685–1693, 2004.

[112] C. Grossmann, J. Frenzel, V. Sampath, T. Depka, A. Oppenkowski, C. Somsen, K. Neuking, W. Theisen, and G. Eggeler. Processing and property assessment of niti and niticu shape memory actuator springs. *Materialwissenschaft und Werkstofftechnik*, 39:499–510, 2008.